
Methods¹

Expedition 319 Scientists²

Chapter contents

| | |
|---------------------------------------|----|
| Introduction | 1 |
| X-ray computed tomography | 4 |
| Logging | 5 |
| Lithology | 9 |
| Structural geology | 13 |
| Biostratigraphy | 15 |
| Geochemistry | 16 |
| Physical properties | 20 |
| Downhole measurements | 25 |
| Cuttings-Core-Log-Seismic integration | 29 |
| Observatory | 30 |
| Paleomagnetism | 32 |
| References | 33 |
| Figures | 36 |
| Tables | 69 |

Introduction

This chapter documents the methods used for shipboard measurements and analyses during Integrated Ocean Drilling Program (IODP) Expedition 319. Riser drilling was conducted in IODP Hole C0009A, and cuttings, mud gas, and cores were recovered and analyzed. In addition, a suite of downhole measurements was performed, including measurement while drilling (MWD) and wireline logging (including vertical seismic profile [VSP] and Modular Formation Dynamics Tester [MDT] experiments). In IODP Hole C0010A, logging while drilling (LWD) and observatory activities were carried out, including a sensor dummy run and a temporary bridge plug sensor installation. In IODP Hole C0011A, LWD drilling was carried out as a contingency operation.

Reference depths

Depths of each measurement or sample are reported relative to both the drilling vessel rig floor (rotary table) and the seafloor (see Table T1 in the “Expedition 319 summary” chapter). These depths are determined by drill pipe and wireline length and are correlated to each other by use of distinct reference points. Drilling engineers refer to pipe length when reporting depth and report it as drilling depth below rig floor (DRF) in meters. Core depths are based on drilling depth below rig floor and converted to core depth below seafloor (CSF). IODP conventions are applied for cores with greater than or less than 100% recovery (IODP Depth Scales, www.iodp.org/program-policies/). Cuttings (“mud”) depths are reported as mud depth below rig floor (MRF), based on drillers depth (DRF) and the calculated lag depth of the cuttings (see below for further details).

In referring to wireline logging results, depths are initially reported as wireline depth below rig floor (WRF). Wireline logging depths are corrected relative to drillers depth (DRF) using a known reference datum (e.g., seafloor [“mudline”] or base of casing [“casing shoe”] and relative to each logging data set down the borehole [including tool speed corrections where appropriate]). These corrected depths are then reported as wireline log matched depth below seafloor (WMSF) (see “Logging” for further details). LWD and MWD use the same depth scale (LWD depth below rig floor [LRF]); depths are described by adding the lengths of all drill string components deployed beneath the rig floor and accounting for the constant offset for each sensor based on its position within

¹Expedition 319 Scientists, 2010. Methods. In Saffer, D., McNeill, L., Byrne, T., Araki, E., Toczko, S., Eguchi, N., Takahashi, K., and the Expedition 319 Scientists, *Proc. IODP, 319*: Tokyo (Integrated Ocean Drilling Program Management International, Inc.).
doi:10.2204/iodp.proc.319.102.2010
²Expedition 319 Scientists’ addresses.



the tool assembly (IODP Depth Scales, www.iodp.org/program-policies/). In summary, the depths reported in depths below rig floor (DRF, MRF, WRF, and LRF) are converted to depths below seafloor (drilling depth below seafloor [DSF] or CSF, mud depth below seafloor [MSF], WMSF, and LWD depth below seafloor [LSF], respectively) by subtracting water depth and the height of the rig floor from the sea surface, with corrections relative to drillers depth where appropriate. These depths below seafloor (DSF, CSF, MSF, WMSF, and LSF) are therefore all equivalent. Seismic depths are reported in either time (s) or depth (m). For time sections, a two-way traveltime (s) scale is used, below sea level. For depth sections, seismic depth below seafloor (SSF) or seismic depth below sea level (SSL) are used. Where figures incorporate multiple data sets, including seismic data, meters below sea level (mbsl) or meters below seafloor (mbsf) are ordinarily used.

Cuttings depths

During riser drilling, drilling mud circulates within the riser pipe between the drillship and the bottom of the hole. As the drill bit cuts through the formation, the fragments (cuttings) are suspended in the drilling mud and carried with the formation pore water and gas back to the rig. A cuttings sample is assumed to be an averaged mixture of rock fragments and sediments from an ~5 m drilling interval. The time between when the formation is cut by the drill bit and when these cuttings arrive at the ship is known as the “lag time,” which is a function of drilling mud pumping rate and annular mud volume, and is used to calculate the “lag depth.” At a constant pump rate, lag time and lag depth increase as the hole is deepened and the volume of circulating mud increases. All of the depths recorded for cuttings at Site C0009 have been corrected for this lag. Twice during Site C0009 drilling, a calcium carbide lag test was conducted to check the calculated lag time. The carbide generates acetylene on contact with water; the acetylene acts as a tracer, and its lag time can be measured precisely by mud gas analysis.

Depth precision estimates of cuttings

Cuttings were retrieved from 5 m depth intervals, and lag depth was calculated and calibrated as discussed above. By comparison with wireline logging data measured relative to the drilling vessel rig floor at distinct marker horizons, we can assess the precision of cuttings depths relative to other data sets. At Site C0009, several parameters in log and cuttings data sets change sharply at ~1300 m MSF. For example, we find changes in values of magnetic susceptibility and MnO from cuttings are within 10 m of

abrupt changes in *P*-wave velocity and spontaneous potential (SP) in the log data at this depth. This estimate of cuttings depth precision (~10 m) generally fits data set comparisons at other depths.

Sampling and classification of material transported by drilling mud

Three sets of cuttings were collected during drilling of Site C0009 (see Table T1 in the “Site C0009” chapter):

1. 703.9–1509.7 m MSF during riser drilling (drilling Phase 2);
2. 1509.7–1593.9 m MSF during the coring operation (drilling Phase 3); and
3. 1509.7–1604 m MSF during opening of the borehole after coring (drilling Phase 4).

Cuttings were taken at every 5 m depth interval (DRF) from the shale shakers. Drilling mud and mud gases were also sampled during drilling (see “[Geochemistry](#)”). Mud gas, fluids, and cuttings samples were classified by drill site and hole using a sequential material number followed by an abbreviation describing the type of material. The material type identifiers are

SMW = solid taken from drilling mud (cuttings),
 LMW = liquid taken from drilling mud, and
 GMW = gas taken from drilling mud.

For example, “319-C0009A-123-SMW” represents the 123rd cuttings sample recovered from Hole C0009A during Expedition 319.

Influence of drilling mud composition on cuttings

Cuttings are mixed with drilling mud and various contaminants. The “[Site C0009](#)” chapter discusses the possible effects of contamination on different types of measurements. Three different batches of cuttings (drilling Phases 2, 3, and 4) were collected during drilling at Site C0009 (see “[Cuttings handling](#)” for details). Cuttings were not retrieved during the 17 inch hole opening (drilling Phase 8), principally because of an expected increase in contamination from cavings. Cuttings from Phase 4 were contaminated by CaCO₃, which was added as a lost circulation material to reduce mud loss. These cuttings were deemed strongly affected physically and chemically and could only be used for lithologic and structural description. Changes in mud weight may also impact physical and chemical measurements made on cuttings. Mud weight was 1.08 specific gravity (SG) during Phase 2 and was increased to 1.09 SG and then 1.1 SG during Phase 3. Mud weight was 1.1 SG during Phase 4. The impact of the differ-

ence in mud weight between Phases 2 and 3 is discussed in various sections of the “[Site C0009](#)” chapter. The length of time between creating the cuttings material and retrieving them from the shale shakers (i.e., time spent within the drilling mud) may also affect the degree of alteration—cuttings collected during Phase 3 (coring) were suspended in the drilling mud significantly longer than cuttings from Phases 2 and 4.

Cuttings handling

Every 5 m, we recovered 400 cm³ of cuttings material for long-term archiving and postexpedition sample requests (including postmortem requests) and ~2000 cm³ for shipboard analyses and personal sampling (Fig. [F1](#)). Two different types of cuttings were recognized: “soft” and “semihard.”

For both soft and semihard cuttings, unwashed cuttings samples were taken for the following measurements:

- 70 cm³ was removed for photography and then micropaleontology.
- 30 cm³ was removed for lithologic and grain-composition description.
- 300 cm³ (10 cm of filled IODP core liner) was removed for natural gamma ray (NGR) measurement and then returned to the sample bottle for future analysis.

Cuttings from 703.9 to 1037.7 m MSF were classified as soft and were not washed because no usable chips could be retrieved without disaggregation. In this case, only photography, lithologic description, paleontological analysis, and NGR measurement could be conducted, as described above (Fig. [F1](#)).

Cuttings between 1037.7 and 1604 m MSF were classified as semihard. In this case, 650 cm³ of the cuttings sample was washed and separated into different size fractions (Fig. [F1](#)). These samples were processed as follows:

- Cuttings and mud were gently washed with seawater using a sieve (opening 250 μm) at the core-cutting area.
- Samples were sieved into different size fractions (>4 mm, 1–4 mm, or 0.25–1 mm) with seawater. During sieving, a hand magnet was used to remove iron contaminants originating from drilling tools and casing. Samples for moisture and density (MAD) analysis were removed (see below) and prepared separately (see “[Physical properties](#)”). All size fractions of Samples 319-C0009A-135-SMW through 173-SMW were lightly washed with freshwater and deionized water and then soaked for 11–37 h in deionized water. All size

fractions of Samples 319-C0009A-75-SMW through 134-SMW and 176-SMW through 220-SMW were lightly washed with deionized water but not soaked.

- MAD analyses were carried out on 35 cm³ of washed and sieved samples, using samples from both the 1–4 mm fraction and some from the >4 mm fraction for comparison.
- The 1–4 mm fraction used for nondestructive MAD measurements was reused for magnetic susceptibility.
- All sample fractions were then freeze-dried. Small samples (~10 cm³ each) were extracted from the 1–4 mm fraction and ground into powder for the following analyses: X-ray diffraction (XRD) and X-ray fluorescence (XRF), inorganic carbon content using a carbonate analyzer, and total carbon (TC) and total nitrogen (TN) content using a carbon-hydrogen-nitrogen-sulfur/oxygen (CHNS/O) elemental analyzer.

Core handling

The cores and plastic liners were cut into ≤1.5 m long sections in the core-cutting area. A small (5 cm³) sample was taken for micropaleontology from the core catcher section and a 40 cm long section, usually from a middle section of the core, was taken for pore water chemistry (interstitial water) (Fig. [F2](#)). This short section was immediately removed from the core-cutting area and scanned with the X-ray computed tomography (CT) scanner to examine the core’s internal structure and to avoid destroying unique tectonic or sedimentary features. A 5 cm thick (primary) whole-round cluster was also selected and sampled next to, or close to, the whole-round interstitial water sampling interval (Araki et al., 2009). Both the interstitial water and cluster whole-round samples were taken from a homogeneous unfractured interval (preferred material for both sample types) based on X-ray CT scan images. In some cores, a homogeneous unfractured section (15 cm) was also removed for anelastic strain recovery measurement.

In the laboratory, X-ray CT images were taken of all remaining core sections. The cluster sample was divided into subsamples for discrete *P*-wave velocity measurement, MAD, anisotropy of magnetic susceptibility (AMS), paleomagnetism, inorganic carbon contents, TC and TN content, bulk XRD, and XRF analyses. A part of the cluster sample was used for time-sensitive personal samples for postexpedition studies.

After the core sections equilibrated to ambient room temperature (~3 h), they were run through the

whole-round multisensor core logger (MSCL-W). After finishing these measurements, personal whole-round samples as well as community geotechnical archives from each core were removed before splitting the cores into working and archive halves (Araki et al., 2009). Additional whole-round cluster samples were taken adjacent to all whole-round samples for shipboard measurements. Digital images of archive-half sections were taken with the photo image logger (MSCL-I) before visual core description (VCD). Discrete samples were taken for *P*-wave velocity, MAD, paleomagnetism, and AMS measurement in each working-half section, excluding the primary whole-round cluster section (previously sampled for analysis). Thermal conductivity measurements were performed on a sample from each core using the half-space method. Additional samples were taken for inorganic carbon, TC and TN, XRD, and XRF analyses from every other section, again excluding the section from which the primary whole-round cluster was taken (samples already taken). Finally, core sections were wrapped in heat shrink plastic and transferred to cold storage. After the expedition, cores were transported for archiving at the Kochi Core Center in Kochi, Japan.

Personal sampling

IODP expeditions usually have a single science party. However, the Expedition 319 Science Party was divided into two groups (Araki et al., 2009). The following sampling procedure was used so that the second group would have equal sampling opportunities. During the first part of the expedition, scientists flagged their preferred personal sample locations, but these samples were not removed from the cores with the exception of (1) whole-round samples (see above), (2) time-sensitive samples, and (3) raw cuttings samples. During the second part of the expedition, scientists flagged their samples and all personal samples were then taken from the cores after resolving conflicts.

Authorship of site chapters

The separate sections of the site chapters and methods chapter were written by the following shipboard scientists (authors are listed in alphabetical order; no seniority is implied):

Principal results: Shipboard Science Party
 X-ray computed tomography: Hayman
 Logging: Moe
 Lithology: Buchs, Buret, Efimenko, Flemings, Kawabata, Schleicher
 Structural geology: Hayman, Huftile, Lin, Moore
 Biostratigraphy: Jiang, Kameo
 Geochemistry: Horiguchi, Wiersberg

Physical properties: Boutt, Conin, Cukur, Doan, Flemings, Ito, Kano, Kitada, Kopf, Lin
 Downhole measurements: Boutt, Doan, Flemings, Hino, Ito, Kano, Lin, von Huene
 Cuttings-Core-Log-Seismic integration: Conin, Cukur, Flemings, Kano, Kopf
 Observatory: Kano, Kitada, Kopf
 Paleomagnetism: Oda, Zhao

Acronyms

For reference, a list of commonly used acronyms in Nankai Trough Seismogenic Zone Experiment (NanTroSEIZE) science is included in the “[Appendix: NanTroSEIZE acronyms](#)” chapter.

X-ray computed tomography

X-ray CT imaging provided information about structures and sedimentological features in the core and helped to assess sample locations and quality for whole-round samples. Our methods followed those in the “cookbook” prepared by Center for Deep Earth Exploration (CDEX)/Japan Agency for Marine-Earth Science and Technology (JAMSTEC) (X-ray CT Scanner, version 3.00, 31 July 2007) and used during previous expeditions (e.g., IODP Expedition 315). The cookbook is based on GE Healthcare (2006), Mees et al. (2003), and Nakano et al. (2000).

The X-ray CT instrument on the D/V *Chikyu* is a GE Yokogawa Medical Systems LightSpeed Ultra 16 capable of generating sixteen 0.625 mm thick slice images every 0.5 s, the time for one revolution of the X-ray source around the sample (Table T1). Data generated for each core consist of core-axis-normal planes of X-ray attenuation values with dimensions of 512 × 512 pixels. Data were stored as Digital Imaging and Communication in Medicine (DICOM) formatted files.

Background

The theory behind X-ray CT has been well established through medical research and is very briefly outlined here. X-ray intensity varies as a function of X-ray path length and the linear attenuation coefficient (LAC) of the target material as

$$I = I_0 \times e^{-\eta L}, \quad (1)$$

where

I = transmitted X-ray intensity,
*I*₀ = initial X-ray intensity,
 η = LAC of the target material, and
L = X-ray path length through the material.

LAC is a function of the chemical composition and density of the target material. The basic measure of attenuation, or radiodensity, is the CT number given in Hounsfield units (HU) and is defined as

$$\text{CT number} = [(\eta_t - \eta_w)/\eta_w] \times 1000, \quad (2)$$

where

η_t = LAC for the target material, and

η_w = LAC for water.

The distribution of attenuation values mapped to an individual slice comprises the raw data that are used for subsequent image processing. Successive two-dimensional (2-D) slices yield a representation of attenuation values in three-dimensional (3-D) pixels referred to as voxels.

Analytical standards used during Expedition 319 were air (CT number = -1000), water (CT number = 0), and aluminum (2477 < CT number < 2487) in an acrylic core mock-up. All three standards were run once daily after air calibration. For each standard analysis, the CT number was determined for a 24.85 mm² area at fixed coordinates near the center of the cylinder.

X-ray CT scan data usage

X-ray CT scans were used during Expedition 319 to

- Provide an assessment of core and core liner integrity,
- Determine locations for whole-round samples, and
- Identify important structural and sedimentological features to be avoided by whole-round sampling.

X-ray CT scanning was done immediately after core cutting for time-sensitive (e.g., anelastic strain and interstitial water) whole-round samples to finalize selection of the samples. All whole-round core sections were screened to avoid destructive testing on core samples that might contain critical structural features. This also ensured minimal drilling disturbance of whole-round samples and an assessment of heterogeneity (essential for postexpedition physical and mechanical property studies).

Logging

Logging data provide measurements of in situ properties in the borehole. Logging data with various depths of investigation into the formation depending on the tool are therefore complementary to centimeter-scale core studies and >10 m seismic images (Expedition 314 Scientists, 2009). We used

the following logging methods during Expedition 319:

- Wireline logging: the logging tool is lowered into the open well bore on a multiple-conductor contra-helically armored wireline, and measurements are usually taken from the bottom of the hole upward. For depth correlation purposes, tension on the cable is maintained as constant as possible. Most wireline measurements are recorded continuously while the tool string is moving except for certain fluid sampling and pressure-measuring tools and a seismic array.
- LWD: measurements are taken with self-contained tools near the bottom-hole assembly (BHA). Data are recorded in memory while drilling the hole. MWD data are transmitted in real time to the surface by mud pulses, together with a few measurements made from the LWD tools.

During Expedition 319, wireline logging, LWD, and MWD were conducted in both riser and riserless holes. Measurements taken by LWD included azimuthal resistivity images and laterolog resistivity-at-the-bit (RAB). MWD measurements included rate of penetration (ROP), downhole torque, inclination/orientation of the hole, weight on bit (WOB), gamma ray emissions, and annular pressure while drilling (APWD) (collected only during 26 inch riserless hole drilling). Measurements from wireline logging included density/porosity, photoelectric factor (PEF), resistivity images from the Formation Micro-Imager (FMI), laterolog resistivity and SP, natural gamma and spectral gamma, sonic velocity (*P*- and *S*-waves), various types of calipers, mud resistivity, and temperature. In addition, the MDT was used to measure pore pressure, permeability, and stress. A walkaway VSP and zero-offset VSP were conducted using the Versatile Seismic Imager (VSI).

Logging while drilling and measurement while drilling

During Expedition 319, MWD tools were used in three holes: C0009A, C0010A, and C0011A. Figure F3 shows the configuration of the LWD/MWD BHA, and the set of measurements recorded from the tools are listed in Table T2.

MWD tools measure downhole drilling parameters, gamma radiation, and annular pressure and assure communication between tools. During drilling operations, these measurements are combined with surface rig floor parameters for drilling monitoring (e.g., WOB, torque, etc.) and quality control. The APWD sensor is included with the MWD sensors for safety monitoring and provides measurements of downhole pressure in the annulus, which are also con-

verted to equivalent circulating density (ECD; density of the circulating drilling fluid when pumping). Downhole pressure and ECD are crucial parameters used to detect any inflow from the formation or obstruction (increase in APWD and ECD) or loss of circulation caused by permeable formations or faults or overbalancing of drilling mud (decrease in APWD).

The key difference between LWD and MWD tools is that LWD data are recorded into downhole memory and retrieved when the tools reach the surface, whereas MWD data and a selection of LWD data at lower resolution are transmitted through the drilling fluid by means of a modulated pressure wave (mud pulsing or fluid pulse telemetry) at a rate of 6 bits per second (bps) and monitored in real time at the surface. The term LWD is often used more generically to cover both LWD and MWD measurements, as the MWD tool is required during any LWD operation to provide communication between the LWD tools and the surface.

The LWD tools are battery powered and use erasable programmable read-only memory chips to store the logging data until they are downloaded. LWD tools take measurements at evenly spaced time intervals using a downhole clock installed in each tool. The depth tracking system on the surface monitors time and drilling depth. After drilling, LWD tools are retrieved and the data downloaded from each tool to a computer. Synchronization of the surface and downhole clocks allows merging of time-depth data (from the surface system) and downhole time-measurement data (from the tools) into depth-measurement data files, which then undergo further processing and analyses by the onboard logging scientists.

LWD/MWD systems

Depth tracking systems

The Schlumberger integrated drilling evaluation and logging (IDEAL) surface system for MWD tools records the time and depth of the drill string below the rig floor. MWD operations require accurate and precise depth tracking and the ability to independently measure and evaluate the position of the traveling block and top drive system in the derrick and the motion of the ship from waves/swells and tide action. The length of the drill string (combined length of the BHA and the drill pipe) and the position of the top drive in the derrick are used to determine the depth of the drill bit and ROP. The system configuration is illustrated in Figure F4A. A hook-load sensor measures the weight of the load on the drill string and can be used to detect whether the drill string is in-slips or out-of-slips. When the drill string is in-slips (i.e., the top of the drill string is hung on the rig floor by the “slip” tool and is de-

tached from the top drive), motion from the blocks or motion compensator will have no effect on the depth of the bit and the drawworks encoder information will not augment the recorded bit depth. The heave of the ship will still continue to affect the bit depth whether the drill string is in-slips or out-of-slips.

The rig instrumentation system measures and records heave and motion of the active compensator's cylinder. The *Chikyu* uses a crown-mounted motion compensator (CMC) (Fig. F4A), which is installed on the top of the derrick to reduce the influence of heave on the drill string and to increase the accuracy of the bit weight measurement. The CMC is united with the crown block, which is a stationary pulley, and absorbs tension by moving the crown block up and down according to the ship's up and down motion. The crown block movement is absorbed by the change in the position of the horizontally overhung pulley even though the length of cable changes between the drawworks and the deadline anchor.

Onboard data flow and quality check

For each LWD/MWD operation, two types of data are collected: (1) real-time data that include all MWD data and selected LWD data and (2) LWD data that have been recorded downhole and stored in the tool's memory (Fig. F5). Data are originally recorded downhole at a preset sampling interval, and no depth information is recorded in the tool. The depth-referenced version is obtained after merging the time (downhole) with the time-depth relationship recorded on the surface by the IDEAL system. For LWD and MWD geoVISION tools, both time (log ASCII standard [LAS] format) and depth (digital logging interchange standard [DLIS] format) versions of the data are generated.

MWD and annulus pressure tools

The 8.25 inch (21 cm) diameter MWD PowerPulse and TeleScope tools serve a similar function; the TeleScope is a newer generation tool. They transmit data by generating a continuous mud wave within the drilling fluid and by changing the phase of this signal (frequency modulation) to convert relevant bit words representing information from various sensors (Fig. F6A), which is compressed and coded digitally in pressure pulses. Drilling fluid pulses are recorded on two pressure transducers mounted on the standpipe manifold (SPT1) and the gooseneck of the standpipe (SPT2) where they are automatically decoded and uncompressed using the horizon signal processing module (HSPM) and the IDEAL system by the field engineer (Fig. F6C). In the MWD fluid

pulsing system, pulse rates range from 1 to 12 bps, depending primarily on water depth and fluid density. During Expedition 319, pulse rates of 3 bps were achieved for MWD-APWD operations and 6 bps for LWD.

MWD measurements are made using paired strain gauges, accelerometers, and lateral shock sensors near the base of the MWD collar. A list of the main MWD parameters is given in Table T2. During LWD operations, the mud pulse system also transmitted a limited set of data from the geoVISION LWD tool to the surface in real time.

LWD geoVISION tool

The geoVISION resistivity tool is based on RAB technology (Table T3) (Anadrill-Schlumberger, 1993). It provides resistivity measurements and electrical images of the borehole wall, calibrated in a homogeneous medium. In addition, the geoVISION tool provides a total gamma ray measurement (Fig. F6B).

The geoVISION tool is connected directly above the drill bit and uses the lower portion of the tool and the bit as a measuring electrode. This allows the tool to provide a bit resistivity measurement with a vertical resolution just a few centimeters longer than the length of the bit (28 cm; Fig. F3C). A 1½ inch (4 cm) electrode is located 102 cm from the bottom of the tool and provides a focused lateral resistivity measurement (ring resistivity) with a vertical resolution of 2–3 inches (5–7.5 cm). The characteristics of ring resistivity are independent of where the geoVISION tool is placed in the BHA, and its depth of investigation is ~7 inches (17.8 cm; diameter of investigation ≈ 22 inches). In addition, button electrodes provide shallow-, medium-, and deep-focused resistivity measurements as well as azimuthally oriented images, which can reveal information about formation structure and lithologic contacts. The button electrodes are ~1 inch (2.5 cm) in diameter and located on a clamp-on sleeve. The buttons are longitudinally spaced along the geoVISION tool to render staggered depths of investigation of ~1, 3, and 5 inches (2.5, 7.6, and 12.7 cm). Multiple depths of investigation allow quantification of invasion caused by drilling fluid and fracture identification (drilling induced and natural). Vertical resolution and depth of investigation for each resistivity measurement are summarized in Table T3. Drilling fluid resistivity and temperature are also measured (Schlumberger, 1989) for environmental correction of the resistivity measurements. The gamma ray sensor has a range of operability of 0–250 gAPI and an accuracy of ±7%, corresponding to a statistical resolution of ±3 gAPI at 100 API and ROP of 30 m/h. Its depth of investigation is between 5 and 15 inches.

The tool's orientation system uses Earth's magnetic field as a reference as the drill string rotates, thus allowing both azimuthal resistivity and gamma ray measurements. The azimuthal resistivity measurements are acquired with a ~6° resolution around the borehole, whereas gamma ray measurements are acquired at 90° resolution as the geoVISION tool rotates.

Wireline logging

During wireline logging at the riser site (Hole C0009A), a passive heave compensator system was used by switching hydraulic lines to the auxiliary tank and compensating the extra line, which is connected between the riser and rig (Fig. F4B). A compensating line (a fixed-length steel wire) is connected between the risers and the rig using special heavy-duty compensating sheave. Then the existing ship compensating system is disconnected by switching the hydraulic line from the rig heave compensating system to the auxiliary tank.

Wireline logging tools

The wireline logging tool strings and runs are shown in Figures F12 and F8 in the "Site C0009" chapter, components of the tools are shown in Figure F7, and the set of measurements recorded from the tools are listed in Table T4.

Total and spectral gamma ray tools

The gamma ray tool passively measures the natural gamma radiation emitted by the formation. The main natural radioactive sources are ⁴⁰K and isotopes of Th and U. All gamma ray tools give the total gamma ray emission in units of gAPI. Gamma radiation is mainly dependent on lithology, and gamma ray logs offer good repeatability. Gamma ray tools used in this expedition had a depth of investigation ranging from 24 to 61 cm (Table T5).

Hostile Environment Natural Gamma Ray Sonde

⁴⁰K and isotopes of the decay chain of radioactive isotopes of Th and U emit photons at different energies. The Hostile Environment Natural Gamma Ray Sonde (HNGS) tool uses spectroscopic analysis to determine the concentration of radioactive ⁴⁰K (in weight percent), Th (in ppm), and U (in ppm). The HNGS tool also measures U-free gamma ray emission (in gAPI, also called computed gamma ray emission). The HNGS uses two bismuth germanate scintillators for gamma ray detection. The tool response is affected by the tool standoff (distance between the sensor and the borehole wall) and the weight and concentration of bentonite or KCl within the drilling mud (KCl may be added to the drilling mud to pre-

vent hydrous clays from swelling and obstructing the well). The spectral analysis filters out gamma ray energy below 500 keV to reduce sensitivity to bentonite and KCl in the drilling mud and to improve measurement accuracy. Environmental corrections are usually made during the data processing. This tool has a 24 cm depth of investigation and can also be used inside casing.

Platform Express

The Platform Express (PEX) tool string combines a Highly Integrated Gamma Ray Neutron Sonde (HGNS), a Three-Detector Lithology Density (TLD) tool and a Micro-Cylindrically Focused Log (MCFL) tool (Fig. F7) and is usually coupled with an azimuthal resistivity measurement or an induction image tool. TLD and MCFL are integrated in the single pad of the High-Resolution Mechanical Sonde (HRMS). In the Hole C0009A configuration, the supplementary electrical tool is the High-Resolution Laterolog Array (HRLA). The tool is provided with an accelerometer that enables real-time depth correction and accurate depth matching of the various sensors.

Highly Integrated Gamma Ray Neutron Sonde

Neutrons interact differently with matter depending on their energy. Fast neutrons ($E > 10$ keV) are scattered elastically, primarily by H atoms. They can also induce inelastic scattering, in which case the excited atoms release gamma rays. If the neutron energy becomes small enough (thermal neutron, $E < 0.1$ eV), they can be absorbed by the medium by thermal capture. The most efficient absorbers are Cl, B, and H. Thermal capture also releases gamma rays. The HGNS contains an Am-Be radioactive source that bombards the formation with fast neutrons (>10 keV). These neutrons are slowed by scattering and then captured. Epithermal neutron detectors quantify elastic scattering, and thus the H index and a porosity estimate are generated. Gamma ray detectors and thermal neutron detectors document the thermal capture.

The measurement by the HGNS sensor is dependent on hydrogen content, and hence water content. We note that clay-rich rocks contain intra-crystalline water. The measured value is also affected by water-based mud; therefore the tool is pressed against the borehole wall to reduce this effect.

Three-Detector Lithology Density tool

The TLD tool assesses the density of the formation by measuring the attenuation of a gamma ray flux.

The gamma radiation will interact with matter according to the energy of the gamma ray photon. Gamma rays are emitted by the ^{137}Cs source at 622 keV. At that energy, photons will first interact with matter by Compton scattering. Their energy then decreases progressively, and gamma radiation is absorbed by matter by the photoelectric effect. The number of scattered gamma rays that reach the detectors is directly related to the number of electrons in the formation, which is related to bulk density. Porosity may also be derived from this bulk density if the grain density is known or assumed.

The TLD tool also measures the PEF caused by absorption of low-energy gamma rays. The PEF depends on the atomic number of the elements in the formation and is essentially independent of porosity; therefore it is an indicator of the chemical composition of the formation. PEF values can be used in combination with HNGS curves to identify different types of clay minerals. For the HNGS, gamma rays are partly adsorbed by the drilling mud. Therefore the gamma ray detectors are mounted on a shielded skid, which is pressed against the borehole wall by a hydraulically activated centralizing arm to produce good coupling. Both density correction and caliper measurement of the hole are used to check the contact quality. The TLD tool has a ^{137}Cs source and three detectors: a backscattering detector, a short spacing detector, and a long spacing detector (Fig. F7).

Micro-Cylindrically Focused Log tool

The MCFL tool includes a cylinder electrode on the same pad as the TLD tool. The source electrodes emit a highly focused beam (2.5 cm) that rapidly diverges and penetrates the formation as deep as 10 cm. The tool gives information on the mud cake resistivity, which is useful for the lithodensity correction of the TLD tool (Fig. F7E).

High-Resolution Laterolog Array

The HRLA combines four electrodes to provide five independent, actively focused, depth- and resolution-matched measurements to resolve true formation resistivity (R_t) in thinly bedded and deeply invaded formations in addition to a shallowest mode (Mode 0) for mud resistivity. Modes 1 to 5 have increasing depths of investigation. The supplementary mode helps improve the mud invasion profile and correct the raw resistivity data to retrieve the true formation resistivity. It is less affected by shoulder beds than traditional laterolog measurements because of the active focusing and multifrequency

operation, together with the symmetric tool design. In addition, the tool employs software focusing to improve the accuracy of true resistivity estimates through advanced 2-D inversion processing.

Environmental Measurement Sonde

The Environmental Measurement Sonde (EMS) combines a six-arm caliper, mud resistivity measurements, and mud temperature measurement. The caliper measurement of borehole diameter helps to identify washouts (large increase in hole radius) and is used for quality control and correction of other logs. Calipers also enable identification of drilling-induced breakouts as stress orientation indicators. The temperature data record the combination of the temperature profile and the drilling-induced temperature perturbation. If the EMS is run multiple times within the hole with the hole kept undisturbed, changes in the temperature profile may be used to quantify the drilling-induced temperature disturbance.

Formation Microlmager

The FMI provides high-resolution resistivity images of the borehole wall. The FMI generates an electrical image of the borehole from 192 microresistivity measurements. The electrodes are located on four pads and four attached flaps that are applied to the borehole wall by caliper arms (Fig. F7B). An applied voltage causes a current to flow from each focused electrode button on the lower pad through the formation to the electrode on the outer cartridge housing. The depth of investigation is ~2.5 cm, and the electrode buttons produce images with a vertical resolution of 5 mm. The quality of the image enables assessment of rock composition and texture, structure, and fluid content.

The borehole wall coverage by the resistivity image ranges from 80% for an 8.5 inch hole to <50% for a 12.25 inch hole (Hole C0009A). The General Purpose Inclination Tool (GPIT), which integrates both a three-axis inclinometer and a three-axis magnetometer, accompanies the FMI to orient its image. It can also provide the geometry of the borehole path. The center of Pad 1 is oriented by the P1AZ parameter in the log data file.

Sonic Scanner

The Sonic Scanner is a new generation of acoustic measurement tool and is a successor to the Dipole Sonic Imager (DSI). In addition to axial and azimuthal measurements, the Sonic Scanner makes a radial measurement to probe the formation for near well bore and far-field slowness. The depth sensitiv-

ity is equal to two to three times the borehole diameter. Other attributes of the Sonic Scanner include (1) a wide-frequency spectrum ranging from 300 Hz to 9 KHz, (2) a longer azimuthal array (five more receiver stations and 2 ft longer than DSI), (3) a borehole-compensated monopole with long (11–17 ft) and short (1–7 ft) spacing, and (4) cross-dipole acquisition. The Sonic Scanner provides accurate radial and axial measurements of stress-dependent properties near the borehole. These data are converted into (1) *P*- and *S*-wave velocities, (2) anisotropy of propagation, (3) Stoneley wave velocity, and (4) cement bond quality.

The configuration of the Sonic Scanner receivers produces a long azimuthal array (i.e., 8 azimuthal receivers at each of the 13 stations; Fig. F7C). With the two near-monopole transmitters straddling this array and a third transmitter beyond, the short-to-long-monopole transmitter-to-receiver spacing combination provides a radial monopole profile.

Versatile Seismic Imager

The VSI is an array of seismometers clamped to the casing to receive seismic waves from air guns (see “[Downhole measurements](#)”).

Data flow and processing

Data for each wireline logging run were recorded and stored digitally and monitored in real time using the Schlumberger MAXIS 500 system (Fig. F5). Onboard logging processing included (1) depth-shifting all logs relative to a common datum, (2) corrections specific to individual tools, and (3) quality control.

FMI image data were processed onboard the *Chikyu* using Schlumberger’s GeoFrame (version 4.3) software package and imported into Geomechanics International (GMI) Imager software for further analysis. The processing steps included conversion of data format, inclinometry quality check, speed correction equalization, resistivity calibration, and normalization. Sonic Scanner data were processed at the Schlumberger Data Consulting Service in Tokyo with their in-house software and the results were used by the Science Party.

Lithology

At Site C0009, cuttings, wireline logging data, gamma ray data from MWD, and a limited amount of core were available to identify lithologic units. At Sites C0010 and C0011, only a limited suite of LWD and MWD data were available, including gamma ray and RAB.

Cuttings and core samples at Site C0009 were described based on

- Macroscopic observations,
- Microscopic observations (including smear slides and thin sections),
- Mineralogical analysis (XRD and XRF), and
- Grain-size separation (Atterberg method).

Macroscopic observations of cuttings and core

Macroscopic observations of cuttings

Cuttings are small fragments of rocks, in general 0.25–4 mm in size, of various lithologies produced during drilling. Cuttings were taken for the first time in IODP operations during Expedition 319. These solid fragments are suspended in drilling mud that contains dissolved clay from the formation, as well as small amounts of claylike drilling additives (e.g., bentonite), which hampers the quantification of the true clay content. Drilling mud also contains disaggregated rock and sediment fragments that were also analyzed. The separation procedure of cuttings from the clay mud and the division into different sizes is explained in [“Introduction.”](#)

Cuttings were taken every 5 m from 703.9 to 1592.7 m MSF, and a second set of cuttings was collected together with core from 1507.7 to 1603.7 m MSF with the same sampling interval (199 samples in total). Based on macroscopic observations of the unwashed bulk material, we estimated the relative amount of coarser grained (e.g., sand/silt) and finer grained (e.g., clay) materials, the induration state of the bulk material, the occurrence of contamination, and the presence of wood fragments, as well as the appearance, softness, relative amount, size, and degree of lithification of hard rock fragments. We defined cuttings from

- 707.7 to 802.7 m (Samples 319-C0009A-SMW-3 through SMW-24) as mud,
- 802.7 to 1037.7 m (Samples 319-C0009A-SMW-27 through SMW-128) as disaggregated mudstone, and
- 1037.7 to 1603.7 m (Samples 319-C0009A-SMW-128 through SMW-215) as mudstone.

All macroscopic observations were recorded on visual cuttings description forms and summarized in C0009_T1.XLS in LITHOLOGY in [“Supplementary material.”](#)

Macroscopic observations of core

We followed conventional Ocean Drilling Program (ODP) and IODP procedures for recording sedimen-

tological information on VCD forms on a section-by-section basis (Mazzullo and Graham, 1988). Core descriptions were transferred to section-scale templates using J-CORES. Texture (defined by the relative proportions of sand, silt, and clay) follows the classification of Shepard (1954). The classification scheme for siliciclastic lithologies follows Mazzullo et al. (1988).

The Graphic Lithology column on each VCD plots all beds that are ≥ 2 cm thick to scale. Interlayers < 2 cm thick are identified as laminae in the Sedimentary Structures column. It is difficult to discriminate between the dominant lithologies of silty claystone and clayey siltstone without quantitative grain size analysis, so we grouped this entire range of textures into the category “silty claystone” on all illustrations. We did not use separate patterns for more heavily indurated examples of the same lithologies (e.g., silty clay versus silty claystone) because the dividing line is arbitrary. Claystone differs from silty claystone and coarser grained sediment by a smoother cut surface. Figure F8 displays graphic patterns for all lithologies encountered during Expedition 319. Also shown are symbols for sedimentary structures, soft-sediment deformation structures, severity of core disturbance, and features observed in X-ray CT images in both soft sediment and indurated sedimentary rock.

Microscopic observation of cuttings

A 30 cm³ aliquot of bulk cuttings was taken for sedimentological description, and smear slides were made in order to identify major lithologic changes. Microscopic investigations of the washed > 45 μm (silt and sand size) fraction using a binocular microscope allowed us to distinguish different minerals in the sediments; their abundance, roundness, and sorting; and the relative abundances of wood/lignite fragments and fossils. These data are summarized in Figures F17 and F18 in the “Site C0009” chapter and in C0009_T2.XLS in LITHOLOGY in [“Supplementary material.”](#) With this technique, the clay fraction could not be evaluated. It is also not possible to discriminate between sand grains that originally formed from uncemented or weakly cemented sand horizons and grains that were originally dispersed in finer grained horizons.

Microscopic observation of core

The microscopic description of core samples follows the same principles as for cuttings. Here, several very small rock chips were carefully taken with a small squeezer from different areas of the archive core for observations under the binocular microscope. The

sample description includes an estimation of mineral occurrence and abundance, as well as grain roundness and sorting.

Smear slides

Smear slides are useful for identifying and reporting basic sediment attributes (texture and composition) in samples of both cuttings and cores, but the results are not quantitative. We estimated the abundance of biogenic, volcanoclastic, and siliciclastic constituents using a visual comparison chart (Rothwell, 1989). Errors can be large, however, especially for fine silt- and clay-size fractions. Thus, it would be misleading to report values as exact percentages. Instead, the visual estimates are grouped into the following categories:

- D = dominant (>50%).
- A = abundant (>10%–50%).
- C = common (>1%–10%).
- F = few (0.1%–1%).
- R = rare (<0.1%).

The relative abundance of major components was also validated by XRD (see “[X-ray diffraction](#)”), and the absolute weight percent of carbonate was verified by coulometric analysis (see “[Geochemistry](#)”). The sample location for each smear slide was entered into the J-CORES database with a sample code of SS using the Samples application.

Thin sections

Thin sections were prepared for microscopic studies of mineralogy, petrology, paleontology, internal structures, and fabrics of rocks and sediments. A thin section was prepared as a 30 μm (= 0.03 mm) thick slice of core or cuttings sample. The standard size of billets for thin section preparation was 2 cm \times 3 cm \times 0.8 cm. Sediments, cuttings, and rocks that were altered, badly weathered, or contained a high clay content were dried first in the freeze dryer and then impregnated under vacuum (Epovac) with epoxy (Epofix) prior to mounting. Core or cuttings samples were attached to a glass slide with Pertopoxy 154. After polishing the samples, thin sections were covered by a cover glass with Canada balsam. Thin sections were observed in transmitted light using an Axioskop 40A polarizing microscope (Carl Zeiss) equipped with a Nikon DS-Fi1 digital camera.

Mineralogical analysis of cuttings and core

X-ray diffraction

The principal goal of XRD analysis of both cuttings and core was to estimate the relative weight percentages of total clay minerals, quartz, feldspar, and

calcite from peak areas. For cuttings, XRD analysis was conducted on 1–4 mm size fractions of washed Samples 319-C0009A-76-SMW through 194-SMW (see “[Introduction](#)” for details of sample preparation). Further grain size separation was performed to analyze the clay mineral composition. Some core samples were selected for XRD analysis from intervals adjacent to whole-round samples. Most were part of sampling clusters taken for physical property and carbonate analyses, which were taken once per core section and in areas of lithologic changes. All samples were freeze-dried, crushed with a ball mill, and mounted as randomly oriented bulk powders.

We completed routine XRD analyses of bulk powders from cuttings and core using a PANalytical CubiX PRO (PW3800) diffractometer. XRD instrument settings were as follows:

- Generator = 45 kV.
- Current = 40 mA.
- Tube anode = Cu.
- Wavelength = 1.54060 \AA ($K_{\alpha 1}$) and 1.54443 \AA ($K_{\alpha 2}$).
- Step spacing = $0.005^\circ 2\theta$.
- Scan step time = 0.648 s.
- Divergent slit = automatic.
- Irradiated length = 10 mm.
- Scanning range = 2° – $60^\circ 2\theta$.
- Spinning = yes.

In order to maintain consistency with previous NanTroSEIZE results, we used the software MacDiff 4.2.5 for data processing (www.ccp14.ac.uk/ccp/ccp14/ftp-mirror/krumm/Software/macintosh/macdiff/MacDiff.html). We adjusted each peak's upper and lower limits following the guidelines shown in Table T6. Calculations of relative mineral abundance utilized a matrix of normalization factors derived from integrated peak areas and singular value decomposition (SVD). As described by Fisher and Underwood (1995), calibration of SVD factors depends on the analysis of known weight-percent mixtures of mineral standards that are appropriate matches for natural sediments. SVD normalization factors were recalculated during Expedition 315 after the diffractometer's high-voltage power supply and X-ray tube were replaced (Ashi et al., 2008), and the mixtures were rerun at the beginning of Expedition 319 (Table T7). Bulk powder mixtures for the Nankai Trough are the same as those reported by Underwood et al. (2003): quartz (Saint Peter sandstone), feldspar (Carich albite), calcite (Cyprus chalk), smectite (Camontmorillonite), illite (Clay Mineral Society IMt-2, 2M1 polytype), and chlorite (Clay Mineral Society CCa-2). Examples of diffractograms for standard mixtures are shown in Figure F9.

Average errors (SVD-derived estimates versus true weight percent) of the standard mineral mixtures are total clay minerals = 3.3%, quartz = 2.1%, plagioclase = 1.4%, and calcite = 1.9%. In spite of its precision with standard mixtures, the SVD method is only semiquantitative, and results for natural specimens should be interpreted with some caution. One of the fundamental problems with any bulk powder XRD method is the difference in peak response between poorly crystalline minerals at low diffraction angles (e.g., clay minerals) and highly crystalline minerals at higher diffraction angles (e.g., quartz and plagioclase). Clay mineral content is best characterized by measuring the peak area, whereas peak intensity may more accurately quantify quartz, feldspar, and calcite. Analyzing oriented aggregates enhances basal reflections of the clay minerals, but this is time consuming and requires isolation of the clay-size fraction to be effective. For clay mineral assemblages in bulk powders, the two options are to individually measure one peak for each mineral and add the estimates together (thereby propagating the error) or to measure a single composite peak at 19.4° – $20.4^{\circ}2\theta$. Other sources of error are contamination of mineral standards by impurities such as quartz (e.g., the illite standard contains ~20% quartz) and differences in crystallinity between standards and natural clay minerals. For trace quantities of a mineral and peaks with low intensity, use of negative SVD normalization factors may result in negative values of absolute weight percent. In such cases, we inserted the numerical value of 0.1% as a proxy for “trace.”

In the final assessment, calculated mineral abundances should be regarded as relative percentages within a four-component system of clay minerals + quartz + feldspar + calcite. How close those estimates are to their absolute percentages within the total solids depends on the abundance of amorphous solids (e.g., biogenic opal and volcanic glass), as well as the total of all other minerals that occur in minor or trace quantities. For most natural samples, the difference between calculated and absolute abundance percentage is probably between 5% and 10%. To compound the error, the XRD data from cuttings show effects of contamination by drilling fluids. The severity of these artifacts is especially obvious in the calculated values of percent calcite. We suspect this is a result of rapid precipitation of calcium carbonate from high-ph fluid coming from the drilling mud, although geochemistry data show a relatively constant pH of >10 during drilling (see “[Geochemistry](#)”), which cannot completely explain variations in calcite content downhole (see “[Lithology](#)” in the “Site C0009” chapter).

Clay mineral analysis

We also separated three different grain-size fractions from five bulk rock samples by sieving and centrifuging (>63 μm , 2–63 μm , and <2 μm). To calculate the rotation speed (rpm) and the running time (min) of the centrifuge, we used the SediTools software (R. Petschick, Geol. Palaeontolog. Institute, University of Frankfurt, Germany). The values were corrected for acceleration and deceleration times.

After 1–2 min of ultrasonic treatment in deionized water, we wet-sieved the samples in a 63 μm sieve to separate the sand/silt grain size from the clay fraction. The >63 μm fraction was dried in an oven at 50°C, and the remaining suspension was used for separating the <2 μm fraction. After another ultrasonic treatment for ~1–2 min, the samples were centrifuged for 3 min at 1000 rpm. The suspension contained the <2 μm grain-size fraction, and the solid material contained the 2–63 μm grain sizes. All samples were then oven-dried at 50°C, and ~0.5 mg of the resulting powder was mixed with ~1.5 mL of deionized water, treated ultrasonically for ~1 min, and placed on an XRD glass sample holder with a pipette. After drying, the samples were analyzed by XRD.

X-ray fluorescence

We performed whole-rock quantitative XRF spectrometry analysis for major elements on cuttings and on core material. The 1–4 mm size fraction of cuttings samples was used for these measurements. Samples of 10 cm³ were taken from the working half of the core next to samples for XRD analysis. Major elements were measured using the fused glass bead method and are presented as weight percent oxide proportions (Na₂O, MgO, Al₂O₃, SiO₂, P₂O₅, K₂O, CaO, TiO₂, MnO, and Fe₂O₃). An aliquot of 0.9 g of ignited sample powder was fused with 4.5 g of SmeltA12 flux for 7 min at 1150°C to create glass beads. Loss on ignition was measured using weight changes on heating at 1000°C for 3 h. Analyses were performed on the wavelength dispersive XRF spectrometer Supermini (Rigaku) equipped with a 200 W Pd anode X-ray tube at 50 kV and 4 mA. Analytical details and measuring conditions for each component are given in Table T8. Rock standards of the National Institute of Advanced Industrial Science and Technology (Geological Survey of Japan) were used as the reference materials for quantitative analysis. Table T9 lists the results and standard deviations for selected standard samples. A calibration curve was created with matrix corrections provided by the operating software, using the average content of each component. Processed data were uploaded into J-

CORES and are shown in Figure F20 in the “Site C0009” chapter (see also C0009_T4.XLS in LITHOLOGY in “Supplementary material”).

Grain size separation (Atterberg method)

To estimate the sand (>63 μm), silt (2–63 μm), and clay (<2 μm) fraction in the cuttings, we separated these fractions by sieving and settling methods (Atterberg method). The conventional Atterberg method is used for separating grain size fractions according to their settling velocity. After the sample was poured into a sedimentation cylinder, deionized water was added up to the desired settling height. The closed cylinder was shaken until the suspension was homogeneous. When the necessary settling time for a given equivalent diameter (e.g., 2 μm) was reached (calculated according to Stokes law), the supernatant suspension (e.g., only material <2 μm) was decanted and dried. In order to achieve optimal separations, this procedure should be repeated up to 15 times. However, because of restricted time, it was repeated only three times during this expedition.

We note that the percentage of “total clay” of the 1–4 mm fraction measured by XRD (45 wt%) is higher than the clay-size fraction determined by the Atterberg method on unwashed cuttings (24%). Our preliminary interpretation is that samples used in Atterberg analysis contained nondisaggregated agglomerates of silty clay that were not disaggregated during shaking, leading to underestimation of the fine-grained fraction. Mixing with drilling mud may also contribute to this effect.

Identification of lithologic units

At Site C0009, we used logging data in conjunction with analyses of core and cuttings to identify lithologic units and boundaries. We identified compositional and textural attributes of the formation mainly using nuclear (gamma ray, density, and PEF) and sonic logs along with data from cuttings and core where available. After evaluating log data quality through the examination of the potential effects of borehole diameter, borehole conditions, and drilling parameters, we defined units using changes in log responses interpreted to reflect differences in rock properties. For this analysis, natural- and induced-radioactivity logs, sonic logs, and resistivity logs were the main input. Integrated interpretation of all the available logs focused on (1) definition and characterization of units and unit boundaries, (2) identification of composition and physical properties within each unit, and (3) interpretation in terms of geological features (unit bound-

aries, transitions, sequences, and likely lithologic composition). These data are shown in Figure F19 in the “Site C0009” chapter.

At riserless Sites C0010 and C0011, we collected a limited suite of LWD/MWD data (gamma ray and RAB, including resistivity images); operations at these sites did not include recovery of core or cuttings. At Site C0010 we identified the major units and boundaries using gamma ray and resistivity data and by comparison with previously drilled nearby IODP Site C0004 (3.5 km to the northeast along strike), where a more extensive suite of LWD data and coring were used to define logging and lithologic units during IODP Expeditions 314 and 316 (Kinoshita et al., 2008; Kimura et al., 2008).

Structural geology

At Site C0009, two groups of sample materials were used for structural geology analysis: (1) cuttings (>4 mm fraction) sampled at 5 m intervals between 1097.7 and 1512.7 m MSF during drilling of Hole C0009A, and (2) core recovered between 1507.7 and 1593.9 m CSF from Hole C0009A. We did not study the structure preserved within cuttings from the cored interval. In addition to sample materials, we analyzed wireline FMI resistivity images and caliper log data for structure and geomechanics analysis from 703 to 1580 m WMSF at Site C0009. At Site C0010, only RAB images and associated log curves were used for structural interpretation.

Cuttings

Cuttings from Hole C0009A were studied with a binocular microscope. Approximately 20 cutting fragments were selected from the >4 mm size fraction at each 5 m depth interval; smaller fragments were not large enough to systematically recognize structures. Structures recognized include slickenlined surfaces (or slickensides), vein structures, and web structures (see “Structural geology” in the “Site C0009” chapter). The depth of each cuttings sample is recorded as the top of the 5 m interval from which it was collected.

Cores

Structures preserved in the core were documented through visual inspection of split cores and in optical thin sections. Detailed structural data were only collected on split cores. The data were hand logged onto a printed form at the core table and then transferred to both a spreadsheet and the J-CORES database. Core observations and measurements followed

procedures of previous ODP expeditions (e.g., ODP Legs 131, 170, and 190). We used a modified plastic protractor to collect orientation data (Fig. F10) and noted results on a descriptive core log. Symbols for structures were entered on VCD sheets.

Following techniques developed on Leg 131 (Shipboard Scientific Party, 1991) and refined during Expedition 315 (Expedition 315 Scientists, 2009), orientations of planar and linear features in cored sediments were determined relative to the core axis, which represents vertical in the core reference frame, and the “double line” marked on the working half of the split core liner, which represents north (or 0° and 360°) in the core reference frame (Fig. F11). To determine the orientation of a plane, two apparent dips of the planar feature were measured in the core reference frame and used to define either a strike and dip or a dip and dip direction. This conversion was accomplished using a spreadsheet, as described in **“Structural geology spreadsheet.”** One apparent dip of a planar feature was measured on the split face of the core with a dip direction and angle in the core reference frame. Apparent dip direction measurements on this core face had a trend of 90° or 270° and ranged in plunge from 0° to 90° (Fig. F11). The second apparent dip was usually measured on a cut or fractured surface at a high angle to the split face of the core (core face). In many cases this was a surface at 90° to the cut core face and either parallel or perpendicular to the core axis. In the former cases, the apparent dip lineation would trend 0° or 180° and plunge from 0° to 90°; in the latter cases, the trend would range from 0° to 360° and plunge 0°. Linear features observed in the cores were always associated with planar structures (typically faults or shear zones), and their orientations were determined by measuring either the trend and plunge in the core reference frame or the rake (or pitch) on the associated plane. All data were recorded on the log sheet with appropriate depths and descriptive information.

We observed a range of deformation structures in Expedition 319 cores (see **“Structural geology”** in the “Site C0009” chapter). Most can be classified as one of three types of structures: shear zones, faults, and slickenlined faults. We also logged bedding, a few sets of “vein structures” (Brothers et al., 1996; Cowan, 1982; Ogawa, 1980), and a range of other structures (e.g., fabrics defined by deformed trace fossils), though we did not measure the orientations of these other structures.

Borehole image data

Borehole resistivity imaging tools run during Expedition 319 also provide an in situ view of structural features. At Site C0009, the FMI wireline logging tool was run in the lower part of the hole (703.9–1580 m WMSF). This tool provides resistivity images with a spatial resolution up to 5 mm, but the four resistivity pads cover only part (~50%) of the interior of the borehole. At Site C0010, borehole images were acquired using the LWD geoVISION resistivity tool. This tool is based on RAB technology, which provides an image of the entire interior of the borehole while drilling (see **“Logging”** for information on image resolution). A 4 cm electrode is located 102 cm from the bottom of the tool and provides a focused lateral resistivity measurement (ring resistivity) with a vertical resolution of ~5–7.5 cm (Expedition 314 Scientists, 2009). Both the FMI and the RAB images are oriented with respect to north. All resistivity images were interpreted using GeoFrame and GMI Imager software to record the orientation of beds, faults, and various borehole failure features (see Expedition 314 Scientists, 2009). Caliper magnitude and orientation were used to determine borehole shape downhole to assess stress orientations.

Data analysis

Structural geology spreadsheet

A spreadsheet, developed and used during Expedition 315, was used to calculate orientation data in the core reference frame (Expedition 315 Scientists, 2009). This spreadsheet takes observations of apparent dips and determines the true dip of the feature in the core reference frame.

During rotary core barrel drilling, the core rotates with respect to the true geographic reference frame and individual core pieces undergo rotation during drilling, recovery, and preparation for visual descriptions. Thus, a correction routine is required to rotate structures from the core reference frame to the geographic reference frame. On previous expeditions (e.g., Expedition 315), paleomagnetic data were used to correct drilling-induced rotations of these coherent intervals. For Expedition 319, the cryogenic magnetometer was unavailable. However, paleomagnetic measurements were made during Expedition 322 on archive-half cores, and preliminary results are reported in **“Paleomagnetism”** in the “Site C0009” chapter. Reorientation using paleomagnetic constraints remains for postexpedition research.

Data recording

Structural data entered in the J-CORES database VCD program include a visual (macroscopic and/or microscopic) description of core structures at a given section index. Orientation data were entered into a spreadsheet separately for postacquisition processing.

Anisotropy of magnetic susceptibility

During Expedition 319, the physical properties group collected AMS from the “pmag” cubes (see “[Physical properties](#)”). The magnetic susceptibility (k_{ij}) is produced by the application of a magnetic field (H_j) to the natural magnetic remanence (M_i):

$$M_i = k_{ij} \times H_j. \quad (3)$$

By measuring the magnetic susceptibility in three directions (by rotating the sample within the Kappa-bridge), one can measure the three principal axes (k_{\max} , k_{int} , and k_{\min}) of the AMS ellipsoid. The resulting AMS ellipsoid is then interpreted as resulting from preferred orientations (or in some instances distribution) of micrometer to submicrometer magnetite grains and/or other paramagnetic phases. Because of the fine-grained nature of materials in the cored sediment, the AMS ellipsoid is thought to be roughly proportional to finite strain in both direction and magnitude (Housen, 1997).

The AMS spreadsheet (see C0009_T1.XLS in STRUC-GEOL in “[Supplementary material](#)”) reports the mean magnetic susceptibility (k_{mean}), k_{\max} , k_{int} , and k_{\min} , and three statistics that describe the AMS ellipsoid (P , L , and F):

$$k_{\text{mean}} = (k_{\max} + k_{\text{int}} + k_{\min})/3, \quad (4)$$

$$P = k_{\max}/k_{\min}, \quad (5)$$

$$L = k_{\max}/k_{\text{int}}, \text{ and} \quad (6)$$

$$F = k_{\text{int}}/k_{\min}. \quad (7)$$

The spreadsheet also has columns in which to determine the geographic orientation of the AMS ellipsoid given paleomagnetic data.

Biostratigraphy

Calcareous nannofossils

During Expedition 319, only calcareous nannofossils were used to date core catcher and cuttings samples. When necessary, we took and examined additional samples from the cores to further refine ages. We

report the depth of each cuttings sample referring to its bottom depth (i.e., the bottom of the 5 m sampling interval).

Zonation and biohorizons

For Expedition 319, we applied a biostratigraphic zonation of calcareous nannofossils based on the zonal schemes of Martini (1971) and Okada and Bukry (1980) that were modified by Young (1998). Our application of zonal markers and additional datums follows Expeditions 315 and 316 for biostratigraphic consistency and subsequent correlation (see “[Biostratigraphy](#)” in Expedition 315 Scientists, 2009, and Expedition 316 Scientists, 2009).

Each nannofossil datum was assigned an astronomically calibrated age based on Raffi et al. (2006). The astrochronological frame for the Neogene and Quaternary follows the International Commission on Stratigraphy (ICS) 2004 timescale (Lourens et al., 2004). The timescale and biostratigraphic zones of calcareous nannofossils are summarized in Figure [F12](#) and Table [T10](#).

Downhole contamination common in cuttings often poses problems in recognition of a zonal boundary defined by a first occurrence (FO) datum because such a boundary may stratigraphically appear significantly lower than its in situ location. To circumvent this problem, a last occurrence (LO) datum stratigraphically close to the FO, if available, was selected to approximate the zonal boundary; otherwise, the biozone was combined with adjacent zones. In addition, though some FO datums can be considered in situ if observed in normal biostratigraphic order as constrained by LO datums, many FO datums listed in Figure [F12](#) may not be reliable in cuttings. The unreliability of FO datums in cuttings reduces the resolution of biostratigraphy.

We applied two additional criteria to resolve the reworking of zonal markers, which tends to make the assemblage appear older. First, we defined a datum based on the continuous occurrence of a taxon, whereas its sparse occurrence is considered reworked. Second, we used changes in assemblage composition and specimen size to evaluate the occurrence of zonal markers.

Taxonomic remarks

Taxonomy followed the compilation of Perch-Nielsen (1985) and Young (1998). Previous work (Raffi et al., 1993, 2006; Raffi, 2002) suggested grouping species in the genus *Gephyrocapsa* by size. This is because *Gephyrocapsa* species show a great variability in size and other morphological features (e.g., relative size of the central opening and

orientation of the bar), creating discrepancy in identification among different authors (Su, 1996). Accordingly, *Gephyrocapsa* is divided into four major groups by maximum coccolith length: small *Gephyrocapsa* (<3.5 μm), medium *Gephyrocapsa* I (3.5–4 μm), medium *Gephyrocapsa* II (4–5.5 μm), and large *Gephyrocapsa* (≥ 5.5 μm). Some important morphologic features (e.g., bar orientation) were also considered during the analysis. In addition, *Reticulofenestra pseudumbilicus* should have a coccolith length >7 μm .

Sample preparation and analysis

We prepared smear slides from cuttings sampled at 5–30 m spacing and core catcher samples within the cored interval, following the standard method with photocuring adhesive as a mounting medium. A simple concentration technique was adopted from Expedition 316 (see “Biostratigraphy” in Expedition 316 Scientists, 2009) for samples that contained coarse materials or few to rare nanofossils. This technique involves suspending and settling sediments in distilled water to remove sands and silts before making smear slides.

In addition, we used a “mixing” technique for cuttings samples in order for the subsamples to better represent the 5 m sampling interval. We soaked >20 g of drilling mud-sediment mixture (when no hard rock pieces were present) or clean chips with ridges in distilled water, stirred to disaggregate rock chips (ground with a mortar and pestle when needed), and suspended the sample materials. The suspension was allowed to settle for 60 s, and then we drew ~3 mL of the suspension using a transfer pipet for making standard smear slides.

Slides were examined using a Zeiss Axio Imager.A1m microscope under cross-polarized light and transmitted light at 1250 \times magnification. A Joel JCM-5700 Carry Scope scanning electron microscope was employed to confidently identify *Emiliana huxleyi*.

We estimated relative abundances of individual species/genus and assemblages based on observations from a traverse at 1250 \times magnification that generally parallels the long axis of the slide. Usually more than three traverses were browsed for zonal markers and rare species, and >600 fields of view (FOVs) were examined per sample. A letter code was given to each abundance category and defined as follows:

- V = very abundant (>10 specimens/FOV).
- A = abundant (1–10 specimens/FOV).
- C = common (1 specimen per 2–10 FOVs).
- F = few (1 specimen per 11–100 FOVs).
- R = rare (1 specimen per 101–500 FOVs).

B = barren (no nanofossils per >500 FOVs; for assemblage abundance only).

The average preservation state of the nanofossil assemblage in each sample was qualitatively categorized and defined as follows:

- VG = very good (no evidence of dissolution and/or overgrowth; no alteration of diagnostic characteristics; all specimens identifiable at the species level).
- G = good (little or no evidence of dissolution and/or overgrowth; only slight alteration of diagnostic characteristics; most specimens [~95%] identifiable at the species level).
- M = moderate (evident etching and/or overgrowth; diagnostic characteristics sometimes altered; broken specimens frequent and delicate forms decreased; however, the majority of specimens identifiable at the species level).
- P = poor (severe dissolution, fragmentation, and/or overgrowth; diagnostic characteristics largely destroyed; many specimens [>50%] not identifiable at the species and/or generic level).

We recorded abundance, preservation, and bioevents for each sample in the J-CORES database. Some additional samples from core sections were scanned only for biostratigraphic zonal markers without recording the abundances of the entire assemblage. These samples were not included in the range chart but may be included in the nanofossil event list.

Geochemistry

Mud gas monitoring

Expedition 319 was the first IODP cruise that conducted real-time drilling mud gas extraction and analysis in addition to sampling for postexpedition studies (e.g., noble gas and stable isotopes) using a system developed at the Deutsches GeoForschungs-Zentrum (GFZ) (Erzinger et al., 2006). This section provides a short description of the online drilling mud gas extraction system and analyses performed during Expedition 319. More detailed explanations of technical aspects of scientific drilling mud gas monitoring can be found in Erzinger et al. (2006).

Gas extraction

The gas dissolved in the returning drilling mud was extracted under a slight vacuum using a custom built water-gas separator (Fig. F13). The separator consists of a steel cylinder with an explosion-proof 220 V electrical motor above the cylinder, which drives a stirring impeller mounted inside the cylinder. In

contrast to commercially built gas separators, the separator used during Expedition 319 is not permanently flushed with air because this could lead to contamination by atmospheric gases prior to sampling and analysis. This is important for gas species that might be only slightly enriched in the formation compared to their atmospheric concentration (e.g., helium). Nevertheless, when making a new pipe connection, the mud flow was stopped and the separator was exposed to air for a short time.

A membrane pump was used to create a vacuum and pump the extracted gas through a polyethylene tube (3 mm inner diameter, 9 mm outer diameter) into a laboratory trailer, which was installed on deck (Fig. F13). The flow rate was adjusted to between 1 and 2 L/min, which resulted in a traveltime of <2 min. Wiersberg and Erzinger (2007) showed that because of the short gas traveltime, diffusion loss along the gas line is negligible. The gas space in the separator head depends on the mud level and the applied vacuum, which was ~20 mbar below ambient air pressure. When the amount of extracted gas was small, the mud would rise in the separator tank because of the vacuum and enter the gas line. In this case, a condensation trap placed directly behind the separator acted as a security valve and opened the separator to the atmosphere.

During drilling of the 12¼ inch hole from 703 to 1510 m MSF (drilling Phase 2 operations; see C0009_T1.XLS in GEOCHEM in “[Supplementary material](#)”), the gas separator was placed in the bypass between the gumbo shakers and close to the outlet of the mud flow line in order to minimize air contamination and degassing of the drilling mud before reaching the separator (Fig. F14). With an average ROP of 20–30 m/h, it took ~1.5–2 h to make a new pipe connection, during which time the degasser was exposed to air. With a separator headspace volume of ~30 L and gas pumping rate of 1–2 L/min, it took up to 1 h to fully exchange the gas volume after air flushing, particularly when the gas composition of drilling mud significantly differed from air. The low gas exchange rate in the separator headspace volume in combination with a high gas load of the drilling mud resulted in smoothing of peaks in gas composition. The uncertainty in depth of origin is estimated at ±20 m during this drilling phase.

To obtain data at higher spatial resolution, a smaller separator was chosen (headspace volume ~10 L) during coring (drilling Phase 3) and hole opening procedures (drilling Phase 8 operations; see C0009_T2.XLS in GEOCHEM in “[Supplementary material](#)”). Furthermore, the separator was moved from the bypass between the gumbo shakers to the mudline in front

of the shale shakers (Fig. F49 in the “Site C0009” chapter). Between the gumbo shakers, the separator could only be placed directly in front of the mudline outlet pipe, where a strong mud flow caused an effect similar to a water-jet pump. When drilling strata with low gas concentration, the separator did not produce gas but instead drew it from the line. The reduced headspace volume and different positioning of the separator improved the resolution of gas sample locations to ±10 m during Phase 8, to ~1260 m MSF. Below ~1260 m MSF, the ROP was significantly increased and the gas-loaded drilling mud was not circulated out, resulting in consistently high background methane. In addition, because of the lower mud weight during Phases 2 and 3 relative to Phase 8, the gas concentrations are higher during these phases. Commercial safety gas monitoring during the same period shows the same trend of lower gas concentrations during Phase 8. Although gas concentrations are different during the two phases, trends with depth are comparable.

Gas analysis

In the laboratory trailer (Fig. F13, right), residual water gas was condensed in a trap installed behind the membrane pump before the gas entered the analytical devices. Prior to gas analysis, the dried gas flowed through a sampling device. This sampler collected up to four gas samples from the gas line in glass cylinders and copper tubes for postexpedition laboratory and isotope analysis. The sampler is remotely controlled by the mass spectrometer; a remote signal is given when a preset threshold concentration of a given type of gas is exceeded. The sampler is equipped with a bypass line to make sure that gas flow to the analytical devices continues even after all samples are taken.

After passing through the sampler, the gas was analyzed by a gas mass spectrometer and a gas chromatograph (GC). Concentrations of N₂, O₂, Ar, CO₂, CH₄, He, and H₂ were determined using an OmniStar (Pfeiffer Vacuum, Germany) quadrupole mass spectrometer (QMS). The QMS requires a gas flux of ~30 mL/h of gas. A complete QMS analysis with detection limits of 1 parts per million by volume (ppmv) for He, H₂, CH₄, and Ar, as well as 10 ppmv for O₂, N₂, and CO₂ was achieved with this setup after an integration time of 16 s. However, a 1 min sampling interval was chosen to reduce the amount of data produced. Hydrocarbons (CH₄, C₂H₆, C₃H₈, i-C₄H₁₀, and n-C₄H₁₀) were analyzed only during Phase 8 at 10 min intervals with an automated standard field GC (SRI 8610) equipped with a flame ionization detector (FID). Detection limits for the hydrocarbons

are ~1 ppmv. In addition, electrical conductivity, pH, and temperature of the returning drilling mud were determined continuously at 5 min intervals during all drilling phases.

After acquisition, data were corrected for artifacts (e.g., connection gas, trip gas) and correlated to the lag depth that takes into account the traveltime of the drilling mud from the drill bit to the surface. Lag time and resulting lag depth were calculated by the mud logging company from the borehole volume and mud pump rate (strokes) and cross-checked by carbide tests twice during drilling operations.

Several analytical instruments (GC, radon detector, one of two mass spectrometers) as well as one hydrogen generator and one computer failed before and/or during drilling. For some of those incidents, a link between failure and apparent fluctuation in the power supply is likely, suggested by simultaneous failure. Hence, a clean power supply independent from rig power is highly recommended for possible future use of this experimental setup.

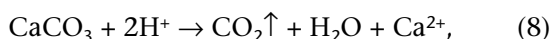
Organic geochemistry

Sample preparation

Inorganic carbon, TC, and TN were determined for 111 cuttings samples (1–4 mm fraction) from 1037.7 to 1592.7 m MSF and for 34 core samples from 1509.8 to 1591.5 m CSF. Prior to sample analysis, cuttings material (~10 cm³) was washed with seawater and deionized water, sieved, freeze-dried, and ground to powder (see “[Cuttings handling](#)”). Core material (~10 cm³) was only dried and ground.

Inorganic carbon

Inorganic carbon was measured using a Coulometrics 5012 CO₂ coulometer. Approximately 10–12 mg of freeze-dried powder was weighed and treated with 2M HCl. The released CO₂ was titrated, and the change in light transmittance was measured with a photodetection cell. The weight percent of calcium carbonate was calculated from inorganic carbon content, assuming that all extracted CO₂ was derived from dissolution of calcium carbonate according to the reaction



by the following equation based on molecular weight ratio:

$$\text{CaCO}_3 = 8.33 \times \text{inorganic carbon}. \quad (9)$$

It is assumed that all carbonate minerals were composed of CaCO₃. The standard deviation based on 63 reference measurements was less than ± 0.71%.

Total carbon and nitrogen

TC and TN concentrations were determined using a Thermo Finnigan Flash EA 1112 CHNS analyzer. Calibration was performed using the synthetic standard sulfanilamide, which contains C (41.81 wt%) and N (16.27 wt%). About 10–20 mg of freeze-dried sample powder was weighed and placed in a tin container for carbon and nitrogen analyses. The samples were combusted at 1000°C in an oxygen stream. NO_x were reduced to N₂, and the mixture of CO₂ and N₂ was analyzed by a GC equipped with a thermal conductivity detector. Total organic carbon was calculated by subtracting inorganic carbon from TC. Standard deviation of carbon and nitrogen is less than ±0.1%. The analytical accuracy for carbon was determined with 0.188 ± 0.014 wt% for N and 0.1755 ± 0.014 wt% for C, using Soil NCS reference material with 0.195 wt% N and 0.176 wt% C.

Interstitial water geochemistry

Interstitial water extraction

Interstitial water samples were obtained from 35–46 cm long whole-round core sections. Whole-round sediment samples were cut from each core at the core cutting area and then immediately transferred to the CT laboratory to be scanned for important features such as lithologic boundaries and structures and to confirm that the section was relatively homogeneous and unfractured. The sample was then taken to the quality assurance/quality control laboratory and was extruded from the core liner in a nitrogen-flushed glove bag. In the glove bag, each sediment sample was cleaned to prevent drilling contamination (e.g., seawater, drilling fluid). The cleaned residual sediment was placed in a Manheim-type titanium squeezer (Manheim, 1966). If all pore water squeezers were in operation, the samples were stored at 4°C prior to extrusion; in all cases, squeezing started within 24 h of receiving core on deck.

Because of the small amount of water extracted from the samples, two squeezers were filled with the maximum amount of sample material and then manually presqueezed to obtain filter cakes. Filter cakes were then placed together in one squeezer for automatic squeezing. The squeezing procedure comprised 10 min of squeezing with 15,000 lb (pound-force), 100 min of squeezing with 20,000 lb, and

final squeezing with 24,000 lb until 4 cm³ of pore water was extracted. Squeezing times are reported in Table T12 in the “Site C0009” chapter.

Collected interstitial water was passed through two rinsed filter papers fitted with 2–4 300 mesh stainless steel screens at the base of the squeezer. Fluids from the squeezing process were then passed through a 0.45 μm disposable filter into an acid-washed (10% HCl) 50 mL plastic syringe. Because of the small volumes obtained, interstitial water was sampled for shipboard analyses only. High-density polyethylene (HDPE) sample vials intended for minor and trace element analysis were cleaned by immersion in 55°C 10% trace metal grade 12N HCl for a minimum of 24 h, rinsed with Millipore 18.2 MΩ·cm Type 1 ultrapure (Milli-Q) water, and then dried in a class 100 laminar flow clean hood. All samples designated for shipboard minor and trace element analysis were acidified with 6N HCl with a ratio of 4 mL of 6N HCl per liter of sample for at least 24 h. This was followed by either inductively coupled plasma–atomic emission spectroscopy (ICP-AES) or inductively coupled plasma–mass spectrometry (ICP-MS) analysis to dissolve any metallic oxide precipitates that may have formed after squeezing.

Interstitial water analysis

Because of the limited amount of water extracted from core (~4 cm³ per sample), not all standard shipboard analyses could be performed. Determination of alkalinity and pH was not carried out, as these measurements alone would have required 3 cm³ sample volume. Interstitial water samples were analyzed for salinity by an Atago RX-5000α refractometer. The refractive index was converted to salinity based on repeated analyses of International Association of Physical Sciences of the Oceans (IAPSO) standard seawater. Precision for the refractive index measurement was ±0.0004. Chlorinity was determined from the interstitial water samples using a Metrohm autotitrator and silver nitrate solution as a titrant. The relative standard deviation for chlorinity is ±0.15%. The average precision of the chlorinity titrations, expressed as 1σ standard deviation of means of multiple determinations of IAPSO standard seawater, is ±0.15%.

Sulfate and bromide concentrations were measured with a Dionex ICS-1500 ion chromatograph (IC) using subsamples that were diluted 1:100 (10 μL in 990 μL) with Milli-Q water. This dilution provided quality peak detection for chloride, bromide, and sulfate. Because of the high chloride concentration, these data were used only to check the quality of the dilu-

tion step. IAPSO standard seawater aliquots (2.5, 5, 7.5, and 10 μL in a total of 1000 μL) were analyzed at the beginning and end of each run for quality control and to monitor potential drift in sensitivity throughout a particular run. The average precision of the sulfate and bromide analyses were ±2.3% for sulfate and ±5.7% for bromide, expressed as 1σ standard deviation.

The concentrations of certain major cations (Mg²⁺, Ca²⁺, Na⁺, and K⁺) were determined with an ICS-1500 IC equipped with a cation exchange column. Samples were acidified with HCl (Tamapure-AA-110 grade) in 0.4% of the sample volume and then diluted by a factor of 200 using a Hamilton diluter. The samples were then placed in an autosampler together with five calibration solutions and two blank solutions (Milli-Q water). For quality checks, a 1:200 solution of diluted IAPSO standard seawater was measured every eight samples. In order to determine the concentration of each ion, measurements of a standard material were performed to obtain calibration curves from the measured peak area and the known concentration. A standard solution containing Li⁺ (0.5 mg/L), Na⁺ (2 mg/L), NH₄⁺ (2 mg/L), K⁺ (5 mg/L), Mg²⁺ (5 mg/L), and Ca²⁺ (5 mg/L) was diluted to five standard solutions (10%, 25%, 50%, 75%, and 100%). The resulting precision for the measurements was ±0.4 for Na⁺, ±1.7% for K⁺, ±2.8% for Mg²⁺, and ±1.3% for Ca²⁺.

Minor element B, Ba, Fe, Li, Mn, Si, and Sr concentrations were determined by ICP-AES (Horiba Jobin Yvon Ultima2). To analyze these elements, 0.5 mL of sample solution was added to 9.5 mL of ultrapure bidistilled nitric acid solution and spiked with 10 ppm Y solution as an internal standard. Because of the high concentration of matrix salts in the interstitial water samples at a 1:20 dilution, matrix matching of the calibration standards is necessary to achieve accurate results by ICP-AES. A matrix solution that approximated IAPSO standard seawater major element concentrations was prepared from the following salts in 1 L of Milli-Q water acidified with 4 mL of optima-grade 6N HCl: 26.90 g NaCl, 3.81 g MgCl₂, 1.00 g CaCO₃, and 0.75 g KCl. Blanks were measured using a dilution of 1% nitric acid solution in the Y solution where only the slope of the calibration curve was used for quantification.

A stock standard solution was prepared from ultrapure primary standards (SPC Science PlasmaCAL) in the 1% nitric acid solution, and then diluted in the same 1% ultrapure nitric acid solution used for pore water samples to concentrations of 50%, 25%, 10%, 5%, and 1%. A 1.25 mL aliquot of each stock solu-

tion was added to 8.75 mL of matrix solution to generate a series of standards that could be diluted using the same method as the samples for consistency.

The final matrix-matched 100% standard solution contained the following concentrations of elements: B = 3000 μM , Li = 400 μM , Si = 1000 μM , Mn = 50 μM , Fe = 50 μM , Sr = 400 μM , and Ba = 200 μM . Because values of many of these elements in IAPSO standard seawater are either below detection limits (e.g., Fe and Mn) or variable, a standard prepared in the 10% matrix-matching solution was repeatedly analyzed to calculate the precision of the method. Relative standard deviations were $\pm 0.8\%$ for B, $\pm 0.5\%$ for Ba, $\pm 2.3\%$ for Fe, $\pm 3.1\%$ for Li, $\pm 1.5\%$ for Mn, $\pm 2.0\%$ for Si, and $\pm 1.4\%$ for Sr.

V, Cu, Zn, Mo, Rb, Cs, Pb, and U were analyzed by ICP-MS (Agilent 7500ce ICP-MS) equipped with an octopole analyzer to reduce isobaric interferences from polyatomic and double-charged ions. To calibrate for interferences between some of the transition metals (V, Cu, and Zn) and some major element oxides, solutions containing these elements were prepared with concentrations similar to IAPSO standard seawater values. These solutions were analyzed at the beginning of each measurement, and an interference correlation was applied based on the average ion counts per second (cps) measured on the standard solutions divided by the abundance of the interfering elements. This ratio was multiplied by the known concentration of the major ions in the samples based on previous analysis, and the result was then subtracted from the measured counts (cps) of the sample.

A 100 μL aliquot of 500 parts per billion (ppb) indium standard was added before further dilution. Aliquots of 150 μL of this sample solution were then diluted with 4.85 mL of 1% HNO_3 based on previous determination of the detection limits and the low concentrations of the elements of interest. A primary standard solution was made that matched the maximum range of predicted concentrations based on published results of deep-sea pore fluid compositions in a variety of settings. The composition of the standard is as follows: V = 20 ppb; Cu, Mo, Pb, and U = 40 ppb; Zn = 140 ppb; Rb = 500 ppb; and Cs = 5 ppb.

This primary standard was then diluted with 1% nitric acid solution to relative concentrations of 50%, 25%, 10%, 5%, and 1%. A 0.15 mL aliquot of these standards was then further diluted by addition of 0.15 mL of a 560 mM NaCl solution and 4.7 mL of 1% HNO_3 solution to account for matrix suppression of the plasma ionization efficiency. The 25% standard was diluted accordingly and analyzed together every eight samples throughout each analysis series for precision and in order to correlate the results

from different analysis dates. Blanks were also analyzed every eight samples, and detection limits were determined to be three times the standard deviation of a procedural blank of Milli-Q water acidified with 4 mL of optima-grade 6N HCl per liter. The average precision of multiple determinations of the 10% ICP-MS standard was $\pm 1.7\%$ for ^{51}V , $\pm 3.6\%$ for ^{66}Zn , $\pm 1.2\%$ for ^{85}Rb , $\pm 10.5\%$ for ^{95}Mo , $\pm 0.5\%$ for ^{133}Cs , and $\pm 3.6\%$ for ^{238}U .

Physical properties

Physical property measurements provide basic information to assess rock and sediment properties, to characterize lithologic units and states of consolidation and deformation, and to correlate core, cuttings, and downhole measurement and logging data. For the cored intervals, X-ray CT images were first taken of core sections. Then, gamma ray attenuation (GRA) density, magnetic susceptibility, natural gamma radiation, *P*-wave velocity, and electrical resistivity were measured for whole-round core sections (MSCL-W) using the multisensor core logger (MSCL) system (Geotek Ltd., London, United Kingdom) after 3 h of thermal equilibration at room temperature. After MSCL-W measurements, thermal conductivity measurements were carried out on the working half of split cores using the half-space method. Digital photo image scanning was carried out on the cut surfaces of archive halves using the MSCL-I. MAD were measured on discrete samples collected from core working halves. *P*-wave velocity was measured in three orthogonal directions on 20 mm cubic samples. For cuttings samples (700–1605 m MSF) of Hole C0009A, GRA was measured by MSCL-W, MAD measurements were conducted, and magnetic susceptibility was measured using the Kappabridge system. Details about each measurement are given in the following sections.

MSCL-W (cores and cuttings)

Gamma ray attenuation density

A thin gamma ray beam was produced by a ^{137}Cs gamma ray source at a radiation level of 370 MBq within a lead shield with a 5 mm collimator. The gamma ray detector is composed of a scintillator and an integral photomultiplier tube. Bulk density was computed from GRA as follows:

$$\rho = 1/(\eta d) \times \ln(I_0/I), \quad (10)$$

where

ρ = sediment bulk density,
 η = Compton attenuation coefficient,

d = sample diameter,
 I_0 = gamma source intensity, and
 I = measured intensity of gamma rays passing through the sample.

Because η and I_0 are treated as constants, ρ can be calculated from I . For calibration, we used a set of aligned aluminum cylinders of various diameters, surrounded by distilled water in a sealed core liner. Gamma ray counts were taken through each cylinder for a period of 4 s, and $\ln(I)$ was plotted against ηd . For the calibration cylinders, ρ was 2.71 g/cm³ and d was 1, 2, 3, 4, 5, or 6 cm. The relationship between I and ηd can be expressed as follows:

$$\ln(I) = A(\eta d)^2 + B(\eta d) + C, \quad (11)$$

where A , B , and C are coefficients determined during calibration. For cores and cuttings, density measurements were conducted every 4 cm. The spatial resolution was 5 mm (collimator diameter), so each data point reflects the properties of the surrounding 5 mm interval.

P-wave velocity

P-wave velocity (V_p) was measured for discrete core samples in a time-of-flight mode, by measuring sonde length and traveltimes:

$$V_p = d/t, \quad (12)$$

where

d = distance traveled through the core, and
 t = traveltimes through the core.

P-wave velocity transducers are mounted on the MSCL system and measure d and t perpendicular to core axis at each measurement point. Total travel-time measured between the transducers includes three types of correctable delays:

t_{delay} = delay related to transducer contact faces and electronic circuitry,
 t_{pulse} = delay related to the peak detection procedure, and
 t_{liner} = transit time through the core liner.

The effects of delays are calibrated using a core liner filled with pure water. For routine measurements on whole-round cores in core liners, the corrected core velocity can be expressed by

$$V_{\text{pcore}} = (d'_{\text{core}} - 2d_{\text{liner}}) / (t_{\text{total}} - t_{\text{pulse}} - t_{\text{delay}} - 2t_{\text{liner}}) \times 1000, \quad (13)$$

where

V_{pcore} = corrected velocity through core (m/s),
 d'_{core} = measured diameter of core and liner (mm),

d_{liner} = liner wall thickness (mm), and
 t_{total} = measured total travel time (μ s).

Electrical resistivity

The bulk electrical resistivity (R_e) of a core of length (L) and cross-section area (S) at constant temperature can be expressed as

$$R_e = R(S/L), \quad (14)$$

where R is electrical resistance. The bulk resistivity of sediments and rocks is lower than that of its solid parts (the rock matrix) because of the presence of relatively high conductivity fluids. The effect of pore fluid on bulk resistivity depends on whether the fluid-filled pores are connected. The bulk electrical resistivity of a fluid-filled sediment relative to that of the pore fluid alone is described by an apparent formation factor F_a (Archie, 1947),

$$F_a = R_e/R_f, \quad (15)$$

where R_f is the resistivity of the pore fluid. Values of F_a include the effect of grain-surface conductivity and thus do not represent the true formation factor, $F = \tau^2/\phi_c$, where τ is the true tortuosity of the fluid flow path, and ϕ_c is the connected porosity.

The noncontact resistivity sensor on the MSCL system operates by inducing a high-frequency magnetic field in the core with a transmitter coil, which in turn induces electrical currents in the core that are inversely proportional to the resistivity. Very small magnetic fields regenerated by the electrical current are measured by a receiver coil. To measure these small magnetic fields accurately, a technique has been developed that compares readings generated from the measuring coils to readings from an identical set of coils operating in air. Electrical resistivity data were obtained at 4 cm intervals along each core section.

Magnetic susceptibility

Magnetic susceptibility is the degree to which a material can be magnetized by an external magnetic field. A Barrington loop sensor (MS2C) with an 8 cm loop diameter was used for magnetic susceptibility measurements. An oscillator circuit in the sensor produces a low-intensity (8.0×10^{-4} mA/m RMS), nonsaturating, alternating magnetic field (0.565 kHz). Any material near the sensor that has a magnetic susceptibility causes a change in the oscillator frequency. This pulse frequency is then converted into a magnetic susceptibility value. The spatial resolution of the loop sensor is ~ 4 cm, and its accuracy is

5%. Magnetic susceptibility data were obtained at 4 cm intervals with an acquisition time of 1 s.

Natural gamma radiation

NGR emissions were recorded from all core sections and all unwashed cuttings samples to determine variations in the radioactive counts of the samples and for correlation with the downhole NGR measurements from logs. Unwashed bulk cuttings were packed into a 15 cm long core tube, producing a volume of 350 cm³. A lead-shielded counter, optically coupled to a photomultiplier tube and connected to a bias base that supplied high-voltage power and a signal preamplifier, was used. Two horizontal and two vertical sensors were mounted in a lead cube-shaped housing. Most NGR emissions from rocks and sediment are produced by the decay of ⁴⁰K, ²³²Th, and ²³⁸U, which are three long-period isotopes. Spatial resolution for this measurement was ~160 mm, and NGR was measured every 16 cm for 30 s. Background radiation noise was 35 cps, measured using a blank filled with distilled water, and this value was subtracted from the raw data to obtain NGR data for the samples.

Moisture and density (cores and cuttings)

Sampling and handling procedures

Core samples

Approximately 5 cm³ of material was taken from the working half of the core for each MAD measurement, at a spacing of one sample per core section. In addition, MAD samples were routinely taken from “cluster” slices adjacent to interstitial water whole-round samples. If the whole-round sampling location overlapped the regular MAD sampling intervals, no additional MAD sample was taken from the working half. Care was taken to sample undisturbed parts of the core and avoid drilling mud. Hard sediment and rock samples were cut with a parallel saw and soaked for 6 h in a 35‰ NaCl solution.

Cuttings

For cuttings, a volume of ~50 cm³ taken from the 1–4 mm size fraction was used for analysis. In sections of specific interest (1200–1400 m MSF in Hole C0009A), cuttings from the >4 mm size fraction were also used for analysis and comparison with the 1–4 mm fraction to assess the effects of sample fraction size on MAD measurements. Cuttings were rinsed three times with a 35‰ NaCl solution and then soaked for 6 h in a 35‰ NaCl solution. Cuttings were separated from the solution using a funnel and then were wiped dry and placed into a glass cell.

Moisture and density measurements

The wet sample mass (M_{wet}) was measured, and dry mass (M_{dry}) and volume (v_{dry}) were measured after drying the samples in a convection oven for >24 h at 105° ± 5°C. Dried samples were then cooled in a desiccator for at least 1 h before the dry mass was measured. Wet and dry masses were determined using a paired electronic balance system, which is designed to compensate for the ship’s heave. Dry volume was measured using a helium-displacement Quanta-chrome penta-pycnometer with a nominal precision of ±0.04 cm³. Each reported value consists of an average of five measurements.

For calculation of bulk density, dry density, grain density, porosity, and void ratio, IODP Method C (Blum, 1997) was used. Water content, porosity, and void ratio are defined by the mass or volume of extracted water before and after removal of all water present in the sample through the drying process. This includes interstitial water (inside the pores) and water bound in hydrous minerals. Standard seawater density ($\rho_w = 1.024 \text{ g/cm}^3$) was assumed for the density of pore water.

Water mass, salt mass, water volume, and water content

Pore water mass (M_w), salt mass (M_s), pore water volume (v_{pw}) and salt volume (v_s) can be calculated by

$$M_w = (M_t - M_d)/(1 - s), \quad (16)$$

$$M_s = M_w - (M_t - M_d)s = (M_t - M_d)s/(1 - s), \quad (17)$$

$$v_{\text{pw}} = M_w/\rho_w = (M_t - M_d)/[(1 - s)\rho_w], \text{ and} \quad (18)$$

$$v_s = M_s/\rho_{\text{salt}} = [(M_t - M_d)s/(1 - s)]/\rho_{\text{salt}}, \quad (19)$$

where

M_t = total mass of the saturated sample,

M_d = mass of the dried sample,

s = salinity (35‰),

ρ_w = density of pore fluid, and

ρ_{salt} = density of salt (2.22 g/cm³).

Water content (W_c) was determined following the methods of the American Society for Testing and Materials (ASTM) designation D2216 (ASTM International, 1990). Corrections are required for salt when measuring the water content of marine samples. In addition to the recommended water content calculation in ASTM D2216 (i.e., the ratio of pore fluid mass to dry sediment mass [percent dry weight]), we also calculated the ratio of pore fluid mass to total sample mass (percent wet weight). The equations for water content are

$$W_c (\% \text{ dry wt}) = (M_t - M_d)/(M_d - sM_t), \text{ and} \quad (20)$$

$$W_c (\% \text{ wet wt}) = (M_t - M_d) \times (1 - s)/M_t. \quad (21)$$

Bulk density

Bulk density (ρ_b) is the density of the saturated samples defined as $\rho_b = M_t/v_t$, where total wet mass (M_t) was measured using the balance, and total volume (v_t) was determined from the pycnometer measurements of dry volume (v_d) and the calculated volumes of the pore fluid and salt ($v_t = v_{pw} + v_d - v_s$).

Porosity

Porosity (ϕ) was calculated by

$$\phi = v_{pw}/v_t. \quad (22)$$

Grain density

Grain density (ρ_g) was determined from measurements of dry mass and dry volume. Mass and volume were corrected for salt by

$$\rho_g = (M_t - M_w - M_s)/(v_d - v_s). \quad (23)$$

Thermal conductivity (cores)

Thermal conductivity measurements were conducted on split cores at a frequency of 1 per core using a half-space line source probe (HLQ probe) and high-precision thermal conductivity meter (TeKa TK04 unit). At the beginning of each measurement, a ~10 cm long split core piece was taken from the working half and placed in seawater at ambient temperature (20°C) for 15 min. The sample and probe were then wrapped in stretchable plastic wrap to maintain contact between the probe and sample face. Care was taken to remove any visible air bubbles and extra water between the plastic wrap and the sample surface. The HLQ probe was placed on a flat surface of the sample with the line probe oriented parallel to the core axis, and heating and measurements were conducted automatically. During each 24 h period, a standard block with thermal conductivity of $1.652 \pm 2 \text{ W/(m}\cdot\text{K)}$ was measured. The requirement for data quality control was that the measured conductivity of the standard sample was in the range of 1.62–1.68 W/(m·K).

MSCL-I: photo image logger (cores)

The MSCL-I scans the surface of archive-half cores and creates a digital image. The line-scan camera is equipped with three charge-coupled devices; each charge-coupled device has 2048 arrays. Light reflected from the sample surface passes through the

lens and is split into three paths (red, green, and blue) by a beam splitter inside the line-scan camera. Then, each reflection is detected by the corresponding charge-coupled device. Finally, the signals are combined and the digital image is produced. Optical distortion downcore is avoided by precise movement of the camera. Spatial resolution is 100 pixels/cm.

Discrete *P*-wave measurement for *P*-wave velocity and anisotropy (cores)

P-wave velocity was measured on discrete samples taken from cores at the same locations as MAD samples, at a sample spacing of 1 per core section. Core pieces were cut with a rock saw into ~20 mm cubes. This sample preparation enables measurement of *P*-wave velocity in three orthogonal directions. All cubes were cut with faces orthogonal to the *x*-, *y*-, and *z*-axes of the core reference, respectively, and were soaked in a NaCl 35‰ solution for 6 h. Orientation of the axes is defined as *z*- pointing downward along the core axis, *x*- pointing into the working half, and *y*- along the core face.

A newly installed *P*-wave logger for discrete samples (PWL-D) was used (Geotek LTD London, UK). Its basic measurement principle is to measure *P*-wave traveltime and sample length, respectively, and then to calculate *P*-wave velocity. To measure *P*-wave velocity in a given direction, the sample is held by two 1.5 kg weights with a force of ~30 N (corresponding to a pressure of 75 kPa) between two transducers covered with rubber spacers to ensure good contact between the sample and the transducers. Both transmitter and receiver are a type of piezocomposite transducer, and the frequency of the compressional wave (*P*-wave) generated by the transmitter is 230 kHz. The transmitter is connected to a pulse generator, the receiver is connected to an amplifier, and the received signal is processed through an analog-to-digital (A/D) converter and then displayed on a PC. Traveltime is picked and logged automatically based on a threshold set by the operator. The sample dimension for the *P*-wave path is automatically measured at the same time as the traveltime measurement by a distance laser sensor mounted in the apparatus.

Calibration of traveltime and laser distance sensor correction was conducted daily. The traveltime offset was determined by placing the transmitter and receiver in direct contact and measuring traveltime. This setup provides a time offset of ~9.8 μs, which is subtracted from the total traveltime to obtain the true traveltime through the sample. Velocity along a given direction is simply given by sample dimension divided by traveltime. Laser distance calibration was

conducted by placing the transmitter and receiver in direct contact and then separating them using a reference box 2.5 cm high.

We defined two parameters to evaluate the degree of anisotropy in the three orthogonal directions:

$$\alpha_1 = 2[(V_{Px} - V_{Py})/(V_{Px} + V_{Py})], \text{ and} \quad (24)$$

$$\alpha_T = 2[(V_{Px} + V_{Py})/2 - V_{Pz}]/[(V_{Px} + V_{Py})/2 + V_{Pz}], \quad (25)$$

where

α_1 = apparent anisotropy in the horizontal plane,

α_T = apparent transverse anisotropy,

V_{Px} = x -direction P -wave velocity,

V_{Py} = y -direction P -wave velocity, and

V_{Pz} = z -direction P -wave velocity.

Magnetic susceptibility (cuttings)

Approximately 10 cm³ of cuttings material (taken from material previously used for MAD measurements) was used for measuring magnetic susceptibility by Kappabridge, of which 7 cm³ was placed in a pmag cube for testing. The Kappabridge has a sensitive sensor so it can measure samples with a magnetic susceptibility as low as 3×10^{-8} m³/kg. Cubes were weighed empty and then filled with the washed cuttings material. A standard was measured daily to ensure proper calibration of equipment, and a blank empty cube was measured with each batch of samples to obtain a background measurement. Samples were then measured using standard test procedures for the Kappabridge (Blum, 1997).

Logging

Wireline logging provides information on a wide range of in situ physical properties at scales of tens of centimeters to tens of meters, including compressional, shear, and surface wave velocities; electrical resistivity; NGR intensity; bulk density; and porosity. This section describes methods for obtaining (1) porosity from density and resistivity logs, (2) thermal conductivities from density logs, (3) downhole temperature profile based on thermal conductivity estimations, and (4) gas saturation from compressional and shear velocity logs.

Estimation of porosity from the density log

Porosity is calculated from bulk density log data by assuming a constant grain density (ρ_g) of 2.65 g/cm³ and a constant water density (ρ_w) of 1.024 g/cm³ using equation 3 in Blum (1997).

Estimation of thermal conductivity and temperature profile

The depth-dependent thermal conductivity (K) is estimated from porosity using a geometric mean model:

$$K = K_g^{1-\phi} K_w^\phi, \quad (26)$$

where

K_g = grain thermal conductivity (2.85 W/[m·K] from Ocean Drilling Program Leg 190 Site 1173; Moore, Taira, Klaus, et al., 2001), and

K_w = water thermal conductivity (0.60 W/[m·K]).

A 2°C surface (seafloor) temperature is assumed in the calculation. The temperature gradient is integrated from the seafloor downward using the estimated thermal conductivity profile and a measured or assumed heat flow at each site.

Estimation of porosity from resistivity

Archie's law is used to estimate porosity from resistivity:

$$F = a/\phi^m, \quad (27)$$

where

F = formation factor,

a = a constant, and

m = "cementation factor."

The value of m depends on rock type and is more closely related to texture than to cementation. The definition of a and m for each site is described in the site chapters.

The formation factor is calculated as

$$F_a = R_e/R_f, \quad (28)$$

where

R_e = bulk resistivity of the formation, and

R_f = fluid resistivity.

We assumed that the pore fluid is similar to seawater. The formula used to calculate the resistivity of seawater (R_f) as a function of temperature (T) (°C) is (Shipley, Ogawa, Blum, et al., 1995)

$$R_f = 1/(2.8 + 0.1T). \quad (29)$$

Estimation of gas saturation from the compressional velocity log

Brie et al. (1995) developed a model for the dependence of sonic velocities on pores and their fluid content that can be applied to clay-rich formations.

It is based on the Gassmann equation for porous media and connects the bulk modulus of the fluid-filled material (K) to the modulus of the dry porous medium (K_{dry}), the modulus of the material (K_s), and the modulus of the fluid (K_f):

$$K = K_{\text{dry}} + \frac{\left(1 - \frac{K_{\text{dry}}}{K_s}\right)^2}{\frac{\phi}{K_f} + \frac{1 - \phi}{K_s} - \frac{K_{\text{dry}}}{K_s^2}}. \quad (30)$$

Elastic moduli are obtained from compressional wave velocity (V_p) and shear wave velocity (V_s), both of which are obtained from the sonic log:

$$(V_p/V_s)^2 = K/G + 4/3, \quad (31)$$

where G is the shear modulus of the material. The ratio K/G is assumed to be the same for a nonporous material and for a porous material filled by very compressible fluid (Brie et al., 1995):

$$K_s/G_s = K_{\text{dry}}/G_{\text{dry}}. \quad (32)$$

Under this assumption, an empirical relationship can be developed to estimate G for clays:

$$G_{\text{dry}} = G_s(1 - \phi)^8. \quad (33)$$

Using the known velocities for the matrix, the shear modulus (G_s), and hence the shear modulus of the dry porous material (G_{dry}) can be computed from Equation 33. By combining Equations 31 and 32, V_p/V_s can be plotted versus slowness ($1/V_p$) for a given porosity (in the case of a fully water-saturated fluid). In case of partial saturation (water saturation [S_w] < 100%, as would be the case if gas is present), fluid moduli are computed by

$$1/K_f = S_w/K_w + (1 - S_w)/K_g, \quad (34)$$

where

$$\begin{aligned} K_g &= \text{gas modulus, and} \\ K_w &= \text{water modulus.} \end{aligned}$$

For an ideal gas, the modulus is equal to its pressure and is assumed to be hydrostatic. The gas saturation can then be determined by fitting computed values of $1/V_p$ and V_p/V_s , which depend on ϕ and S_w , to V_p and V_s measurements from wireline logging.

Poisson's ratio (ν) is related to the ratio of V_p and V_s by

$$\nu = 1/2\{[(V_p/V_s)^2 - 2]/[(V_p/V_s)^2 - 1]\}. \quad (35)$$

Downhole measurements

Modular Formation Dynamics Tester

The MDT wireline logging tool was used to measure in situ stress, permeability, and pore fluid pressure. Its modular design allowed it to be customized for several applications. The configuration we used during Expedition 319 included the gamma ray sonde, pumpout module (MRPO), single probe module (MRPS), and dual packer module (MRPA) (Figs. F15, F16). We used the MDT tool to conduct three types of tests: (1) single probe drawdown tests to measure pore fluid pressure (P_f), fluid mobility, and permeability (k); (2) dual packer drawdown tests to measure P_f and k ; and (3) dual packer hydraulic fracture tests to estimate the least principal stress (σ_3).

Single probe tests

Single probe pore pressure measurements are made by pushing a probe against the sidewall and withdrawing pore fluid (Figs. F15, F17). Pressure in the isolated zone is recorded during and after pore fluid extraction with a sampling period of 300 ms. For single probe measurements during Expedition 319, a fluid volume of 5–10 cm³ was extracted at a rate of 30–80 cm³/min. The extracted volume is usually chosen based on anticipated formation permeability, and it is commonly adjusted during multiple drawdown tests at a single measurement location. Three probe types are available for single probe measurements: (1) conventional, (2) large-diameter probe, and (3) large-diameter packer. For all Expedition 319 deployments, the large-diameter probe was used.

We estimated in situ pore fluid pressure from the last pressure recorded during the pore pressure recovery in single probe tests. More sophisticated approaches that extrapolate from the recovery curve of pore pressure to in situ pressure were deferred to post-expedition research. During Expedition 319, we used Schlumberger's standard approach to estimate fluid mobility for single probe measurements. Pore pressure was drawn down for a specified time (typically 15 s), and then the pressure was allowed to partially or fully recover. The mobility is calculated by

$$k_D/\mu = Cq/\Delta P. \quad (36)$$

Equation 36 is dimensionally dependent. k_D is the drawdown permeability (md), μ is viscosity (centipoise), q is the flow rate (volume of fluid extracted during the drawdown divided by the time [cm³/s]), and ΔP (psi) is the difference between drawdown pressure and in situ pressure (often approximated as the final build-up pressure). C is a constant that de-

depends on the probe type (C = 5360, 2395, and 1107 for conventional, large-diameter probe, and large-diameter packer, respectively); C = 2395 for all Expedition 319 deployments.

Dual packer tests

The dual packer module on the MDT tool was configured to isolate a 1 m section of the borehole (Fig. F18). Pressures in the packers and test interval were recorded simultaneously and could be displayed in real time. As with the single probe tests, the data sampling interval was 300 ms. The MRPO is used to pump fluid from the mud column to the packers or into the test interval. The MRPO can either withdraw or inject fluid into the test interval. The flow rate depends on the differential pressure (the difference between the mud pressure and the flowing pressure). At a differential pressure greater than several thousand pounds per square inch (several MPa), flow rates are as low as 0.1 cm³/s, whereas at differential pressures of a few hundred pounds per square inch (MPa), flow rates are as high as 31.6 cm³/s. The maximum differential pressure is 3500 psi (24 MPa) for the displacement pump. The packers have a 10 inch diameter prior to inflation and are designed for 12¼ to 14¾ inch boreholes.

The packers seal most effectively if they are deployed in a zone of the borehole that is not washed out and where there are no preexisting fractures. During Expedition 319, logging data and core information were used to find optimal zones for deploying the dual packer tool. Our minimum criteria for choosing a location were a 5 m thick zone <14¾ inches in diameter with hole ovality (max diameter/min diameter) of <130%. The test section was sealed off by inflation of the dual packers. After sealing off the test interval, either a drawdown test or a hydraulic fracturing test was performed.

Dual packer pressure drawdown test

During a drawdown test, fluid is rapidly extracted from the isolated section causing a drop in pressure within the interval. The pump is then stopped and the pressure begins to recover as fluid flows from the formation into the sealed borehole interval. The time necessary for pressure stabilization is longer for formations with low permeability. Permeability and the coefficient of consolidation can be estimated from comparison with theoretically derived curves (e.g., Papadopoulos et al., 1973). As for the single probe tests, formation pore fluid pressure was estimated as the pressure at the end of the pressure recovery phase.

Dual packer hydraulic fracture test

The hydraulic fracturing, or “minifrac,” test is carried out following a standard procedure (Haimson and Cornet, 2003). Fluid is pumped into the isolated interval under a constant flow rate (Fig. F18). This gradually raises the pressure within the interval until a fracture is initiated within the formation. Pumping is stopped (“shut in”) some time after fracture initiation, and the pressure decays. Several minutes after shut in, pressure is released and allowed to return to ambient conditions. The pressure cycle is repeated several times, maintaining the same flow rate. Key pressure values used in the computation of in situ stress are picked from this pressure-time record. Among these, the most useful is the instantaneous shut in pressure (ISIP), which is thought to be close to the least principal stress (σ_3). ISIP is determined from the first break in slope in a plot of pressure versus time after the shut in (Zoback, 2007). If repeated cycles provide consistent values of the key pressures (e.g., the ISIP), this confirms that the fracture has grown sufficiently and the least principal stress is being measured.

The hydraulic fracture data can be integrated with other information to obtain further constraints on the in situ stress state. For example, if an image log is run after the hydraulic fracturing test, the orientation of the induced fracture (and therefore of σ_3) can be defined. Borehole breakout information can be used to define the orientation of the maximum and minimum horizontal compressive stresses (see “Structural geology”).

Vertical seismic profile in scientific drilling

The VSP is a high-resolution seismic imaging technique often employed in industry. In past scientific ocean drilling, zero-offset VSP (check shot) experiments were conducted to improve depth resolution and seismic velocity near the borehole (Holbrook et al., 1996). A VSP involves geophones lowered from the drillship into the drill hole to receive signals from a sea-surface source. The zero-offset VSP, which receives signals from a source next to the drillship, provides traveltimes more precisely than seismic survey data and improves the accuracy of the location of strata and faults. The VSP technique can be expanded with a line of shots fired at increasing distances from the drill hole by a surface ship (walk-away VSP) to acquire 2-D seismic reflection images and refraction data.

There have been several previous VSP experiments in IODP designed to record seismic waves generated from an air gun towed by a shooting vessel. One ex-

ample is an experiment using a broadband seismometer lowered to 714.5 mbsf by wireline in a borehole in the Japan Sea during ODP Leg 128 (Kanazawa et al., 1992; Shinohara et al., 1992). Later experiments used broadband seismometers cemented permanently at the bottom of boreholes in the northwestern Pacific Ocean and the Philippine Sea (Salisbury et al., 2006; Shinohara et al., 2008). These seismometers were all intended as part of a permanent or long-term borehole observatory.

For a VSP experiment, the seismic source signal is commonly recorded at an array of receivers placed in the drill hole. A walkaway VSP produces higher quality data than data obtained from a surface ship using hydrophones at the sea surface because the VSP array employs three-axis geophones that are clamped to the walls of the borehole. These clamps couple the receivers firmly to the formation, and the receiver can resolve the ground motion caused by the seismic source with high fidelity. With three-axis data, the direction from which reflected waves arrive is also determined. Seismic signals with higher frequencies are acquired because the seismic signal travels through the water and the seafloor interface only once, whereas sea-surface source and receiver systems record signals that have passed through the water and seafloor twice. The seafloor interface degrades signals and attenuates the higher frequencies that provide better spatial resolution. In addition, the shortened ray path reduces the Fresnel zone. The much better signal-to-noise ratio achieved in a quiet borehole environment enhances recording of low-amplitude signals.

Seismic anisotropy from VSP experiment

During the walkaway VSP experiment during Leg 128, circle shooting was conducted for analysis of seismic anisotropy of the Yamato Basin crust (Hirata et al., 1992). In this experiment, two circular lines (radius of 9 and 18 km) were shot to define the seismic anisotropy of refracted waves in the lower crust. Seismic anisotropy can also be studied from linear seismic lines of different azimuths crossing at the borehole (Shinohara et al., 2008). During the walkaway VSP experiment in Expedition 319, a circle with a 3.5 km radius was shot around Site C0009 (Fig. F19) to document seismic anisotropy in the Kumano Basin sediment.

Walkaway vertical seismic profile

A walkaway VSP experiment was conducted in Hole C0009A after installation and cementing of the 13 $\frac{3}{8}$ inch casing to ~1600 m DRF, with a seismometer array (VSI tool, Schlumberger, 2002) deployed near the bottom of the hole to observe air gun shots from a

separate shooting vessel (Fig. F20). The VSI tool consists of an array of separate sensor shuttles, a VSI cartridge, and a telemetry module. Each sensor shuttle consists of triaxial (three component) geophone accelerometers, a shaker, and a locking arm to provide mechanical coupling to the casing interior (Table T11). The shooting vessel (JAMSTEC R/V *Kairei*) shot a single 53.4 km long offset transect in the dip direction of the subducting plate and a 3.5 km radius circular shooting offset around the borehole (Fig. F19). Opening the hole to 17 inches, installing the 13 $\frac{3}{8}$ inch casing, and cementing the casing were completed before the walkaway VSP experiment.

The objective of the walkaway VSP experiment was to improve our understanding of the structure around the megasplay fault and the master décollement including

- Spatial variation of *S*-wave velocity,
- Attenuation of *P*- and *S*-waves,
- Anisotropy of *P*- and *S*-waves, and
- Contrasts in physical properties across the faults.

Better coupling of the VSI seismometer with the formation improves the quality of the *S*-wave data from a wide-offset range to provide reliable shear wave velocity estimates. Direct comparison of seismic data obtained from the ocean bottom and the downhole environment are valuable for attenuation parameter estimation. Azimuthal dependence of arrival times and amplitudes of seismic waves provide estimates of the direction and magnitude of anisotropy in compressional (*P*) and shear (*S*) wave velocities, which may be correlated to the stress field around the site. Seismic records obtained from the downhole site are expected to be rich in high-frequency content and thus will enable us to examine the fine structure of the plate boundary fault system. Measurements of reflection coefficients (not only *P* to *P* but also for *S* to *S*, *P* to *S*, and *S* to *P* reflections) will clarify contrasts in elastic moduli and density across reflectors.

Survey design

The design of the walkaway VSP experiment during Expedition 319 was guided by recommendations from an industry contractor (Seismic 2020), whose staff modeled the experiment with proprietary 3-D VSP modeling software. Modeling showed that deployment of the receivers at the bottom of the drill hole (~1600 mbsf) was optimal, but that good results could also be obtained further up the hole. The critical angle for reflections from the plate interface would be reached ~15 km from the hole, and a maximum number of receivers (20) would optimize results.

Location and survey lines

The location of the survey line, ocean-bottom seismometers (OBSs), and broadband ocean-bottom seismometers (BBOBSs) are shown in Figure F19 and Tables T12, T13, and T14.

Data acquisition

The shooting ship *Kairei* shot air guns while traveling along the survey line (Fig. F19). The air guns towed by *Kairei* consisted of four tuned subarrays of air guns (Fig. F21) designed to generate high-amplitude broadband acoustic waves. A total of 16 VSI shuttles with 15.12 m intervals were lowered as deep as possible into the casing and individually clamped in the casing with mechanical arms. The acquisition parameters are shown in Tables T15, T11, and T16. The triaxial geophones in the VSI tool (Table T11) recorded direct, reflected, refracted, and converted seismic waves.

Prior to air gun shooting, the *Kairei* deployed eight OBSs and communicated acoustically to three BBOBSs deployed in a previous survey. The *Chikyu* and the *Kairei* conducted a radio communication test at maximum range of 50.7 km to confirm shot and recording synchronization before air gun shooting began. For Line 1, the *Kairei* shot every 60 m from southeast to northwest starting 24.1 km southeast of the *Chikyu* (B in Fig. F19). In the vicinity of the *Chikyu*, the *Kairei* turned at a point 500 m from Hole C0009A and maintained a distance of 350 m from the *Chikyu* to avoid collision before returning to the shooting course. After passing the *Chikyu*, the *Kairei* switched shooting from Line 1 to Circle 1, with an offset of 3.5 km from the *Chikyu* (Fig. F19). In circle shooting, the *Kairei* shot every 30 s while cruising clockwise. After completing circle shooting, the *Kairei* resumed shooting Line 1 to 29.3 km northwest of the *Chikyu* (A in Fig. F19).

Accurate synchronization between shooting and receiving timing is the most important factor in successful walkaway VSP data acquisition. A very high frequency radio signal from the blaster controller on the *Kairei* was used to start data recording aboard the *Chikyu*. A predetermined constant time interval for shooting was prepared in case of radio communication breakdown over long distances or in bad radio communication conditions. Accurate time from the Global Positioning System (GPS) was recorded for all shots for both the shooting and recording systems. Another system, Schlumberger's VSI recording system (MAXIS), which records GPS time with an accuracy of 1 s, was used in conjunction with time synchronization and the accurate time recording system as shown in Table T17.

Acquisition parameters

Seismic source parameters are given in Table T15, and recording parameters are given in Table T18. Navigation and positioning parameters are given in Table T16. Specifications for time synchronization and time recording are given in Table T17.

Onboard data flow, quality check, and processing

The data were stored in MAXIS (Schlumberger's VSI acquisition system) and an initial quality control check was conducted on the ship. The data were converted to SEG-Y (Society of Exploration Geophysicists standard Y) format and delivered to the scientists. Further processing will be completed postexpedition.

Zero-offset VSP

A zero-offset VSP (check shot) was conducted after the walkaway VSP experiment using the same VSI tools (Table T11). In this configuration, the VSI tools in the borehole receive seismic energy from a conventional air gun suspended from a crane on the drillship.

The main objectives of the zero-offset VSP are to

- Obtain a depth-time-velocity profile (check shot),
- Conduct sonic calibration,
- Document seismic reflectivity along/below the borehole (corridor stack), and
- Serve as a reference for the walkaway VSP in the vicinity of the borehole.

Tool and system

Schlumberger's VSI receiver tools and MAXIS surface seismic recording system were used as in the walkaway VSP experiment. The three-component geophone accelerometers detect vertical and horizontal particle motions and provide a linear and flat response from 3 to 200 Hz. The receivers consisted of eight shuttle-array VSI systems spaced at 15.12 m. The receivers record acoustic waves fired by air guns shot from 6 mbsl and ~60 m away from the borehole with a chamber pressure of 1700–2000 psi (Fig. F22). We used three sets of 250 in³ air guns as a seismic source (Fig. F23). Time correlations of the shots are ensured with a surface hydrophone suspended 5 m below the air guns (11 m below mean sea level).

Data acquisition

The VSI receivers were checked by air gun shooting from the *Chikyu* before the zero-offset VSP survey, and the waveforms of VSI Shuttles 9 and 10 indi-

cated that coupling to the formation was poor. The positions of the VSI shuttles were changed and rechecked, but their coupling did not improve. Consequently, we decided to use only eight shuttles for zero-offset VSP. The VSIs were clamped to the casing and the air gun was fired between 6 and 11 times at each station to improve the signal-to-noise ratio by stacking. After stacking, the arm crutches (clamps) were released and the VSIs were raised by ~121 m (8 shuttle intervals) and then clamped again and shots fired. These procedures were repeated until reaching 2227.4 m WRF. During acquisition, the seismic signals were recorded in MAXIS. The acquisition parameters are shown in Table T19.

Onboard data flow and quality check

The VSI raw seismic data, depth-time/-velocity tables (check shot results), and quick report were delivered by Schlumberger engineers and distributed to the Shipboard Science Party for immediate processing and analysis. The waveforms were converted to SEG Y format.

Cuttings-Core-Log-Seismic integration

During Expedition 319 we used information from cores and cuttings as well as several of the LWD, MWD, and wireline logging data sets to establish accurate ties to the 2006 Kumano 3-D seismic reflection data set (e.g., Moore et al., 2007, 2009). In addition, zero-offset VSP (check shot) results (see “[Downhole measurements](#)”) were used to verify or adjust depths of the 3-D seismic reflection volume (see below).

At Site C0009, wireline logging data, gamma ray data from MWD, cuttings from riser drilling, and a limited number of cores were available to define lithologic units. Three wireline logging runs were conducted: the first run with EMS-HRLA-PEX-gamma ray, the second run with FMI-Hostile Natural Gamma Ray Spectrometry Cartridge (HNGC)-Sonic Scanner-EMS-Power Positioning Device and Caliper Tool (PPC), and the third run with MDT-gamma ray (see “[Logging](#)” and this section for details). At Sites C0010 and C0011, only a limited suite of LWD/MWD data was available. The suite comprises data from the LWD geoVISION tool, measuring NGR and resistivity, and the MWD-PowerPulse, measuring direction and inclination, downhole torque, and WOB. For details regarding techniques, refer to “[Logging](#),” “[Lithology](#),” “[Downhole measurements](#),” and “[Physical properties](#).”

Seismic reflection data

Data acquisition along the NanTroSEIZE transect was contracted with Petroleum Geo-Services (PGS) in 2006, covering an area ~12 km × 56 km that extends from the Kumano Basin seaward to the frontal thrust in the dip direction and extends from ~4 km northeast to ~8 km southwest along strike of the NanTroSEIZE drilling transect (Moore et al., 2009).

Preexpedition 3-D seismic processing consisted of three stages. In the first stage, PGS provided a 3-D stack and poststack migration to better understand the regional seismic reflection characteristics for choosing parameters for more detailed processing. During the second stage, the data set was processed through 3-D prestack time migration by Compagnie Générale de Géophysique (CGG) in Kuala Lumpur, Malaysia. Variable streamer feathering and strong seafloor multiples required several processing steps to fill and regularize all of the bins and provide quality imaging. The third stage consisted of 3-D prestack depth migration (PSDM) performed at the JAMSTEC-Institute for Research on Earth Evolution (IFREE). The 3-D PSDM clearly images details of faults and small-scale structures but lacks velocity resolution deeper than ~4500–5000 mbsf. Data resolution is ~5–7 m for near-surface sediments, ~10–20 m for the deepest sediments drilled so far in NanTroSEIZE, and ~90–125 m for the oceanic crust region.

In order to acquire as accurate a cuttings-core-log-seismic correlation as possible, the depth-migrated data were converted back to time using the PSDM velocity field and then reconverted to depth using new velocity information based on the zero-offset VSP (check shot) (see “[Downhole measurements](#)” and “[Downhole measurements](#)” in the “[Site C0009](#)” chapter). In this way we minimized the potential differences in arrival times between these seismograms and those in the Kumano 3-D multichannel seismic data.

Application to information from coring and logging

Zero-offset VSP measurements did not cover the entire drilled and cored interval (see the “[Site C0009](#)” chapter). Hence, it was necessary to extrapolate the velocity structure below the lowest check shot data point based on velocity-depth profiles obtained from wireline sonic data (see “[Downhole measurements](#)”). Velocities from the sonic log were lower than those used for seismic processing prior to the expedition (see above and discussion in “[Cuttings-Core-Log-Seismic integration](#)” in the “[Site C0009](#)” chapter). For Site C0010, zero-offset VSP data were

not available, so the regional velocity model used both the PSDM velocity field (see Moore et al., 2009, and above) and the zero-offset VSP information from Site C0004, located ~3.5 km to the east of Site C0010 (Kinoshita, Tobin, Ashi, Kimura, Lallemand, Sreaton, Curewitz, Masago, Moe, and the Expedition 314/315/316 Scientists, 2009). Details regarding measures taken at the individual sites are found in the respective site chapters.

Once the seismic data were refined using the relevant zero-offset VSP and sonic log data, intervals where complementary information from LWD, downhole logging, or coring was available were examined. For Expedition 319, this meant, explicitly,

- Relating prominent seismic reflectors and contrasts in impedance to characteristic lithologic changes, unit boundaries, unconformities, or layers with special physical properties;
- Correlating zones of low *P*-wave velocity in the seismic data with mud gas occurrence (riser hole) or variations in resistivity and other parameters during LWD and wireline logging runs;
- Linking prominent fault zone reflectors (where present) to areas of broken formation in core, high conductivity in image logs, high density/low porosity in cores and cuttings, and/or age reversals or age gaps defined by biostratigraphy;
- Correlating the clay fraction (from core and cuttings based on XRD and VCD) with any excursions in gamma ray, photoelectric effect, and SP logs; and
- Relating onlapping or downlapping reflectors to discontinuities in the biostratigraphic succession (age reversals, hiatuses).

Observatory

Sensor dummy run test

After casing operations at Site C0010 (proposed Site NT2-01J), we conducted a simulation of the planned future borehole sensor installation as part of the preparation for installation and fabrication of long-term borehole observatories in future NanTroSEIZE expeditions. This test had two main objectives: (1) to evaluate environmental conditions, such as shock, acceleration, and vibration during installation and (2) to confirm sensor installation operational procedures, such as shipboard assembly of the sensor tree, ship maneuvers to reenter the hole, and hole reentry. In addition, nine miniature temperature loggers (MTLs) were attached to the dummy instrument package to provide temperature data.

The sensor tree is illustrated in Figure F24. The tree was attached to the end of the drill pipe before running into the hole. The tree consists, from the bottom up, of one 6 ft pup joint, two 3½ inch tubing joints, a borehole strainmeter (Fig. F25), a multiinstrument carrier housing a self-recording accelerometer-tiltmeter (Fig. F26), two broadband borehole seismometers (Guralp CMG1T and CMG3T), and four joints of 3½ inch tubing to connect the tree to the drill pipe (Fig. F24). Specifications of the sensors and instrument carrier are summarized in Table T20. The orientation of the sensors is shown in Figure F27. The tree was similar to the structure of the bottom section of planned future observatories (Fig. F28), with the exception that no cables or hydraulic lines were attached, a shorter total length of tubing was used, and there was no packer seal above the tree for hydraulic isolation.

A self-recording accelerometer-tiltmeter equipped with internal lithium batteries was included with the sensors to record vibration and shock data throughout the experiment. The accelerometer measures acceleration in three orthogonal directions (*x*, *y*, and *z*). The orientation of the *x*- and *y*-axes are shown in Figure F27, and the *z*-axis is vertical. The tiltmeter senses two components (*x* and *y*) of tilt; their orientations are the same as for the accelerometer (Fig. F27).

The strainmeter is composed of nine sensors. It runs on internal batteries and records strain changes of the instrument during the experiment, with a positive value indicating compressional strain. The directions for each sensor are shown in Figure F27. The strainmeter has a very weak deformable surface to make contact with the formation and record strain changes without interfering with the surrounding strain field. In order to withstand high pressures in the borehole during installation, the strainmeter is designed to balance its internal pressure with the hydraulic pressure outside of the instrument. In pressure cycling tests, deformation of the strainmeter sensing surface was confirmed to be well within the full scale of the instrument (~2 mm) even under hydrostatic pressure changes up to 60 MPa.

The two borehole seismometers were not set to record any data during testing but were included to test the ability of the internal sensor mechanics to withstand vibration. Performance of the broadband seismometers is highly dependent on the integrity of fragile pivots that suspend the moving mass. Before the experiment, performance of each broadband seismometer was verified by 2 weeks of continuous observation in the Matsushiro vault of the Japan Me-

teorological Agency. The plan for the dummy run originally included onshore inspections of the strainmeter and seismometer packages after the expedition to evaluate any performance changes.

One MTL was set inside a pup joint at the bottom part of the sensor tree, and eight MTLs were attached to the instrument carrier in the first dummy run (Fig. F24; Table T21). Two sets of configurations for sampling interval and observation period were adopted (1) to observe temperature over the entire period of the dummy run experiment and (2) to observe temperature at as high a sampling rate as possible (Table T21).

Temporary monitoring system

As part of operations at Site C0010, the mechanically set retrievable packer (Baker-Hughes A3 Lok-Set) to be installed inside the 9% inch casing string was modified to attach a small instrument package to monitor pore pressure and temperature within the shallow megasplay fault zone (Fig. F29). The instrument package includes one “upward looking” and one “downward looking” pressure sensor to monitor pressure both below the packer seal in a screened interval that is open to the fault zone and above the packer seal to serve as a hydrostatic reference open to the overlying water column. The temperature sensor is located within the instrument package itself and thus records temperature at a depth just below the packer (Fig. F30). The retrievable packer was set inside casing above two screened casing joints that span the splay fault (Fig. F29). The instrument package is threaded to the bottom of the bridge plug and includes a self-contained temperature sensor and data logger, as well as a pressure gauge and data logger package. These instruments will monitor formation pore pressure and temperature from the time the bridge plug is set until they are retrieved at the beginning of permanent riserless observatory installation operations.

General description

The smart plug instruments built for Expedition 319 are designed for deployment immediately beneath a casing packer seal. Structurally, each unit includes a hollow-bore 3.5 inch EU 8RD box end-threaded coupling at the upper end, which mates with the lower end of the Baker-Hughes packer supplied by CDEX, and an outer O-ring-sealed structural shell that is designed to withstand the loads encountered during hole reentry operations (Figs. F31, F32). Housed inside are a high-precision (~10 ppb of full-scale pres-

sure or ~0.7 Pa) A/D converter and data logger (designed and built by Bennest Enterprises, Ltd., Minerva Technologies, Ltd., and the Pacific Geoscience Centre, Geological Survey of Canada), two pressure sensors (Paroscientific, Inc., USA), and an MTL (Antares, Germany). Four independent temperature readings are made by (1) the MTL, (2) a platinum thermometer mounted on the primary data logger end cap, and (3) each of the two pressure sensors as an internal compensation for the pressure measurements. The inside of the structural shell is exposed to the cased borehole above through the internal open bore of the casing packer seal. One of the pressure sensors is in communication with this volume to provide a hydrostatic reference, and the second sensor is in communication with the sealed screened borehole interval below via hydraulic tubing that passes through the bottom end of the smart plug (Fig. F32). RS-422 communications with the pressure logging package for setting recording parameters and downloading data are conducted via a multisegment Seacon AWQ connector on the logger pressure case. Communications with the MTL are conducted with a special Antares interface. The instrument frame is shock-mounted within the structural shell, and the pressure sensors are mounted with secondary shock pads within the frame (Fig. F32). Structural components are constructed with 4140 alloy steel, and pressure sensor housings and hydraulic tubing are constructed from 316 stainless steel.

Settings

The instruments were set to begin recording data at the time they were shipped from the Pacific Geoscience Centre to the Shingu, Japan, port on 11 April 2009 and were stored at Shingu until they were transported to the *Chikyu* via supply boat on 1 June 2009. Logging intervals for the formation and hydrostatic pressure sensors and the internal platinum thermometer were set to 1 min; at this rate and with other operational parameters as set, battery power (provided by six Tadiran TL-5137 DD primary lithium cells) is the limiting factor for operational lifetime, which is roughly 7 y including a derating factor of 75% applied to full power withdrawal. The instruments are equipped with 512 Mb (low power) flash memory cards, which provide ~40 y of storage at a 1 min sampling rate. The independent MTLs in Instruments 8A and 82 are set to sample temperature at 30 and 60 min intervals, respectively. The main logger clocks were synchronized to Universal Time Coordinated (UTC) on 11 April 2009, and the MTL clocks were set at approximately the same date.

Paleomagnetism

Note: This section was contributed by Hirokuni Oda (Institute of Geology and Geoinformation, National Institute of Advanced Industrial Science and Technology, Central 7, 1-1-1 Higashi, Tsukuba 305-8567, Japan) and Xixi Zhao (Earth and Planetary Sciences Department, University of California Santa Cruz, 1156 High Street, Santa Cruz, CA 95064, USA).

The cryogenic magnetometer was off the ship for repairs during Expedition 319, so paleomagnetic analyses were performed during Expedition 322.

Paleomagnetic and rock magnetic investigations on cores taken during Expedition 319 were carried out on the *Chikyu* at the beginning of IODP Expedition 322. The measurements were primarily designed to determine the characteristic remanence directions for use in magnetostratigraphy and to reorient cores for structural analysis. To accomplish these goals, paleomagnetic measurements were performed on archive halves.

Laboratory instruments

The paleomagnetism laboratory on board the *Chikyu* is a relatively large (7.3 m × 2.8 m × 1.9 m) magnetically shielded room with an internal total magnetic field that is ~1% of Earth's magnetic field. The room is oriented with its long axis transverse to the long axis of the ship and houses a superconducting rock magnetometer (SRM) and other magnetically sensitive instruments. The room is large enough to comfortably handle standard IODP core sections (~150 cm).

Superconducting rock magnetometer

The long-core SRM (2G Enterprises, model 760) unit is ~6 m long with an 8.1 cm diameter access bore. A 1.5 m split core liner can pass through a magnetometer, an alternating-field (AF) demagnetizer, and an anhysteretic remanent magnetizer. The system includes three sets of superconducting pickup coils, two for transverse moment measurement (x - and y -axes) and one for axial moment measurement (z -axis). The noise level of the magnetometer is $<10^{-7}$ A/m for a 10 cm³ volume rock. The magnetometer includes an automated sample handler system (2G804), consisting of aluminum and fiberglass channels designated to support and guide long-core movement. The core itself is positioned in a non-magnetic fiberglass carriage that is pulled through the channels by a pull rope attached to a geared

high-torque stepper motor. A 2G600 sample degaussing system is coupled to the SRM to allow automatic demagnetization of samples up to 100 mT. The system is controlled by an external computer and enables programming of a complete sequence of measurements and degauss cycles without removing the long core from the holder.

The measurements on cores taken during Expedition 319 were made during the beginning of Expedition 322. One of the main reasons for this is that the SRM was sent back to the manufacturer to replace y -axis superconducting quantum interference device (SQUID) during Expedition 319. The SRM was then transported from the manufacturer, set up, refilled with liquid He and cooled down to 4.2 K during the port call of Expedition 322 at Yokkaichi, Japan. However, leakage caused the liquid He to evaporate more quickly than usual. We managed to measure the whole archive halves taken during Expedition 319 up to 20 mT AF demagnetization. After the measurements, liquid He in the dewar of the SRM evaporated completely and the SRM stopped working.

Sampling coordinates

Magnetic axes from the long-core magnetometer are reported relative to the double line marked on the plastic liner of the working half of the split core with $+x$, $+y$, and $+z$ representing north, east, and down-core, respectively (Fig. F33). The “flipping” function of the control software (Long Core version 3.4) enables 180° rotation of the x - and y -axes about the z -axis. By using this flipping function, working and archive halves can be measured in the same coordinate system.

Measurements

Remanent magnetization of archive halves was measured at 5 cm intervals using the shipboard 2G Enterprises (model 760R) long-core cryogenic magnetometer equipped with direct-current superconducting quantum interference devices (DC-SQUIDS) and an in-line automated AF demagnetizer capable of reaching a peak field of 80 mT. The response curve from the sensor coils of the cryogenic magnetometer corresponds to a region ~20 cm wide; therefore, only measurements taken every 20 cm are independent from each other. Measurements at core and section ends, whole-round locations and voids, and within intervals of drilling-related core disturbance were not measured or were removed from the data set during data processing.

References

- Anadrill-Schlumberger, 1993. *Logging While Drilling*: Houston (Schlumberger), SMP-9160.
- Araki, E., Byrne, T., McNeill, L., Saffer, D., Eguchi, N., Takahashi, K., and Toczko, S., 2009. NanTroSEIZE Stage 2: NanTroSEIZE riser/riserless observatory. *IODP Sci. Prosp.*, 319. doi:10.2204/iodp.sp.319.2009
- Archie, G.E., 1947. Electrical resistivity—an aid in core analysis interpretation. *AAPG Bull.*, 31:350–366.
- Ashi, J., Lallemand, S., Masago, H., and the Expedition 315 Scientists, 2008. NanTroSEIZE Stage 1A: NanTroSEIZE megaspall riser pilot. *IODP Prel. Rept.*, 315. doi:10.2204/iodp.pr.315.2008
- ASTM International, 1990. Standard method for laboratory determination of water (moisture) content of soil and rock (Standard D2216–90). In *Annual Book of ASTM Standards for Soil and Rock* (Vol. 04.08): Philadelphia (Am. Soc. Testing and Mater.). [revision of D2216-63, D2216-80]
- Blum, P., 1997. Physical properties handbook: a guide to the shipboard measurement of physical properties of deep-sea cores. *ODP Tech. Note*, 26. doi:10.2973/odp.tn.26.1997
- Brie, A., Pampuri, F., Marsala, A.F., and Meazza, O., 1995. Shear sonic interpretation in gas-bearing sands. *SPE Annu. Tech. Conf.*, 30595-MS. doi:10.2118/30595-MS
- Brothers, R.J., Kemp, A.E.S., and Maltman, A.J., 1996. Mechanical development of vein structures due to the passage of earthquake waves through poorly consolidated sediments. *Tectonophysics*, 260(4):227–244. doi:10.1016/0040-1951(96)00088-1
- Cowan, D.S., 1982. Origin of “vein structure” in slope sediments on the inner slope of the Middle America Trench off Guatemala. In Aubouin, J., von Huene, R., et al., *Init. Repts. DSDP*, 67: Washington, DC (U.S. Govt. Printing Office), 645–650. doi:10.2973/dsdp.proc.67.132.1982
- Erzinger, J., Wiersberg, T., and Zimmer, M., 2006. Real-time mud gas logging and sampling during drilling. *Geofluids*, 6(3):225–233. doi:10.1111/j.1468-8123.2006.00152.x
- Expedition 314 Scientists, 2009. Expedition 314 methods. In Kinoshita, M., Tobin, H., Ashi, J., Kimura, G., Lallemand, S., Screaton, E.J., Curewitz, D., Masago, H., Moe, K.T., and the Expedition 314/315/316 Scientists, *Proc. IODP*, 314/315/316: Washington, DC (Integrated Ocean Drilling Program Management International, Inc.). doi:10.2204/iodp.proc.314315316.112.2009
- Expedition 315 Scientists, 2009. Expedition 315 methods. In Kinoshita, M., Tobin, H., Ashi, J., Kimura, G., Lallemand, S., Screaton, E.J., Curewitz, D., Masago, H., Moe, K.T., and the Expedition 314/315/316 Scientists, *Proc. IODP*, 314/315/316: Washington, DC (Integrated Ocean Drilling Program Management International, Inc.). doi:10.2204/iodp.proc.314315316.122.2009
- Expedition 316 Scientists, 2009. Expedition 316 methods. In Kinoshita, M., Tobin, H., Ashi, J., Kimura, G., Lallemand, S., Screaton, E.J., Curewitz, D., Masago, H., Moe, K.T., and the Expedition 314/315/316 Scientists, *Proc. IODP*, 314/315/316: Washington, DC (Integrated Ocean Drilling Program Management International, Inc.). doi:10.2204/iodp.proc.314315316.132.2009
- Fisher, A.T., and Underwood, M.B., 1995. Calibration of an X-ray diffraction method to determine relative mineral abundances in bulk powders using matrix singular value decomposition: a test from the Barbados accretionary complex. In Shipley, T.H., Ogawa, Y., Blum, P., et al., *Proc. ODP, Init. Repts.*, 156: College Station, TX (Ocean Drilling Program), 29–37. doi:10.2973/odp.proc.ir.156.103.1995
- GE Healthcare, 2006. *LightSpeed Series Learning and Reference Guide-Multi Slice CT*: Waukesha, Wisconsin (GE Healthcare), 936.
- Haimson, B.C., and Cornet, F.H., 2003. ISRM suggested methods for rock stress estimation—Part 3: hydraulic fracturing (HF) and/or hydraulic testing of pre-existing fractures (HTPF). *Int. J. Rock Mech. Min. Sci.*, 40(7–8):1011–1020. doi:10.1016/j.ijrmms.2003.08.002
- Hirata, N., Nambu, H., Shinohara, M., and Suyehiro, K., 1992. Seismic evidence of anisotropy in the Yamato Basin crust. In Tamaki, K., Suyehiro, K., Allan, J., McWilliams, M., et al., *Proc. ODP, Sci. Results*, 127/128 (Pt. 2): College Station, TX (Ocean Drilling Program), 1107–1121. doi:10.2973/odp.proc.sr.127128-2.231.1992
- Holbrook, W.S., Hoskins, H., Wood, W.T., Stephen, R.A., Lizzaralde, D., and the Leg 164 Science Party, 1996. Methane hydrate and free gas on the Blake Ridge from vertical seismic profiling. *Science*, 273(5283):1840–1843. doi:10.1126/science.273.5283.1840
- Housen, B.A., 1997. Magnetic anisotropy of Barbados prism sediments. In Shipley, T.H., Ogawa, Y., Blum, P., and Bahr, J.M. (Eds.), *Proc. ODP, Sci. Results*, 156: College Station, TX (Ocean Drilling Program), 97–105. doi:10.2973/odp.proc.sr.156.010.1997
- Kanazawa, T., Suyehiro, K., Hirata, N., and Shinohara, M., 1992. Performance of the ocean broadband downhole seismometer at Site 794. In Tamaki, K., Suyehiro, K., Allan, J., McWilliams, M., et al., *Proc. ODP, Sci. Results*, 127/128 (Pt. 2): College Station, TX (Ocean Drilling Program), 1157–1171. doi:10.2973/odp.proc.sr.127128-2.236.1992
- Kimura, G., Screaton, E.J., Curewitz, D., and the Expedition 316 Scientists, 2008. NanTroSEIZE Stage 1A: NanTroSEIZE shallow megaspall and frontal thrusts. *IODP Prel. Rept.*, 316. doi:10.2204/iodp.pr.316.2008
- Kinoshita, M., Tobin, H., Ashi, J., Kimura, G., Lallemand, S., Screaton, E.J., Curewitz, D., Masago, H., Moe, K.T., and the Expedition 314/315/316 Scientists, 2009. *Proc. IODP*, 314/315/316: Washington, DC (Integrated Ocean Drilling Program Management International, Inc.). doi:10.2204/iodp.proc.314315316.2009
- Kinoshita, M., Tobin, H., Moe, K.T., and the Expedition 314 Scientists, 2008. NanTroSEIZE Stage 1A: NanTroSEIZE LWD transect. *IODP Prel. Rept.*, 314. doi:10.2204/iodp.pr.314.2008
- Lourens, L.J., Hilgen, F.J., Shackleton, N.J., Laskar, J., and Wilson, D., 2004. The Neogene period. In Gradstein, F.M., Ogg, J.G., and Smith, A.G. (Eds.), *A Geological Time Scale 2004*. Cambridge (Cambridge Univ. Press), 409–440.

- Manheim, F.T., 1966. A hydraulic squeezer for obtaining interstitial waters from consolidated and unconsolidated sediments. *Geol. Surv. Prof. Pap. (U.S.)*, 550-C:256–261.
- Martini, E., 1971. Standard Tertiary and Quaternary calcareous nannoplankton zonation. In Farinacci, A. (Ed.), *Proc. 2nd Int. Conf. Planktonic Microfossils Roma*: Rome (Ed. Tecnosci.), 2:739–785.
- Mazzullo, J., and Graham, A.G. (Eds.), 1988. Handbook for shipboard sedimentologists. *ODP Tech. Note*, 8. doi:10.2973/odp.tn.8.1988
- Mazzullo, J.M., Meyer, A., and Kidd, R.B., 1988. New sediment classification scheme for the Ocean Drilling Program. In Mazzullo, J.M., and Graham, A.G. (Eds.), *Handbook for shipboard sedimentologists*. ODP Tech. Note, 8:45–67. doi:10.2973/odp.tn.8.1988
- Mees, F., Swennen, R., Van Geet, M. and Jacobs, P., 2003. Applications of X-ray computed tomography in the geosciences. *Geol. Soc. Spec. Publ.*, 215(1):1–6. doi:10.1144/GSL.SP.2003.215.01.01
- Moore, G.F., Bangs, N.L., Taira, A., Kuramoto, S., Pangborn, E., and Tobin, H.J., 2007. Three-dimensional splay fault geometry and implications for tsunami generation. *Science*, 318(5853):1128–1131. doi:10.1126/science.1147195
- Moore, G.F., Park, J.-O., Bangs, N.L., Gulick, S.P., Tobin, H.J., Nakamura, Y., Sato, S., Tsuji, T., Yoro, T., Tanaka, H., Uraki, S., Kido, Y., Sanada, Y., Kuramoto, S., and Taira, A., 2009. Structural and seismic stratigraphic framework of the NanTroSEIZE Stage 1 transect. In Kinoshita, M., Tobin, H., Ashi, J., Kimura, G., Lallemand, S., Screaton, E.J., Curewitz, D., Masago, H., Moe, K.T., and the Expedition 314/315/316 Scientists, *Proc. IODP, 314/315/316*: Washington, DC (Integrated Ocean Drilling Program Management International, Inc.). doi:10.2204/iodp.proc.314315316.102.2009
- Moore, G.F., Taira, A., Klaus, A., et al., 2001. *Proc. ODP, Init. Repts.*, 190: College Station, TX (Ocean Drilling Program). doi:10.2973/odp.proc.ir.190.2001
- Nakano, T., Nakashima, Y., Nakamura, K., and Ikeda, S., 2000. Observation and analysis of internal structure of rock using X-ray CT. *Chishitsugaku Zasshi*, 106(5):363–378.
- Ogawa, Y., 1980. Beard-like veinlet structure as fracture cleavage in the Neogene siltstone in the Miura and Boso Peninsulas, central Japan. *Sci. Rep. Dept. Geol., Kyushu Univ.*, 13:321–327.
- Okada, H., and Bukry, D., 1980. Supplementary modification and introduction of code numbers to the low-latitude coccolith biostratigraphic zonation (Bukry, 1973; 1975). *Mar. Micropaleontol.*, 5:321–325. doi:10.1016/0377-8398(80)90016-X
- Papadopoulos, S.S., Bredehoeft, J.D., and Cooper, H.H., Jr., 1973. On the analysis of ‘slug test’ data. *Water Resour. Res.*, 9(4):1087–1089. doi:10.1029/WR009i004p01087
- Perch-Nielsen, K., 1985. Cenozoic calcareous nannofossils. In Bolli, H.M., Saunders, J.B., and Perch-Nielsen, K. (Eds.), *Plankton Stratigraphy*: Cambridge (Cambridge Univ. Press), 427–554.
- Raffi, I., 2002. Revision of the early-middle Pleistocene calcareous nannofossil biochronology (1.75–0.85 Ma). *Mar. Micropaleontol.*, 45(1):25–55. doi:10.1016/S0377-8398(01)00044-5
- Raffi, I., Backman, J., Fornaciari, E., Pälike, H., Rio, D., Lourens, L., and Hilgen, F., 2006. A review of calcareous nannofossil astrobiochronology encompassing the past 25 million years. *Quat. Sci. Rev.*, 25(23–24):3113–3137. doi:10.1016/j.quascirev.2006.07.007
- Raffi, I., Backman, J., Rio, D., and Shackleton, N.J., 1993. Plio–Pleistocene nannofossil biostratigraphy and calibration to oxygen isotope stratigraphies from Deep Sea Drilling Project Site 607 and Ocean Drilling Program Site 677. *Paleoceanography*, 8(3):387–408. doi:10.1029/93PA00755
- Richter, C., Acton, G., Endris, C., and Radsted, M., 2007. Handbook for shipboard paleomagnetists. *ODP Tech. Note*, 34. doi:10.2973/odp.tn.34.2007
- Rothwell, R.G., 1989. *Minerals and Mineraloids in Marine Sediments: An Optical Identification Guide*: London (Elsevier).
- Salisbury, M.H., Shinohara, M., Suetsugu, D., Arisaka, M., Diekmann, B., Januszczak, N., and Savov, I.P., 2006. Leg 195 synthesis: Site 1201—a geological and geophysical section in the West Philippine Basin from the 660-km discontinuity to the mudline. In Shinohara, M., Salisbury, M.H., and Richter, C. (Eds.), *Proc. ODP, Sci. Results*, 195: College Station, TX (Ocean Drilling Program), 1–27. doi:10.2973/odp.proc.sr.195.113.2006
- Schlumberger, 1989. *Log Interpretation Principles/Applications*: Houston (Schlumberger Educ. Services), SMP–7017.
- Schlumberger, 2002. *Efficient Acquisition of Quality Borehole Seismic—The Versatile Seismic Imager*: Houston (Schlumberger Educ. Services), SMP-5807. <http://www.slb.com/~media/Files/seismic/brochures/vsi.ashx>
- Shepard, F.P., 1954. Nomenclature based on sand-silt-clay ratios. *J. Sediment. Petrol.*, 24(3):151–158.
- Shinohara, M., Fukano, T., Kanazawa, T., Araki, E., Suyehiro, K., Mochizuki, M., Nakahigashi, K., Yamada, T., and Mochizuki, K., 2008. Upper mantle and crustal seismic structure beneath the Northwestern Pacific Basin using a seafloor borehole broadband seismometer and ocean bottom seismometers. *Phys. Earth Planet. Inter.*, 170(1–2):95–106. doi:10.1016/j.pepi.2008.07.039
- Shinohara, M., Hirata, N., Nambu, H., Suyehiro, K., Kanazawa, T., and Kinoshita, H., 1992. Detailed crustal structure of northern Yamato Basin. In Tamaki, K., Suyehiro, K., Allan, J., McWilliams, M., et al., *Proc. ODP, Sci. Results*, 127/128 (Pt. 2): College Station, TX (Ocean Drilling Program), 1075–1106. doi:10.2973/odp.proc.sr.127128-2.230.1992
- Shipboard Scientific Party, 1991. Explanatory notes. In Taira, A., Hill, I., Firth, J.V., et al., *Proc. ODP, Init. Repts.*, 131: College Station, TX (Ocean Drilling Program), 25–60. doi:10.2973/odp.proc.ir.131.104.1991

- Shiple, T.H., Ogawa, Y., Blum, P., et al., 1995. *Proc. ODP, Init. Repts.*, 156: College Station, TX (Ocean Drilling Program). doi:10.2973/odp.proc.ir.156.1995
- Su, X., 1996. Development of late Tertiary and Quaternary coccolith assemblages in the northeast Atlantic. *GEO-MAR Rep.*, 48.
- Underwood, M.B., Basu, N., Steurer, J., and Udas, S., 2003. Data report: normalization factors for semiquantitative X-ray diffraction analysis, with application to DSDP Site 297, Shikoku Basin. In Mikada, H., Moore, G.F., Taira, A., Becker, K., Moore, J.C., and Klaus, A. (Eds.), *Proc. ODP, Sci. Results*, 190/196: College Station, TX (Ocean Drilling Program), 1–28. doi:10.2973/odp.proc.sr.190196.203.2003
- Wiersberg, T., and Erzinger, J., 2007. A helium isotope cross-section study through the San Andreas Fault at seismogenic depths. *Geochem., Geophys., Geosyst.*, 8(1):Q01002. doi:10.1029/2006GC001388
- Young, J.R., 1998. Neogene. In Bown, P.R. (Ed.), *Calcareous Nannofossil Biostratigraphy*: Dordrecht, The Netherlands (Kluwer Academic Publ.), 225–265.
- Zoback, M.D., 2007. *Reservoir Geomechanics*: Cambridge (Cambridge Univ. Press).

Publication: 31 August 2010
MS 319-102

Figure F1. Washed cuttings work flow, Hole C0009A. PP = polypropylene, NGR = natural gamma ray, MAD = moisture and density, XRD = X-ray diffraction, XRF = X-ray fluorescence, CA = carbonate analyzer, TC = total carbon, TN = total nitrogen, EA = elemental analyzer. Red = only limited measurements performed on soft cuttings; unwashed cuttings (1 jar left) and separated washed grains kept at Kochi Core Center.

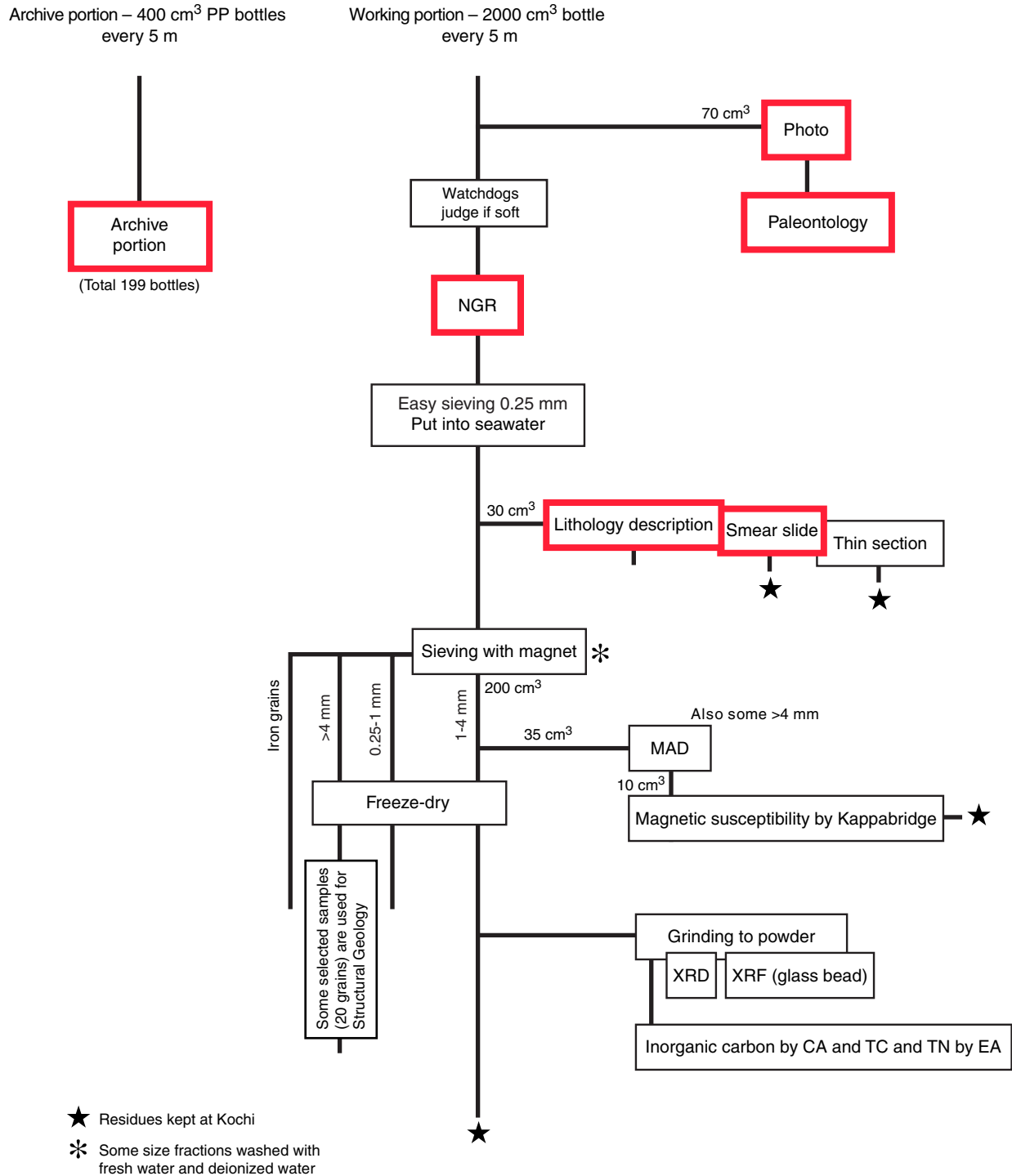


Figure F2. Core work flow, Hole C0009A. CT = computed tomography, WR = whole round, IW = interstitial water, MSCL-W = whole-round multisensor core logger, CA = carbonate analyzer, TC = total carbon, TN = total nitrogen, EA = elemental analyzer, XRD = X-ray diffraction, XRF = X-ray fluorescence.

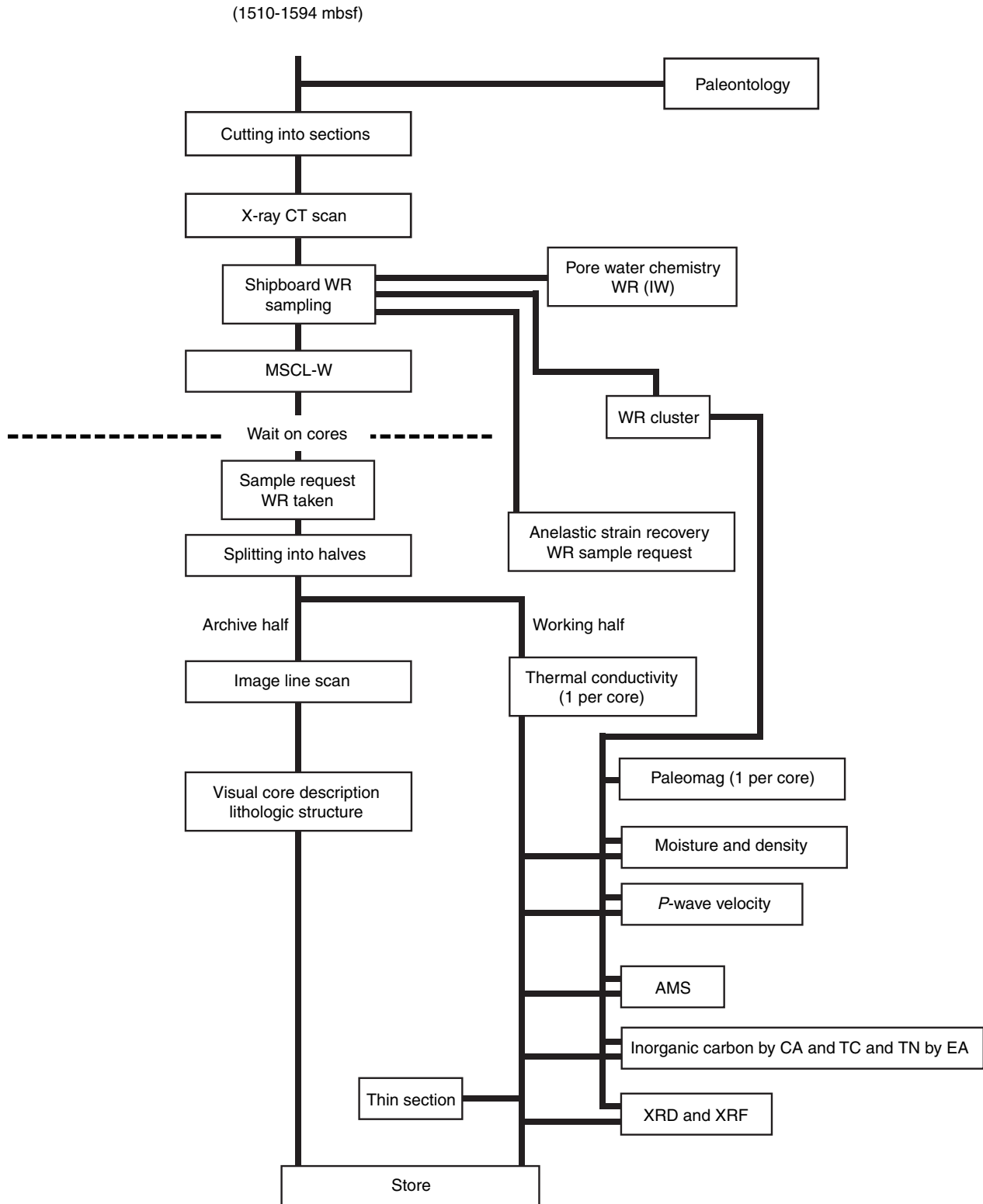




Figure F3. LWD/MWD tool strings used during Expedition 319. **A.** 26 inch hole drilled between seafloor and 711.8 m LSF, Hole C0009A. 825 HF = 8.25 inch high flow model, APWD = annular pressure while drilling, ARC-8 = 8.25 inch Array Resistivity Compensated tool. **B.** 12.25 inch hole drilled between 707.7 and 1509.7 m LSF, Hole C0009A. **C.** 12.25 inch hole drilled between 41 and 560 m LSF, Hole C0010A. RAB-08 = 8.25 inch resistivity at the bit.

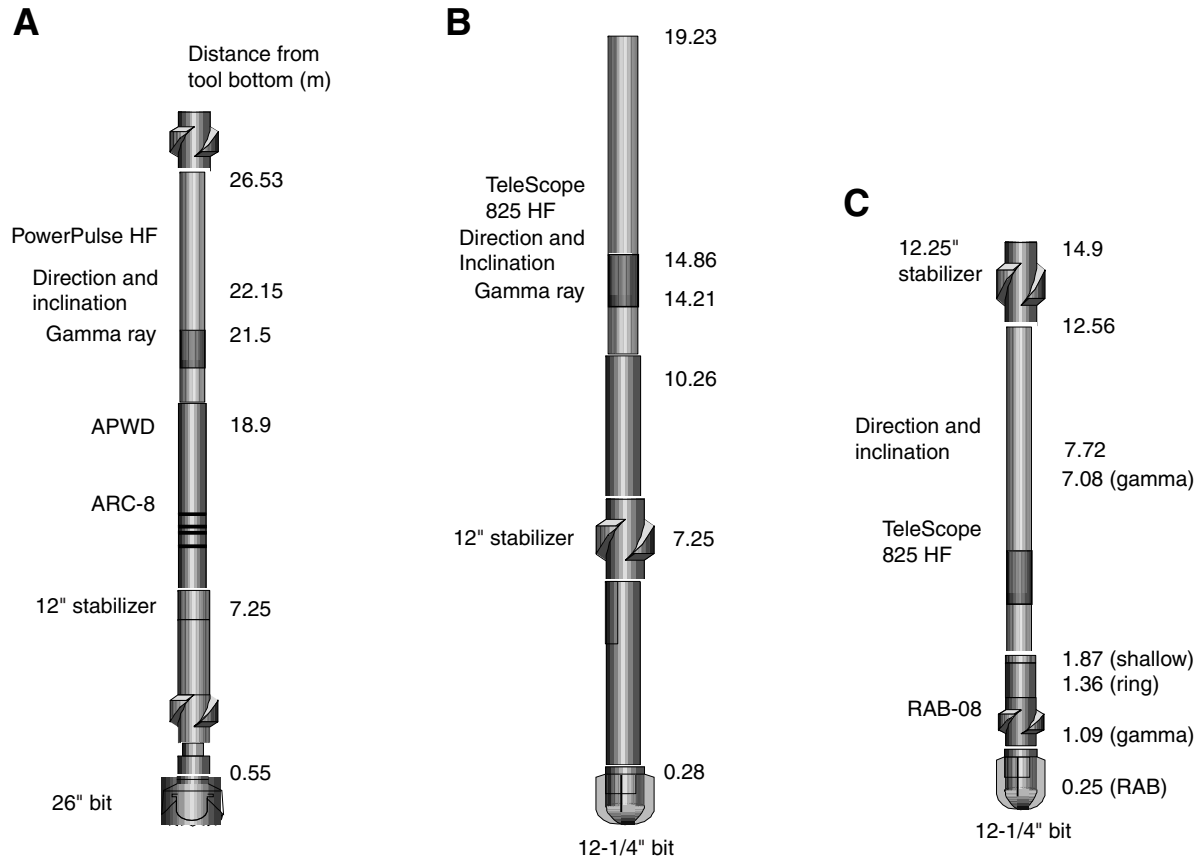


Figure F4. A. Schematic of rig instrumentation used for logging-while-drilling (LWD)/measurement-while-drilling (MWD) operations. B. Schematic of passive heave compensating system used during wireline logging operations at the riser site.

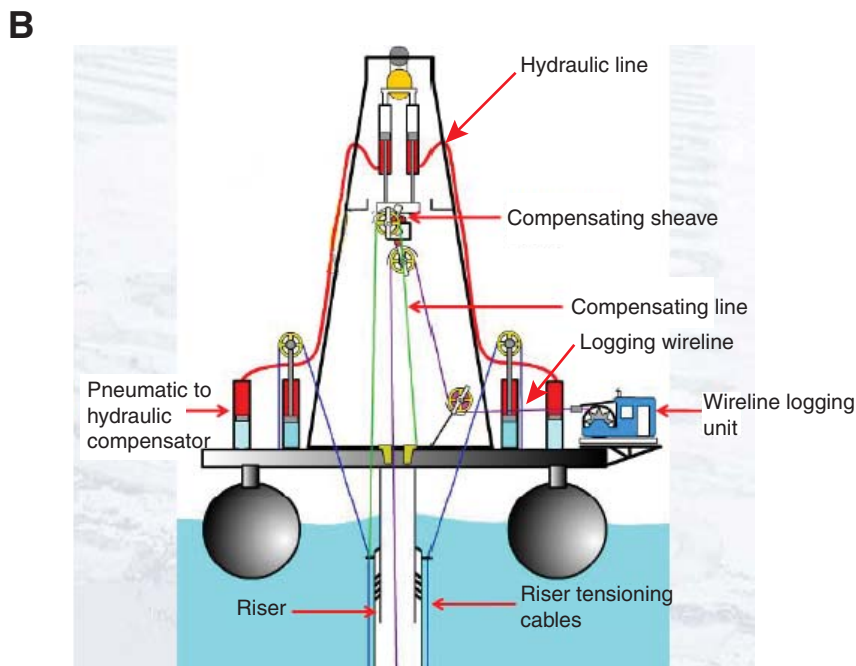
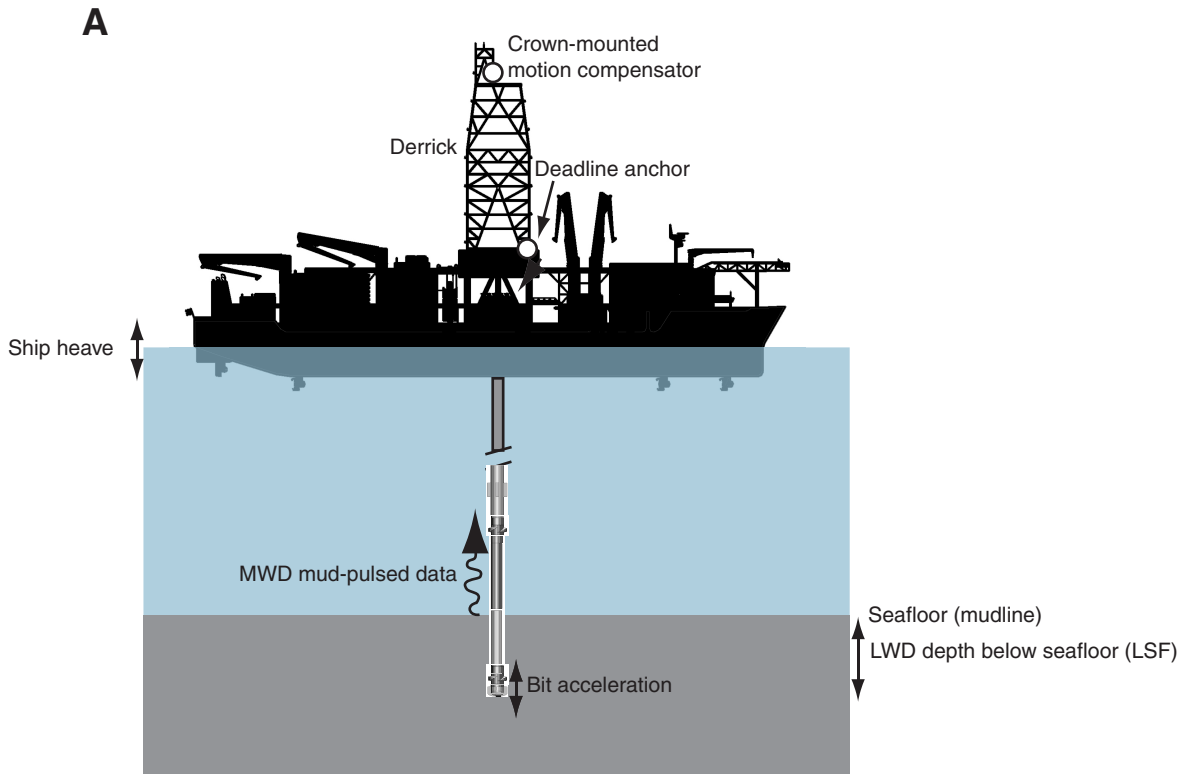




Figure F5. Shipboard structure and data flow. MWD = measurement while drilling, APWD = annular pressure while drilling, LWD = logging while drilling, IDEAL = integrated drilling evaluation and logging surface system, MAXIS = Multitask Acquisition Imaging System, CDEX = Center for Deep Earth Exploration, LAS = log ASCII standard, DLIS = digital logging interchange standard, SEG Y = Society of Exploration Geophysicists standard Y.

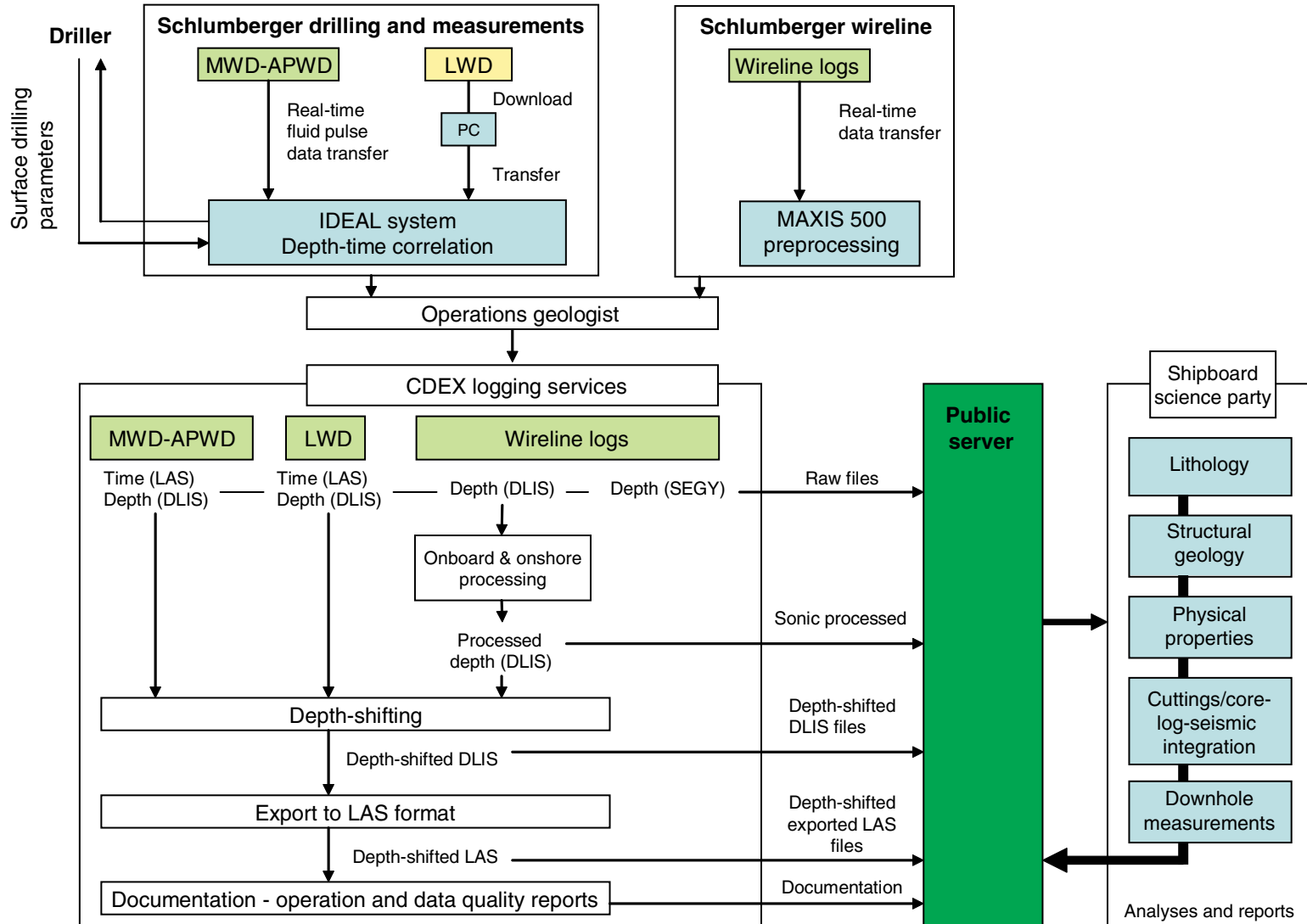


Figure F6. A. Configuration and principle of MWD fluid pulse telemetry. B. Position and components of geo-VISION tool. C. Mud pulse data recording and processing. SPT = signal pulse transducer, HSPM = horizon signal processing module, IDEAL = integrated drilling evaluation and logging surface system.

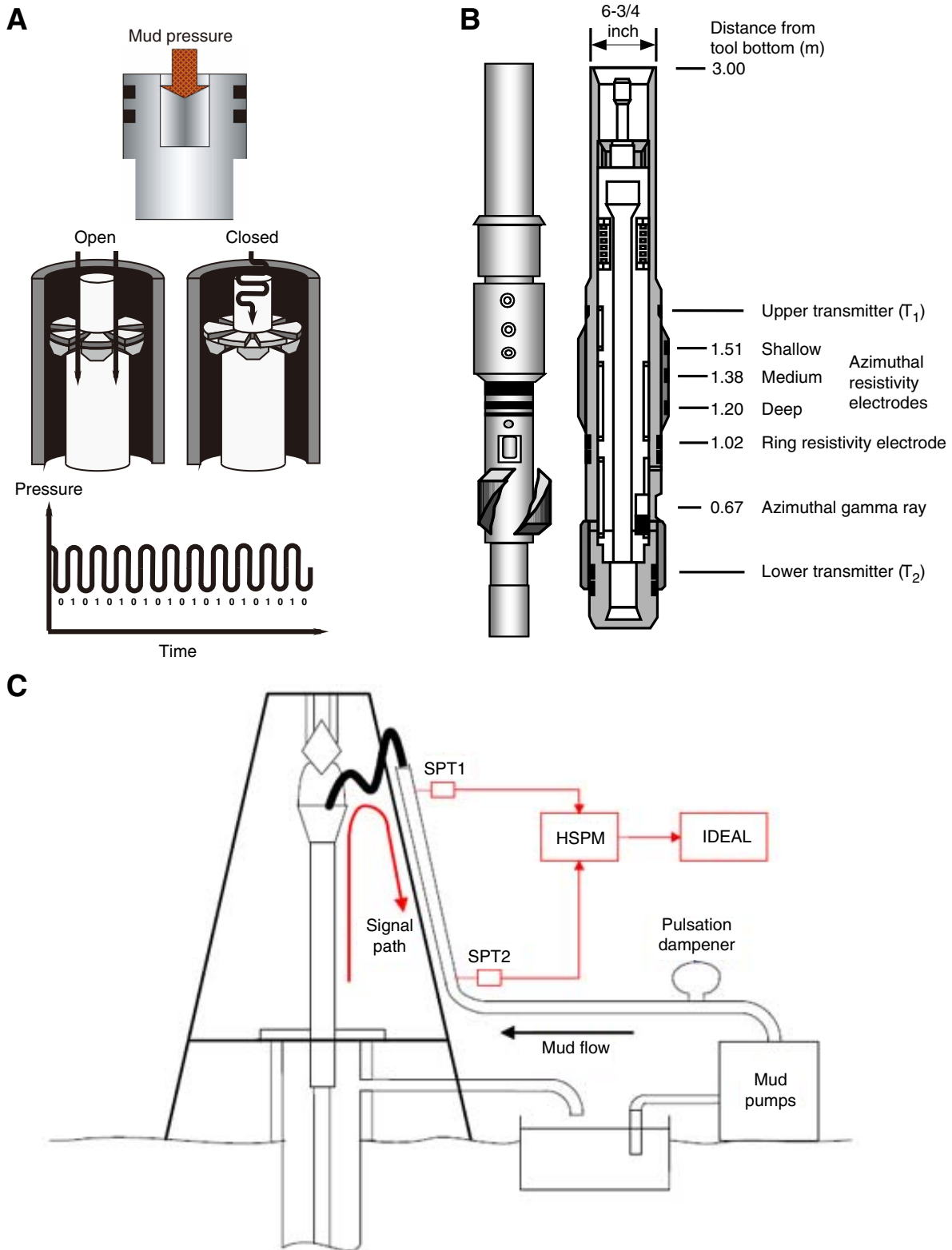


Figure F7. Position and components of wireline logging tools. **A.** HRLA. **B.** FMI. **C.** Sonic Scanner. Platform Express tools: **(D)** Highly Integrated Gamma Ray Neutron Sonde (HGNS) and **(E)** Micro-Cylindrically Focused Log (MCFL).

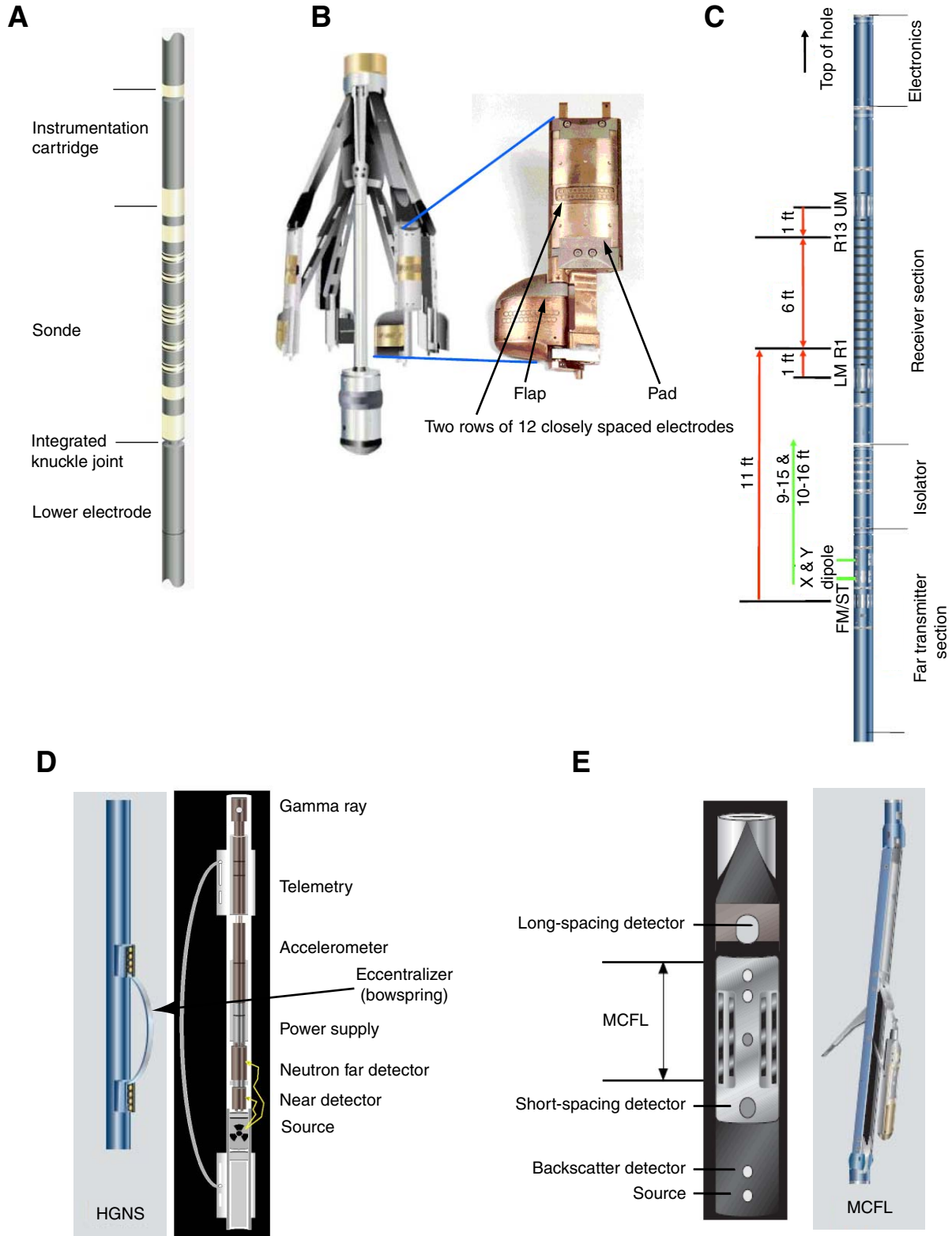



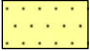















Figure F8. Graphic patterns and symbols used on visual core descriptions, Expedition 319.

Lithology

| | | | |
|---|-----------------|---|-------------------------|
|  | Claystone |  | Silty sandstone |
|  | Silty claystone |  | Sandstone |
|  | Siltstone |  | Tuff |
|  | Sandy siltstone |  | Volcaniclastic mudstone |

Sedimentary structure

| | |
|---|-----------------------------------|
|  | Slight bioturbation |
|  | Moderate bioturbation |
|  | Heavy bioturbation |
|  | Fining upward |
|  | Coarsening upward |
|  | Ripple cross-lamination |
|  | Planar bedding (lamination) |
|  | Flaser bedding/flaserlike bedding |
|  | Load structure |

Drilling disturbance





| | |
|---|---|
|  | Moderately fractured by drilling or splitting |
|  | Heavily fractured by drilling or splitting |
|  | Drilling breccia |
|  | Moderately disturbed |

Figure F9. Examples of X-ray diffractograms for mixtures of standard minerals showing positions of diagnostic peaks used to calculate relative mineral abundance. Green line = baseline subtraction. cps = counts per second.

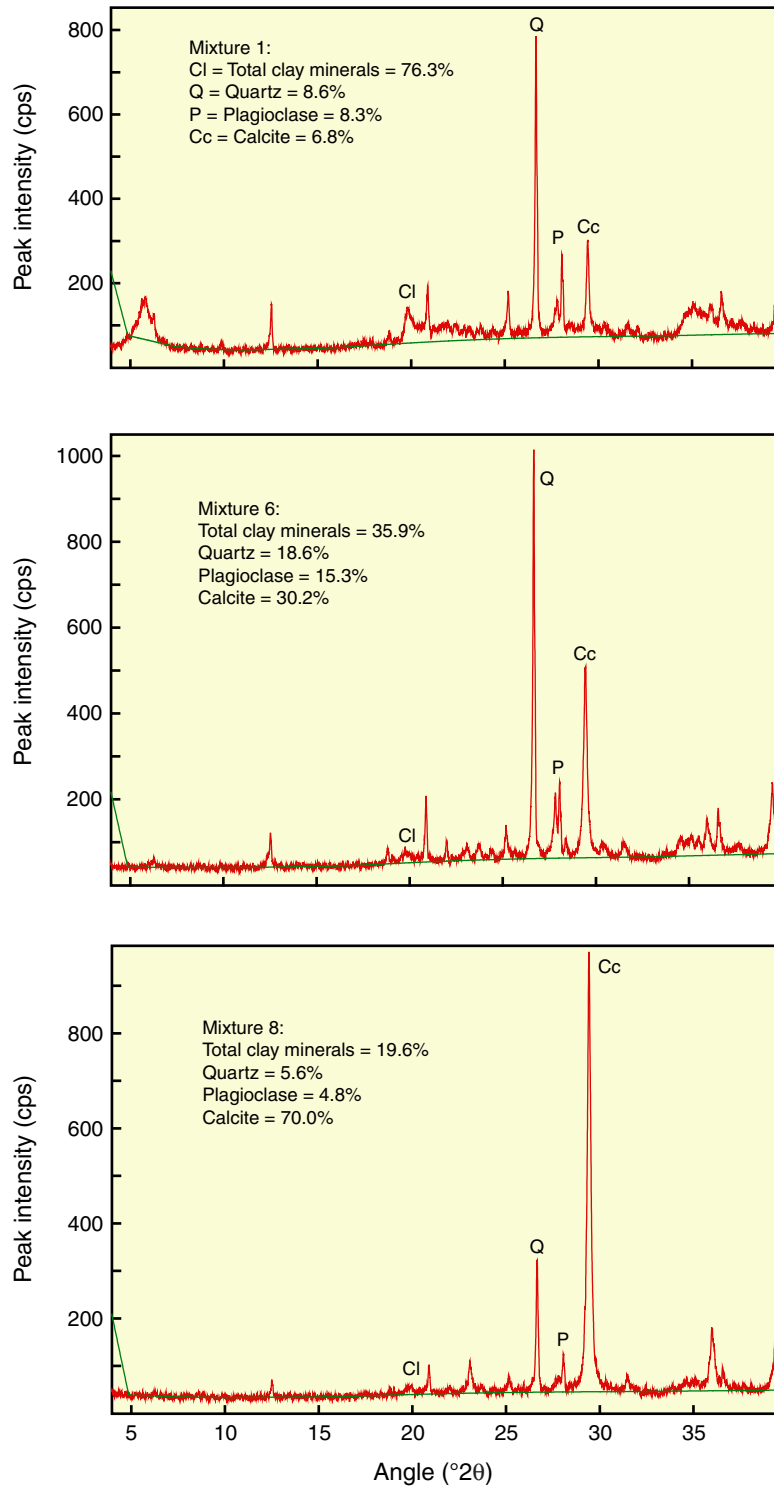


Figure F10. Photograph of modified protractor used to measure apparent dips, trends, plunges, and rakes on planar and linear features in a split core from Leg 131 (Shipboard Scientific Party, 1991) and Expedition 315 (Expedition 315 Scientists, 2009).

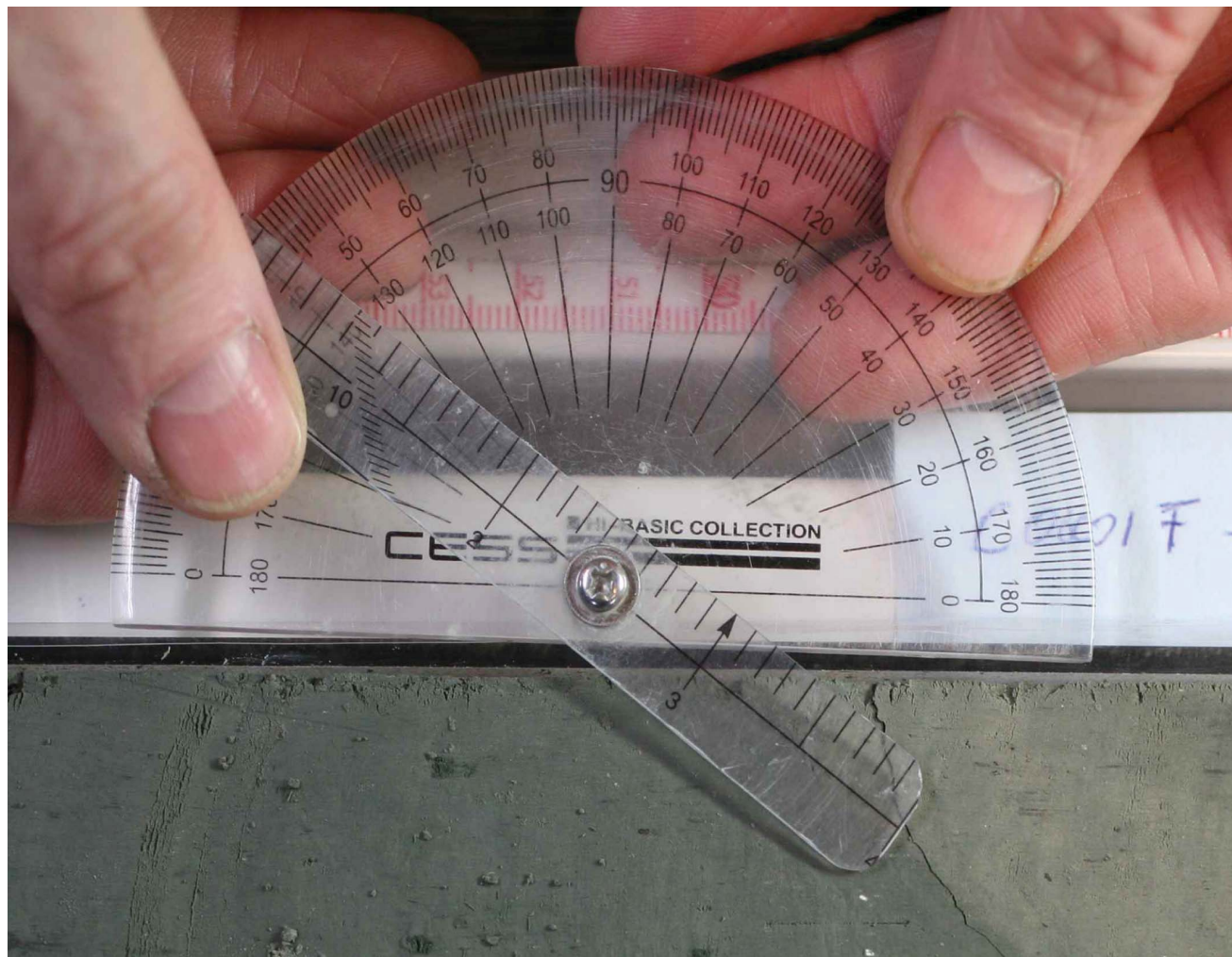


Figure F11. Core reference frame and x -, y -, and z -coordinates used in orientation data calculations from Leg 131 (Shipboard Scientific Party, 1991) and Expedition 315 (Expedition 315 Scientists, 2009).

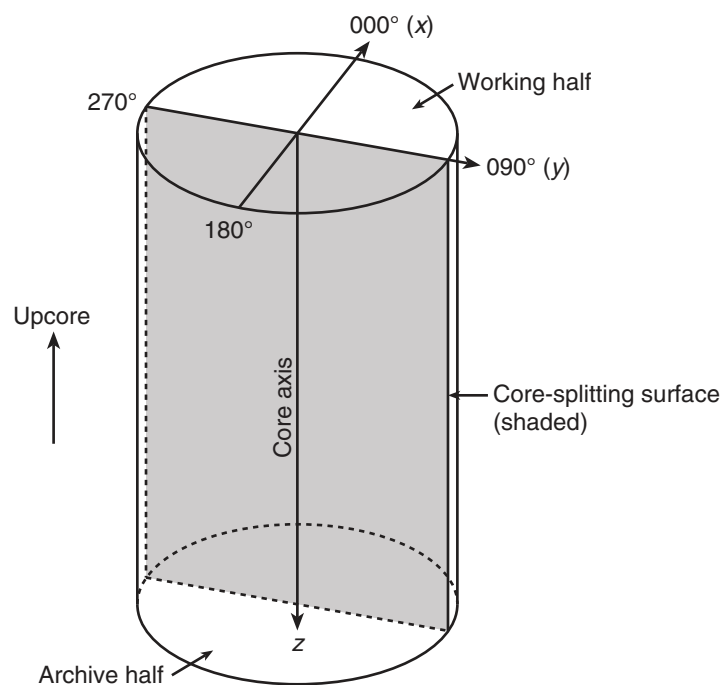


Figure F12. Late Cenozoic magnetostratigraphic and calcareous nannofossil events (Raffi et al., 2006; modified after Expedition 315 Scientists, 2009). FO = first occurrence, LO = last occurrence, RE = reentrance. Polarity: black = normal, white = reversal.

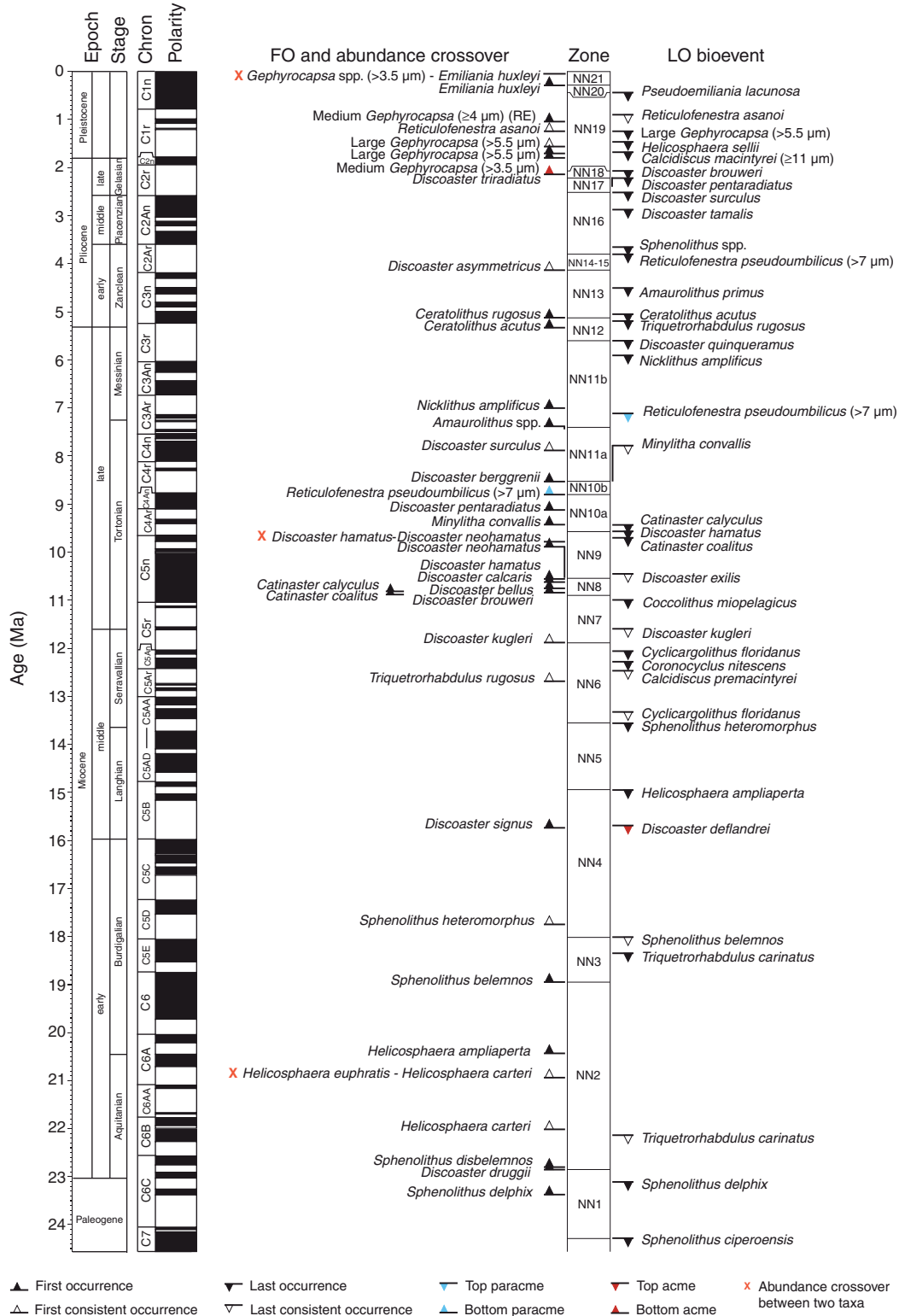




Figure F13. System used for real-time drilling mud gas extraction and analysis during Expedition 319 including location of gas separator during drilling Phases 3 and 8. FID = flame ionization detector.

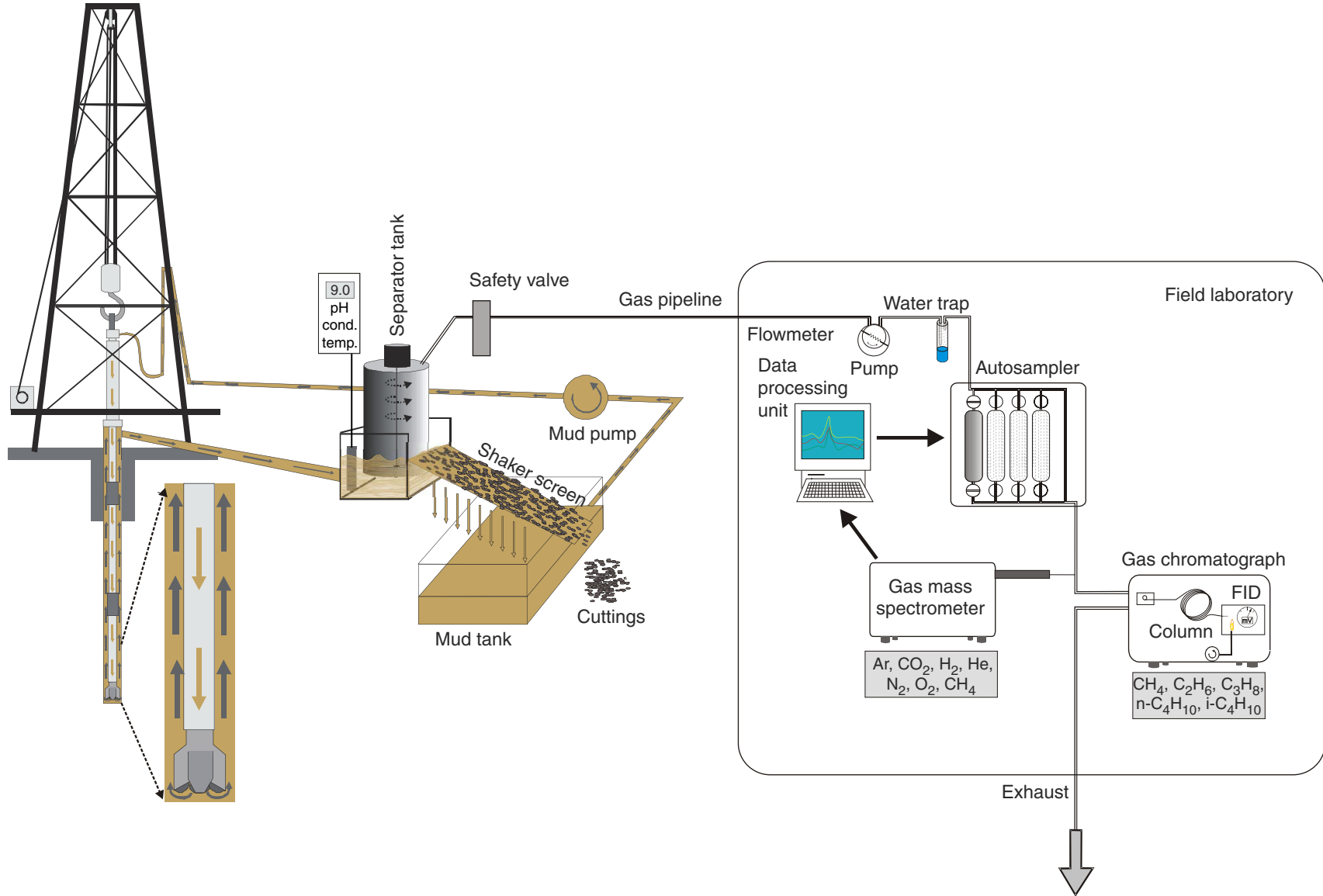


Figure F14. Location of gas separator during Drilling Phase 2 (plan view). GFZ = GeoForschungsZentrum (German Research Center for Geoscience).

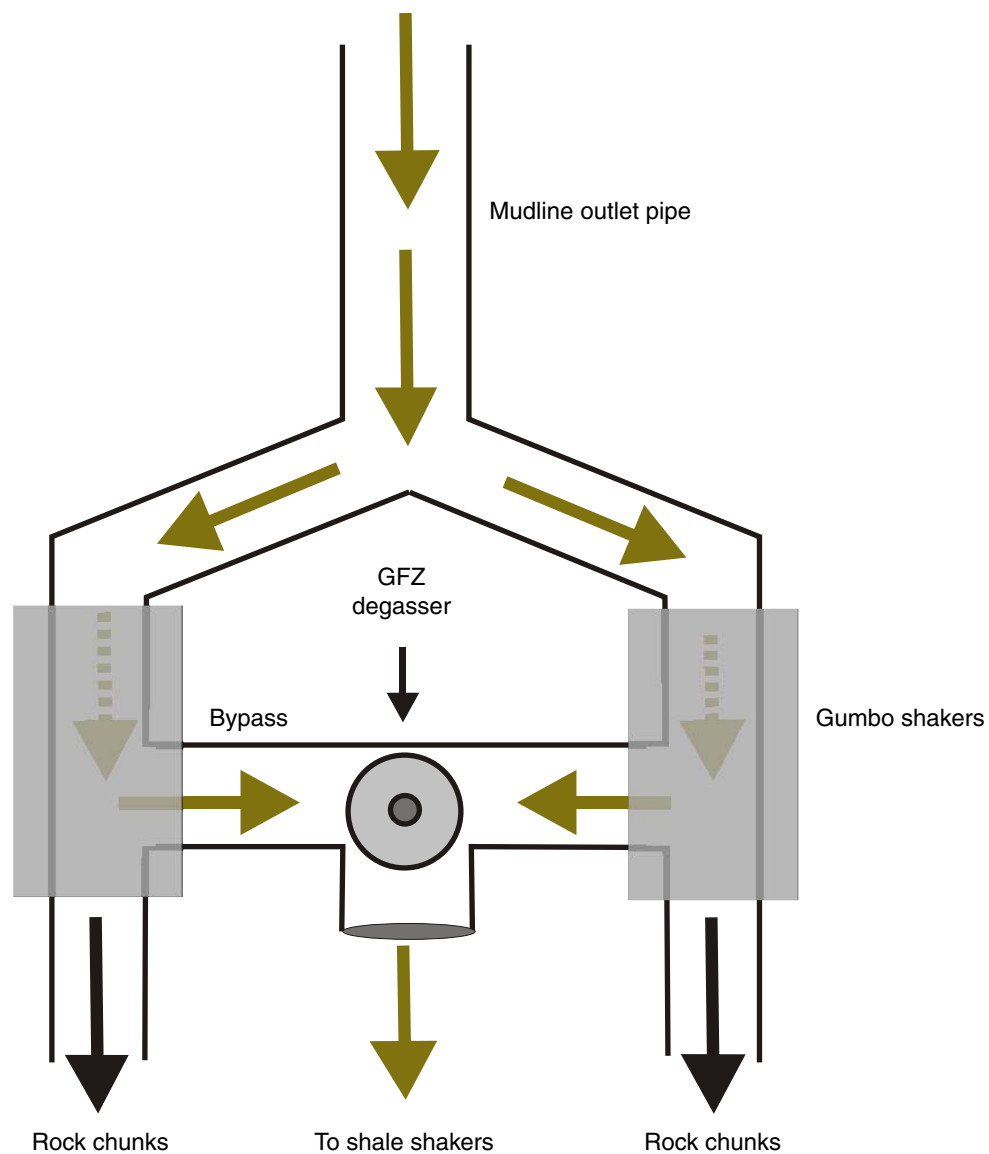


Figure F15. Schematic diagram of position and components of single probe module of MDT tool. CQG = crystal quartz gauge.

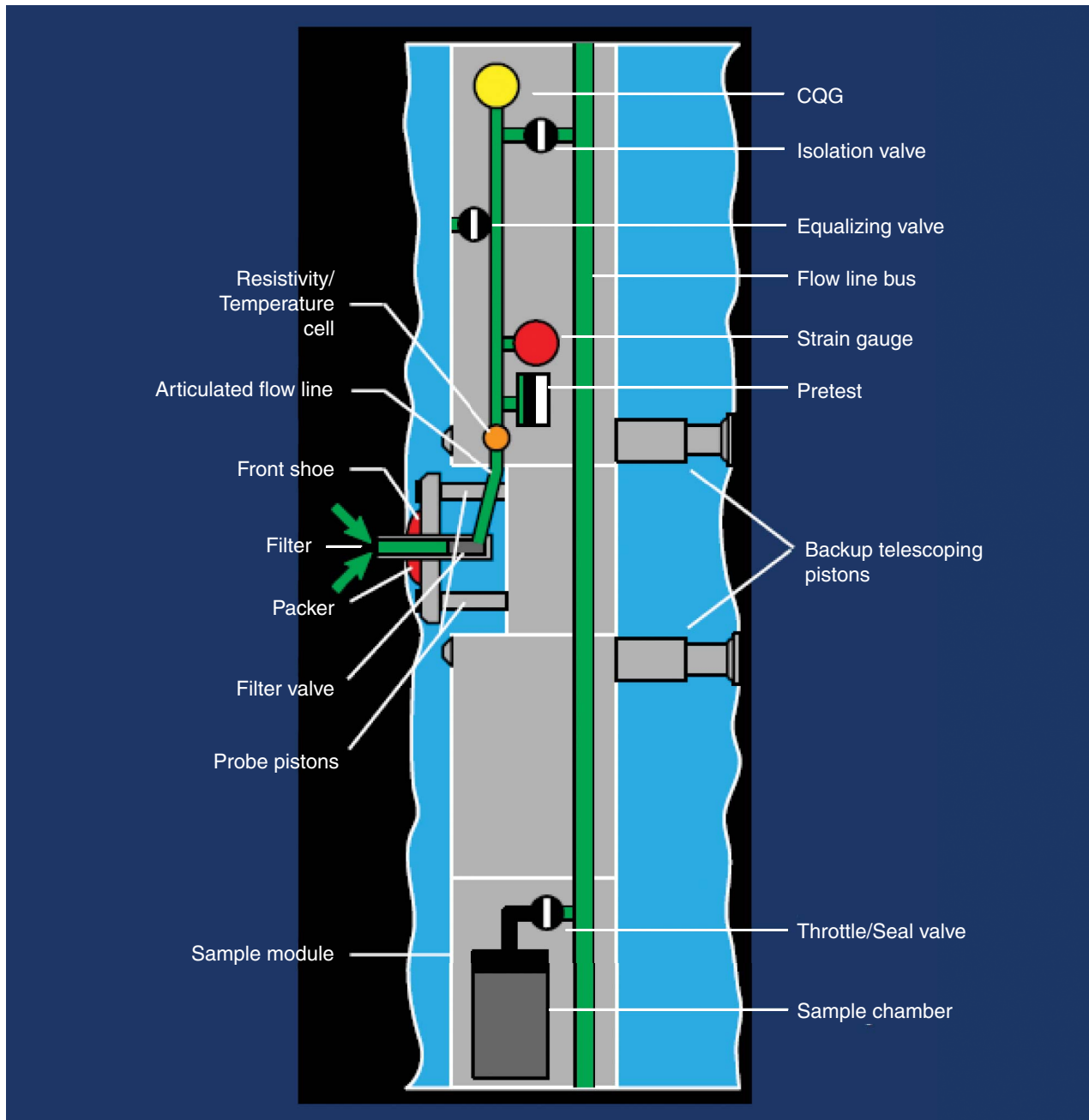


Figure F16. Diagram of MDT tool configured for use at Site C0009.

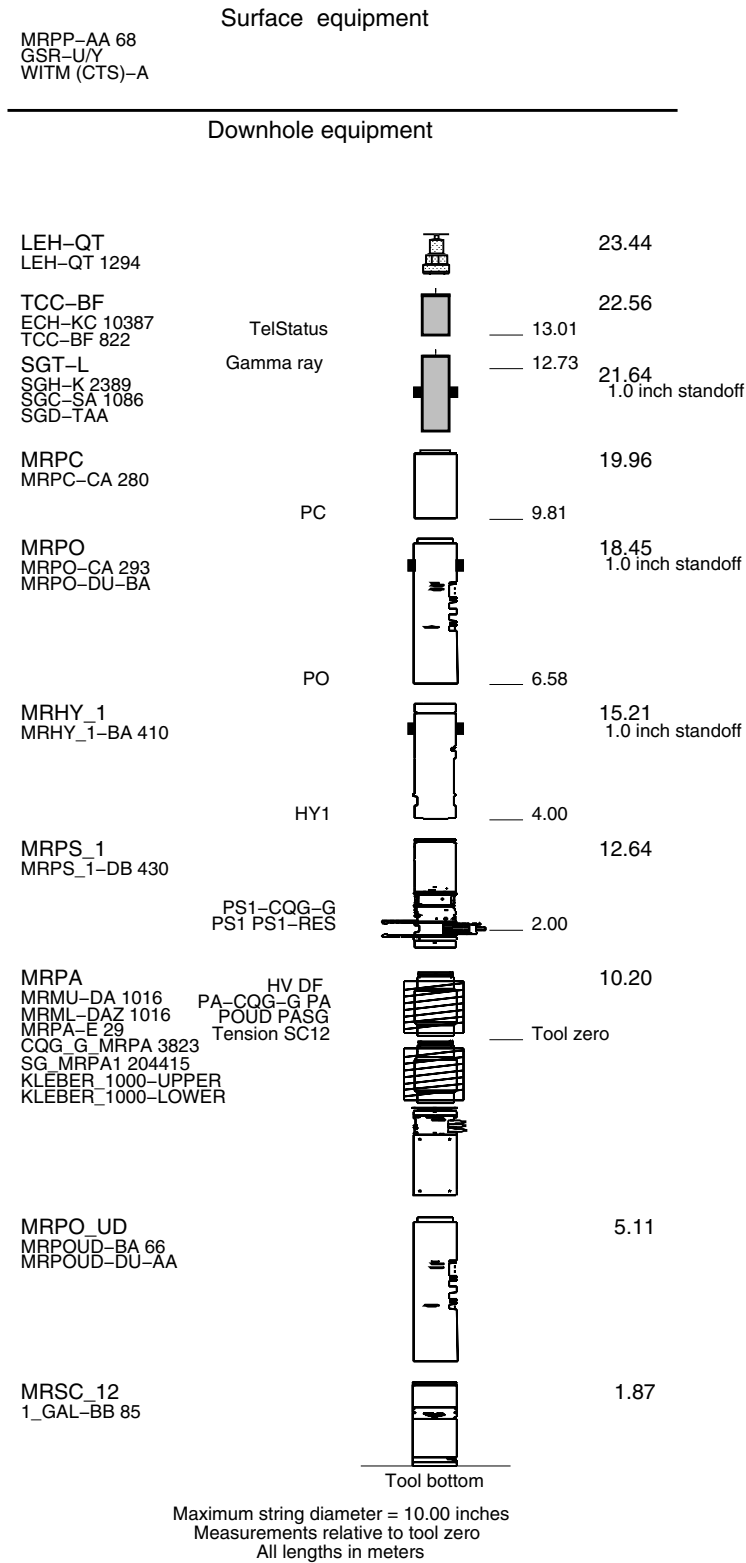




Figure F17. Diagram of MDT tool (center), with photographs showing dual packer module (left) and single probe module (right).

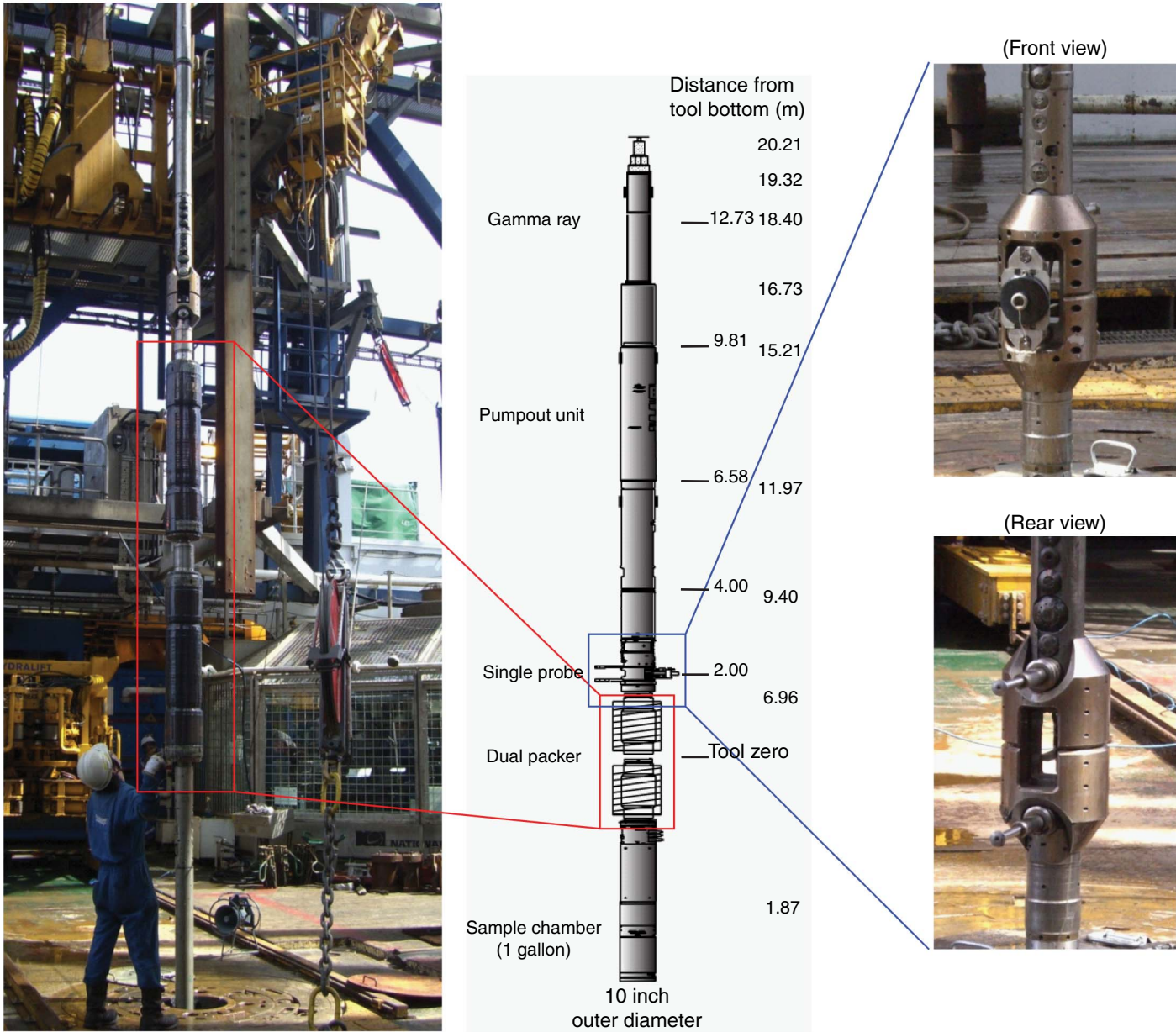


Figure F18. Schematic diagram illustrating concept for dual packer hydraulic fracturing tests.

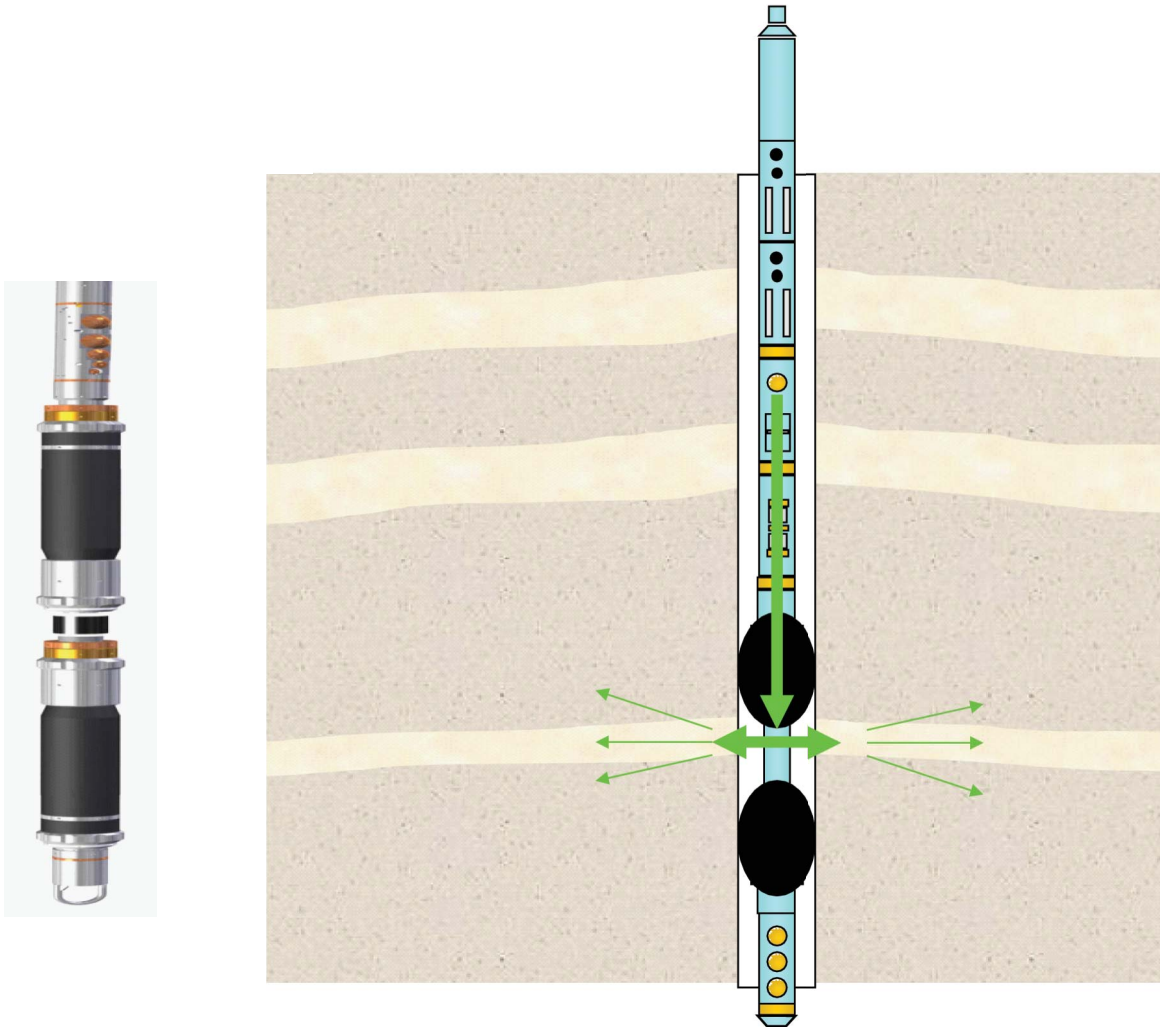


Figure F19. Location map of survey lines, Site C0009 (proposed Site NT2-11B). Line 1 shooting from southeast (B) to northwest (A), and Circle 1. Red circles = broadband ocean-bottom seismometers (BBOBSs), blue points = 8 short period ocean-bottom seismometers (OBSs) deployed by *Kairei* around *Chikyu*, thin gray lines = previous 2-D seismic surveys, shaded areas = previous 3-D and dense 2-D survey.

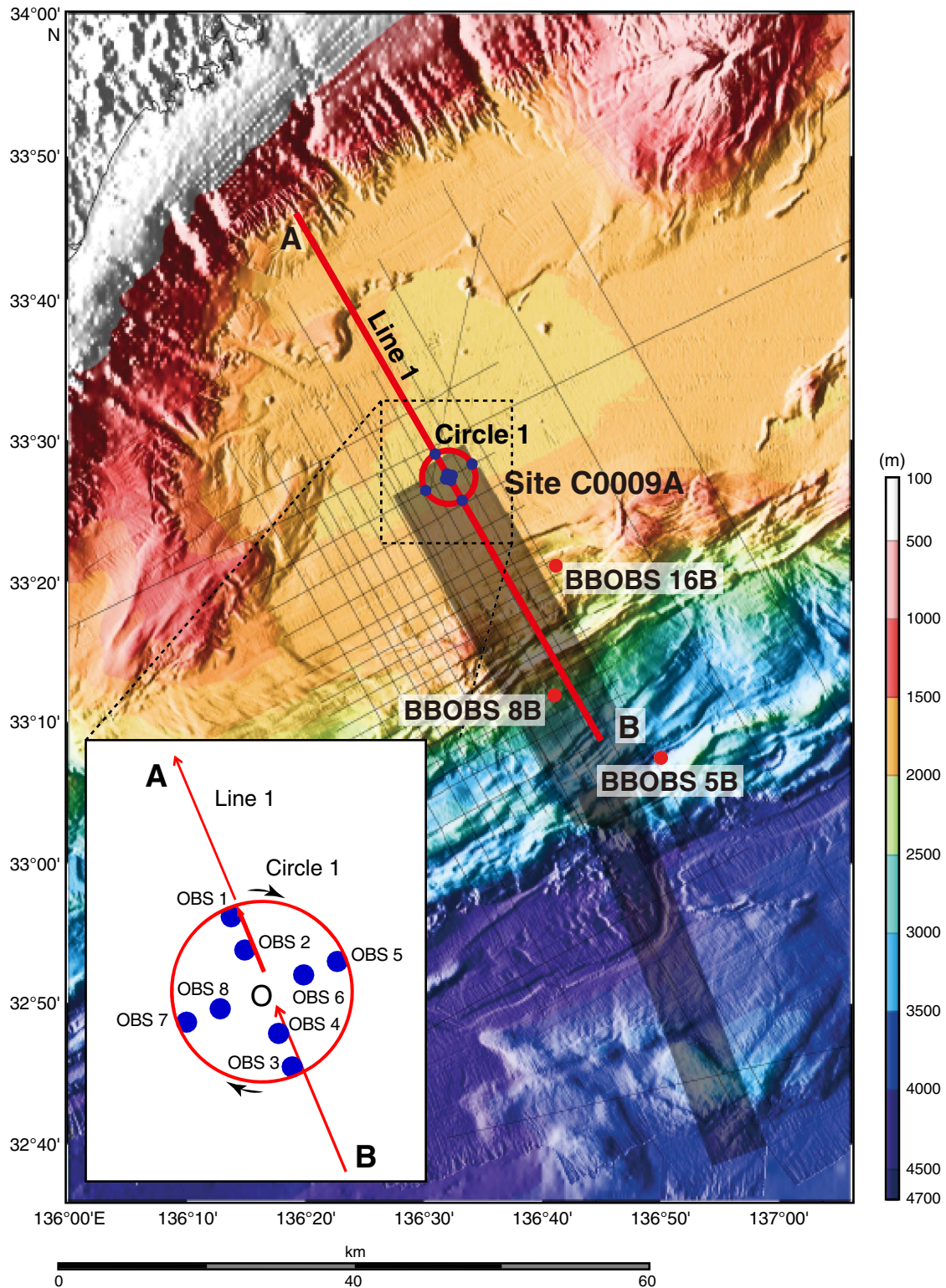




Figure F20. Schematic of walkaway VSP experiment concept.

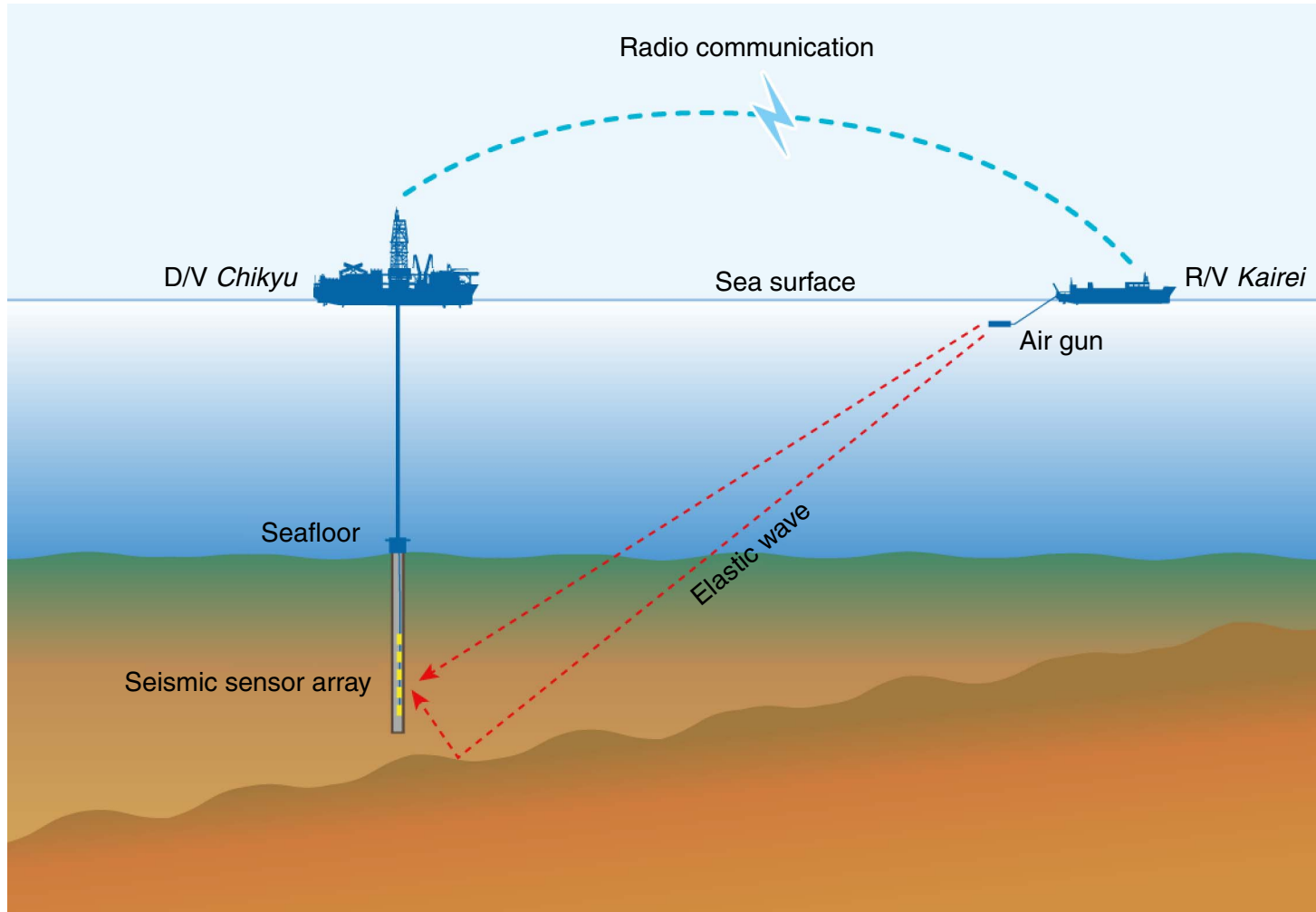


Figure F21. Configuration of air gun array towed from *Kairei*.

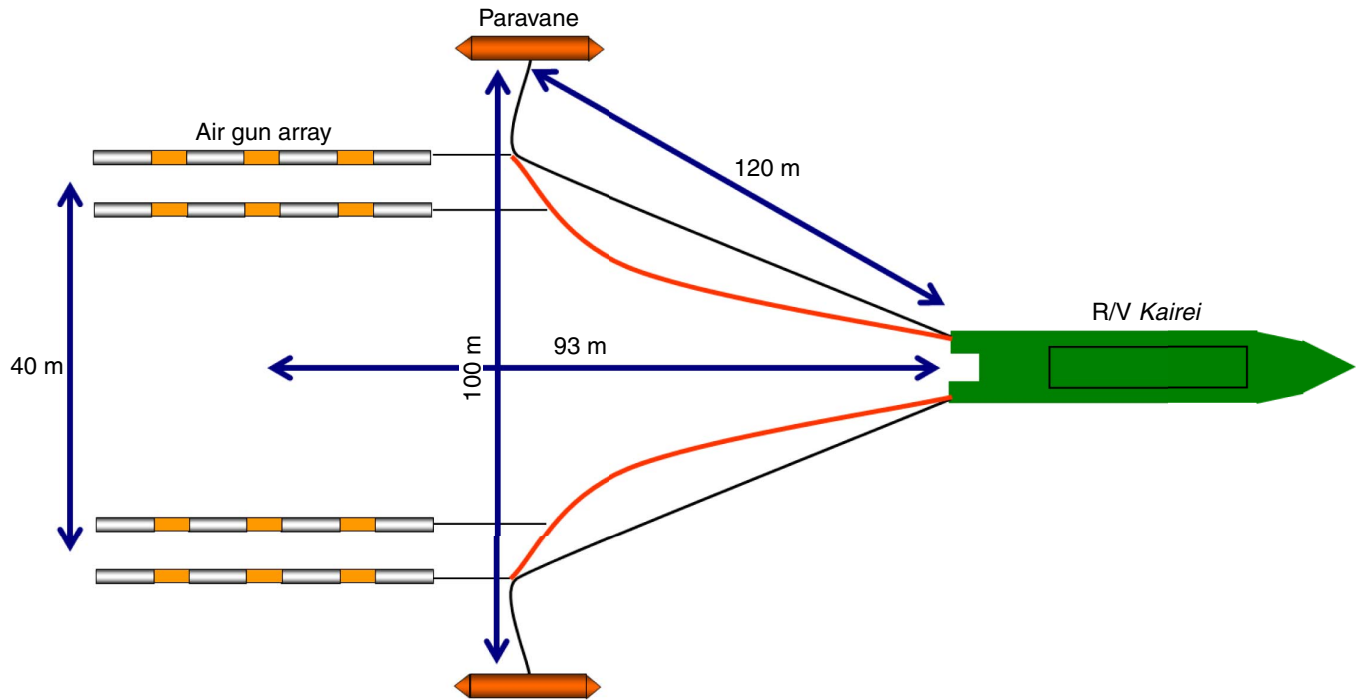


Figure F22. Acquisition geometry of zero-offset VSP on the *Chikyu*.

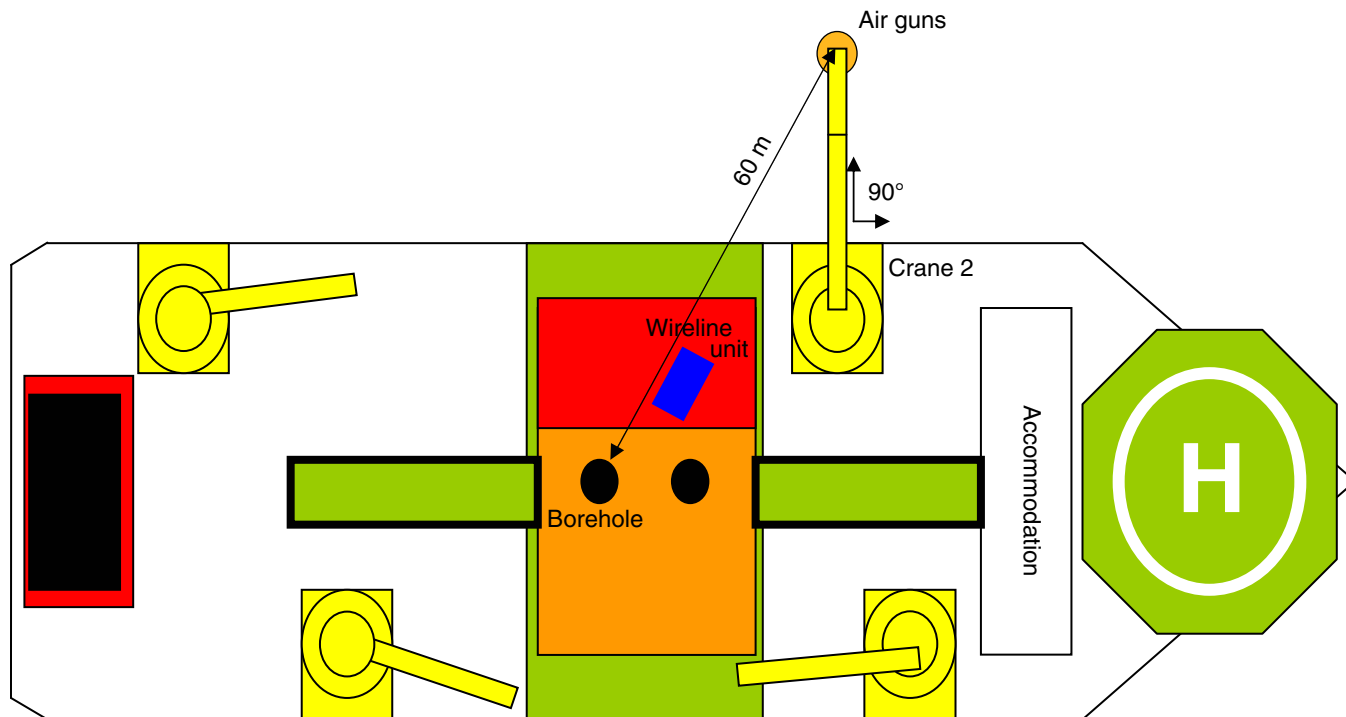


Figure F23. Photographs of air gun system. A. Air gun array. B. Deployment of air gun. C. Air gun shooting.

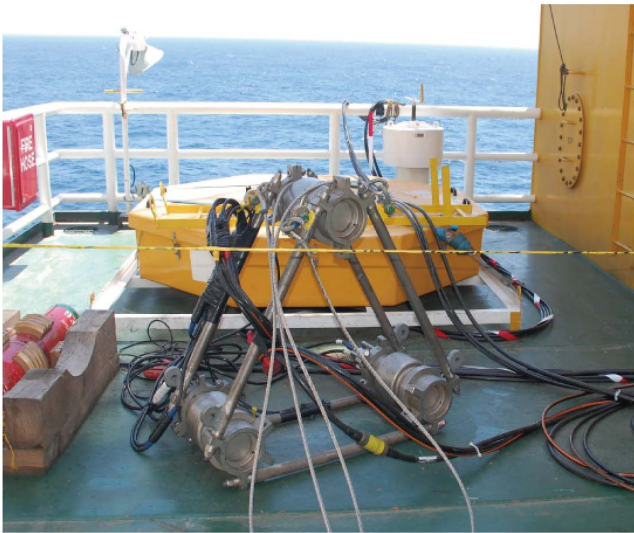
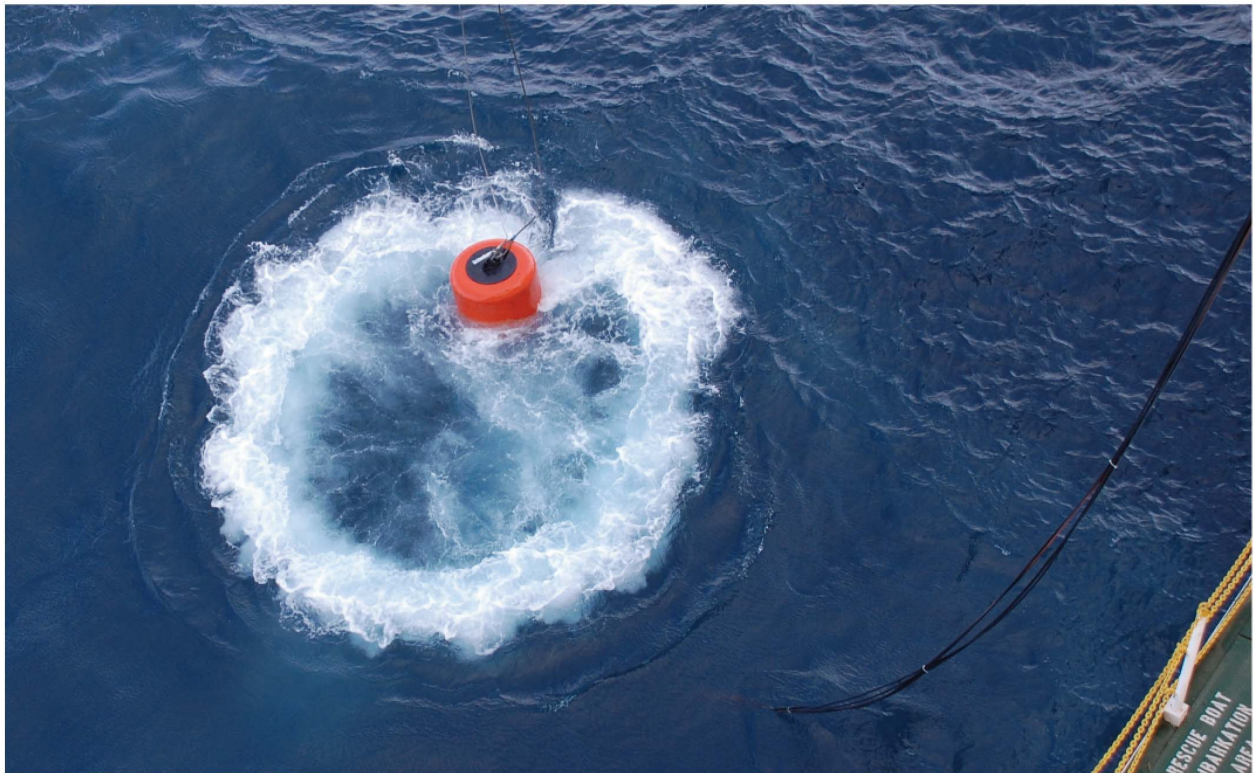
A**B****C**

Figure F24. Schematic diagram of dummy run test string, Hole C0010A. XO = crossover, EUE = external upset end, VAM = Vallourec and Mannesmann, MTL = miniature temperature logger.

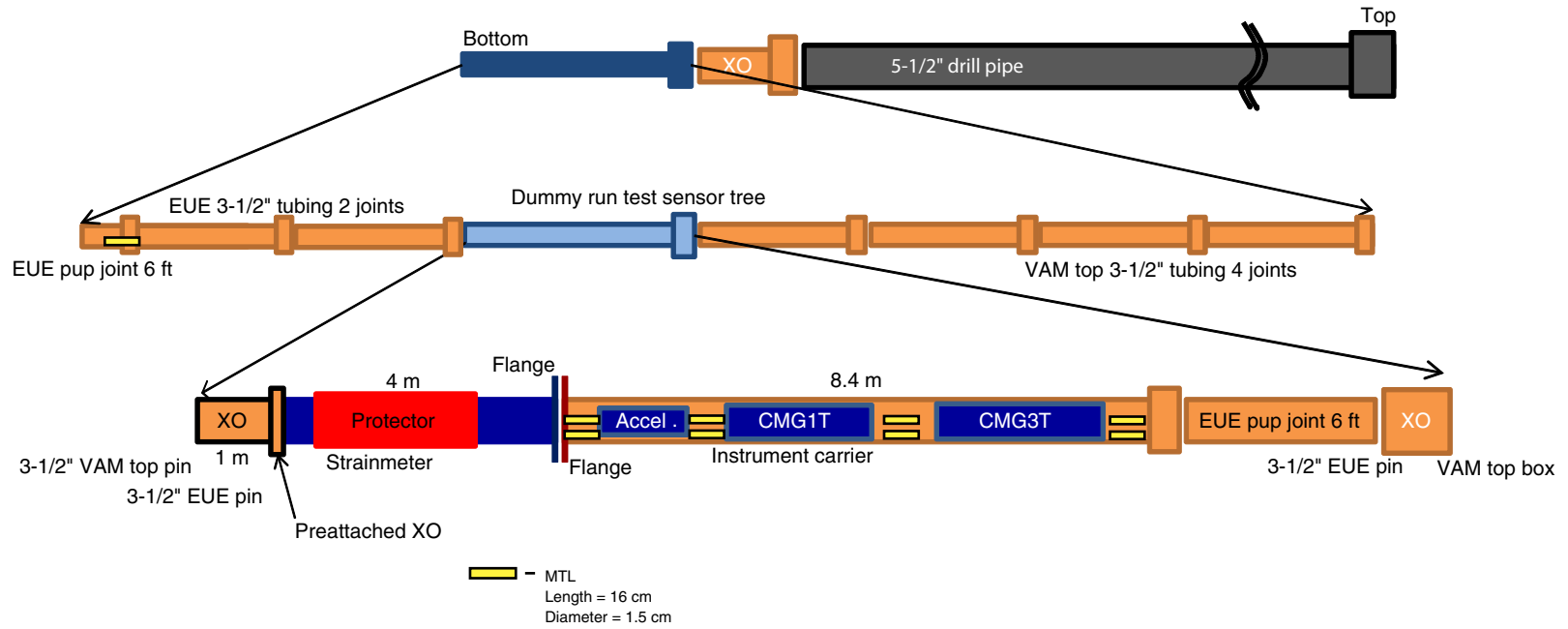




Figure F25. Schematic drawing of strainmeter. EUE = external upset end, OD = outside diameter.

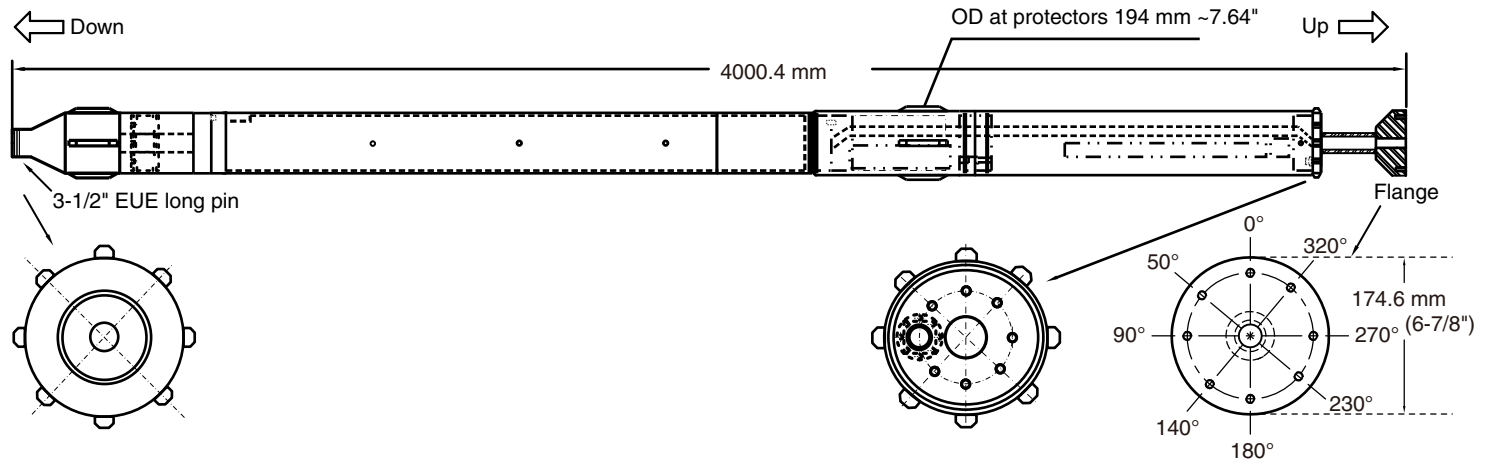


Figure F26. Schematic drawing of instrument carrier. EUE = external upset end, OD = outside diameter, ID = inside diameter.

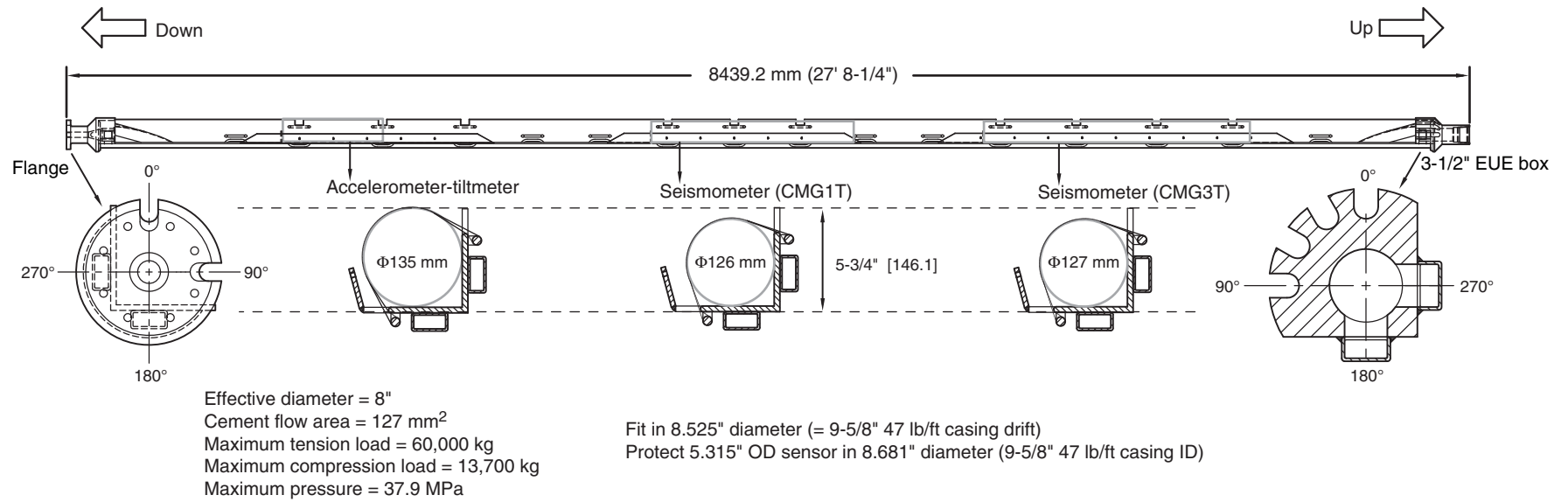


Figure F27. Cross section of instrument carrier, top view, showing orientation of sensors.

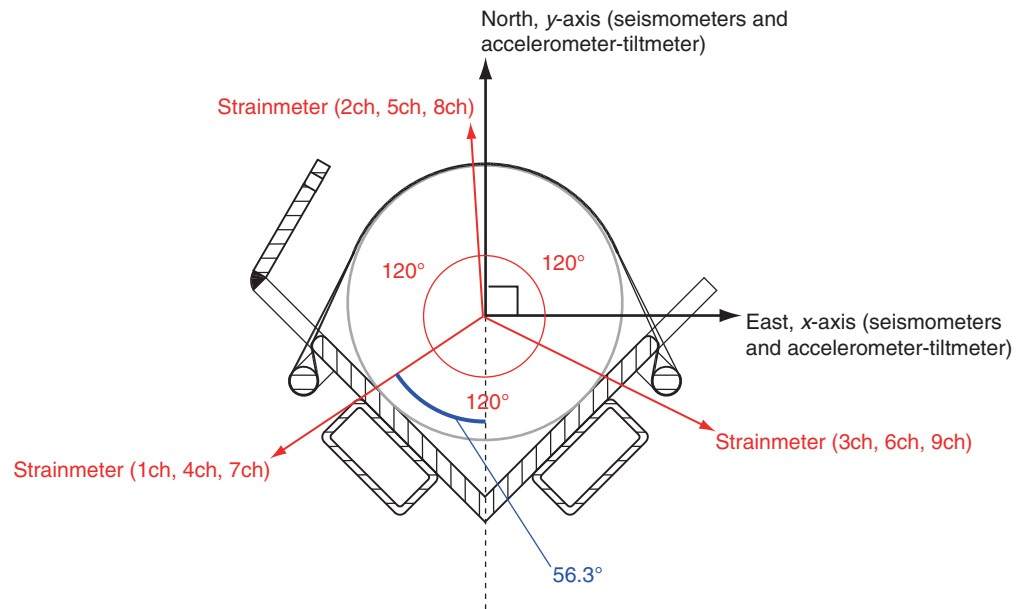


Figure F28. Schematic of planned long-term observatory, Hole C0010A. CORK = circulation obviation retrofit kit, ROV = remotely operated vehicle.

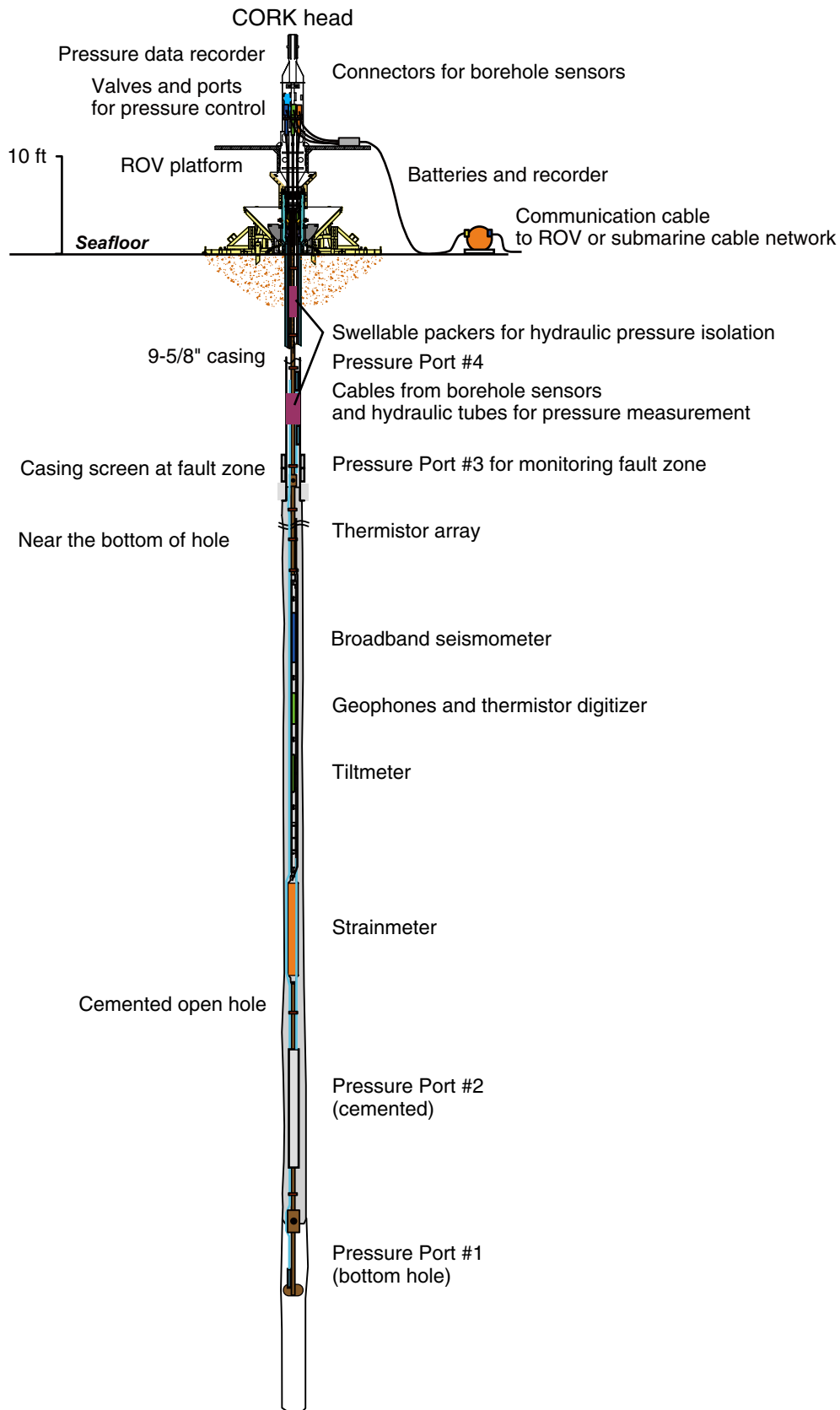


Figure F29. Diagram of borehole configuration for smart plug deployment.

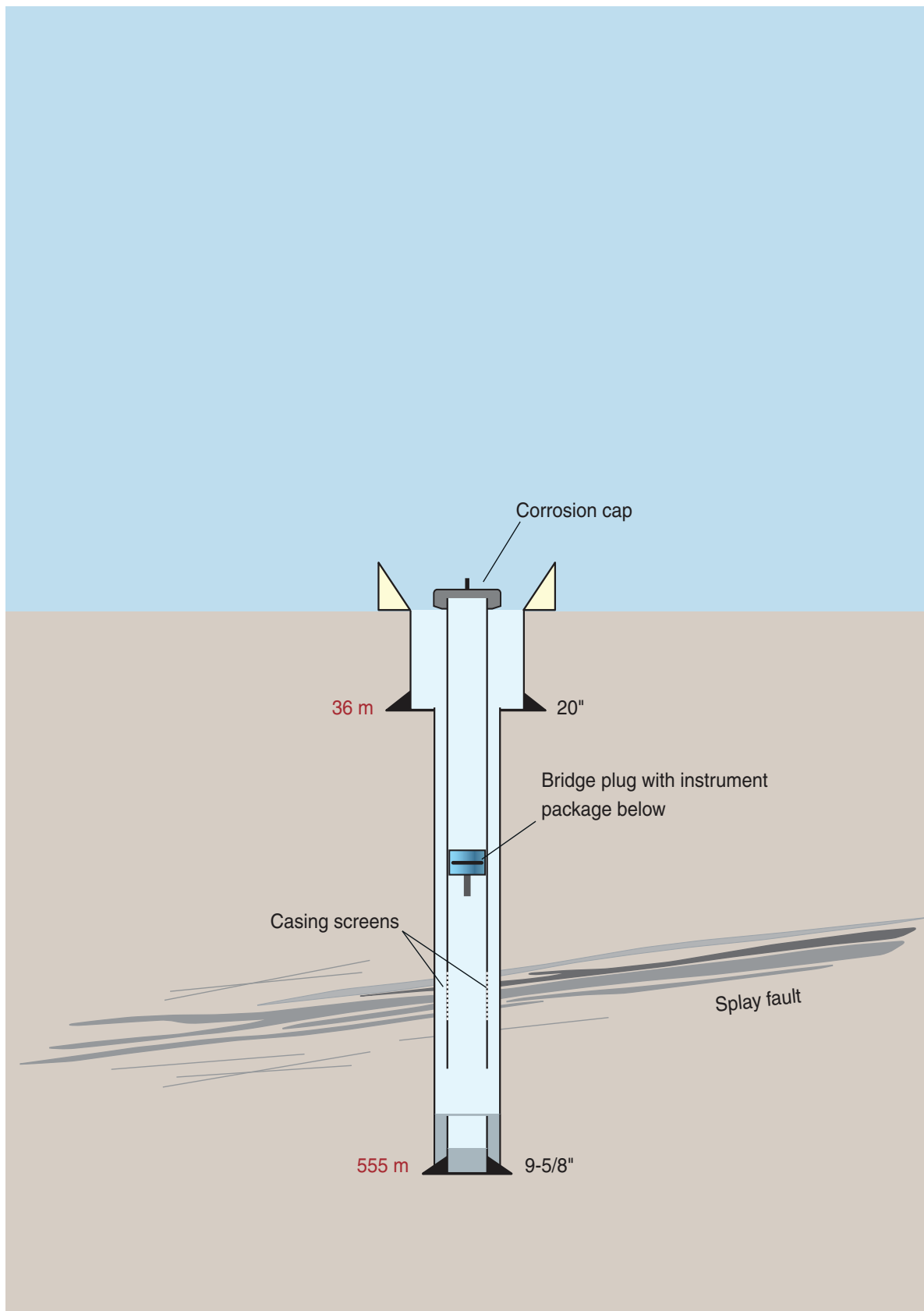
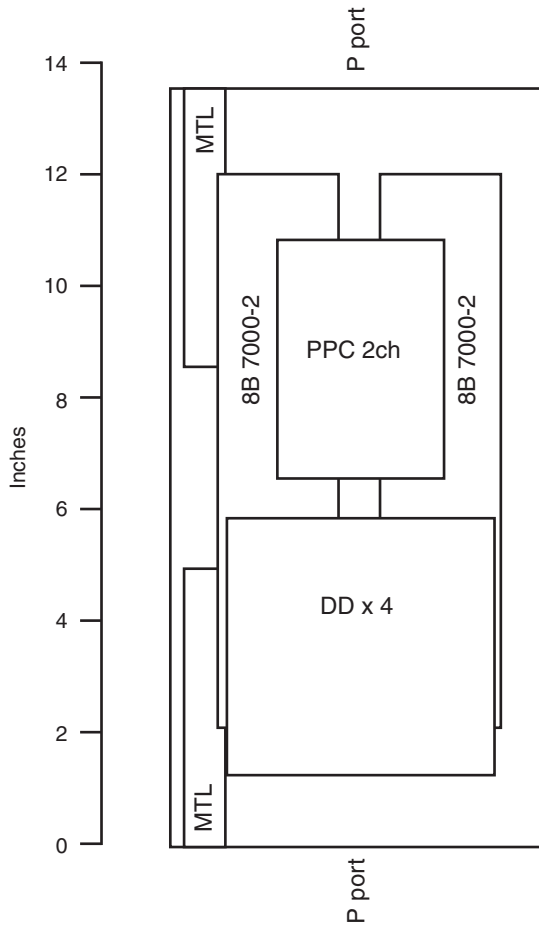


Figure F30. Diagram of smart plug (instrumented bridge plug). **A.** Side view. **B.** Cross-sectional top view. PPC = pressure period counter/logger, DD = lithium thionyl chloride batteries (7 y capacity at 1 min sampling rate), 8B 7000-2 = paroscientific pressure transducer, MTL = Antares miniature temperature logger. Pressure case = 6 inch diameter, 8 inch OD, flange-mounted end caps with high-pressure port feed through bulkheads leading to pressure sensors. Top end cap fabricated with 3.5 inch OD EU 8RD thread for mounting to Baker-Hughes retrievable casing packer.

A



B

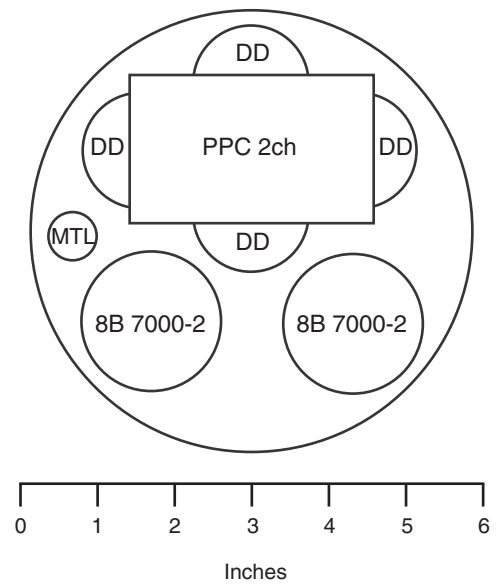


Figure F31. Photograph of smart plug instrument package. MTL = miniature temperature logger.

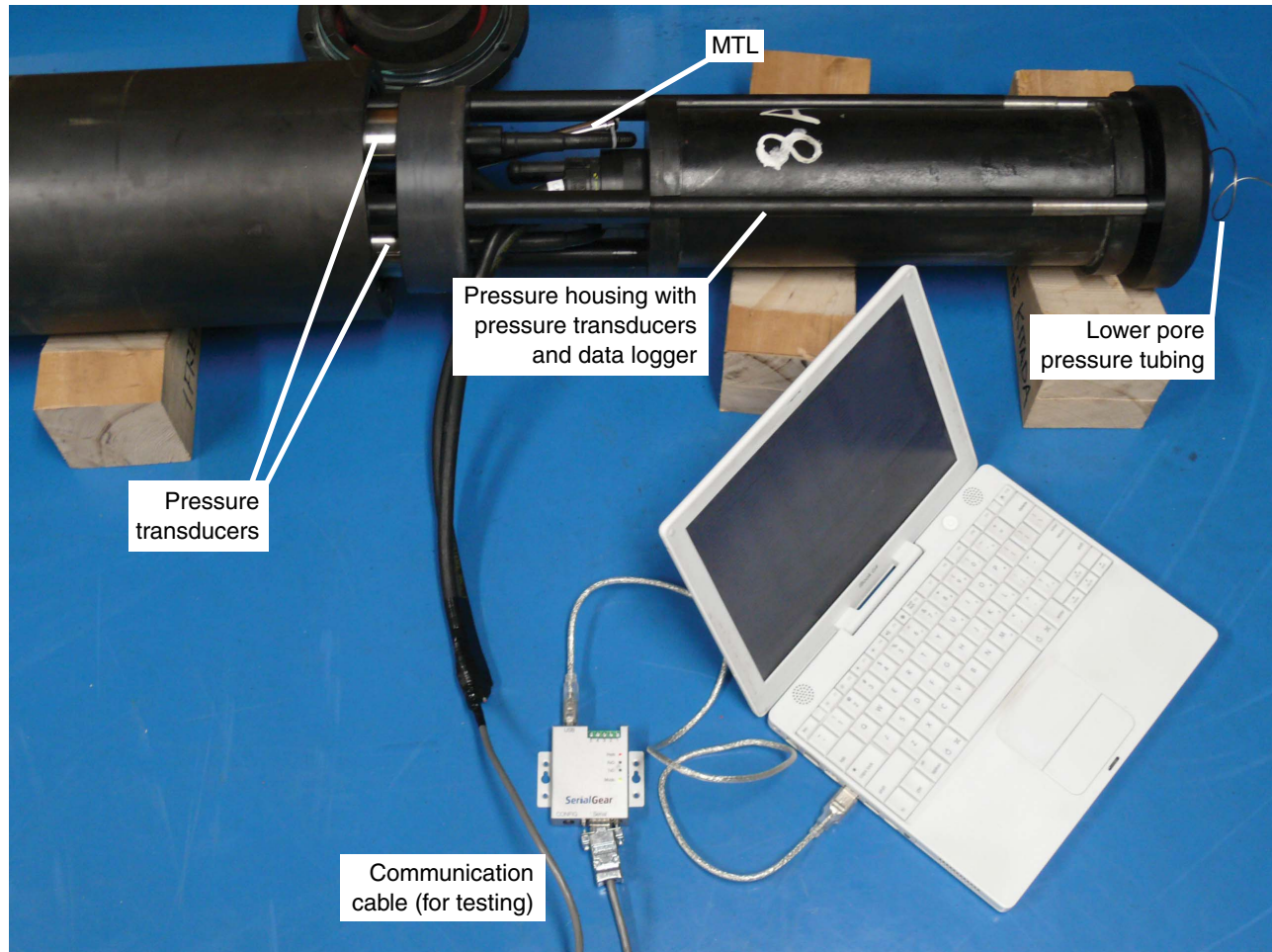


Figure F32. Diagram of smart plug pressure case and instrument package.

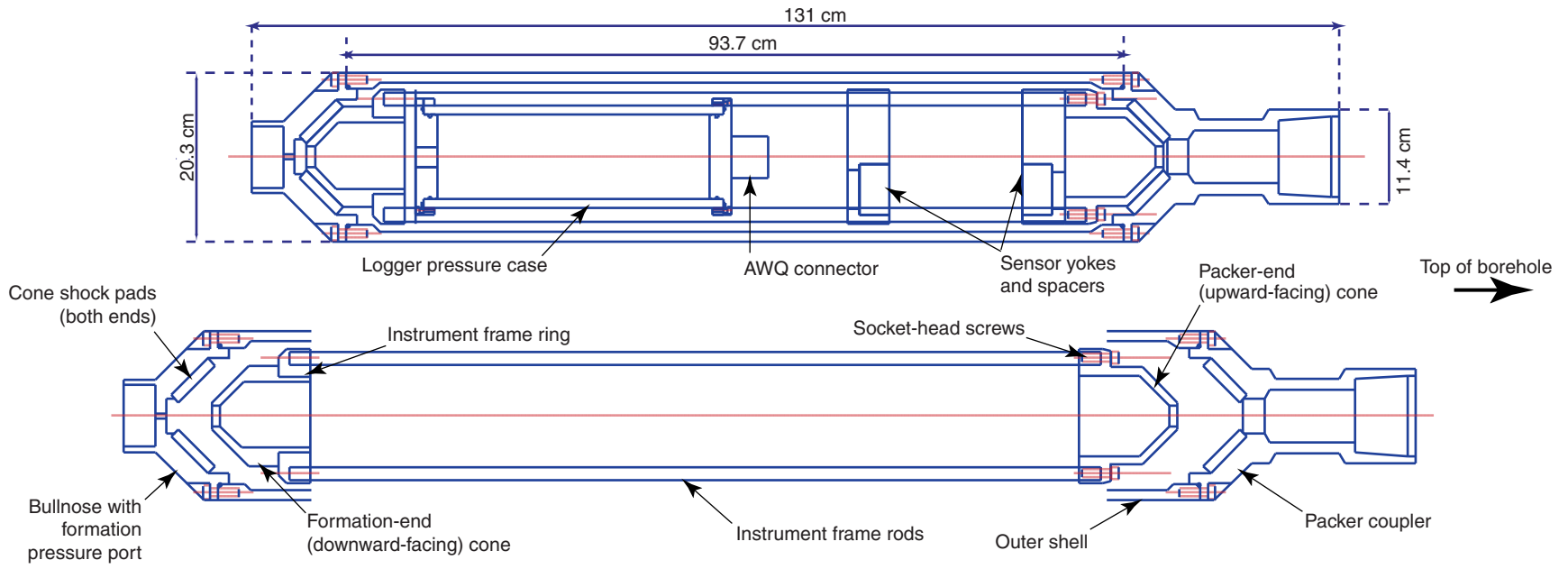


Figure F33. Orientation system used during Expeditions 319 and 322. Coordinates for superconducting rock magnetometer (modified from Richter et al., 2007). SQUID = superconducting quantum interference device.

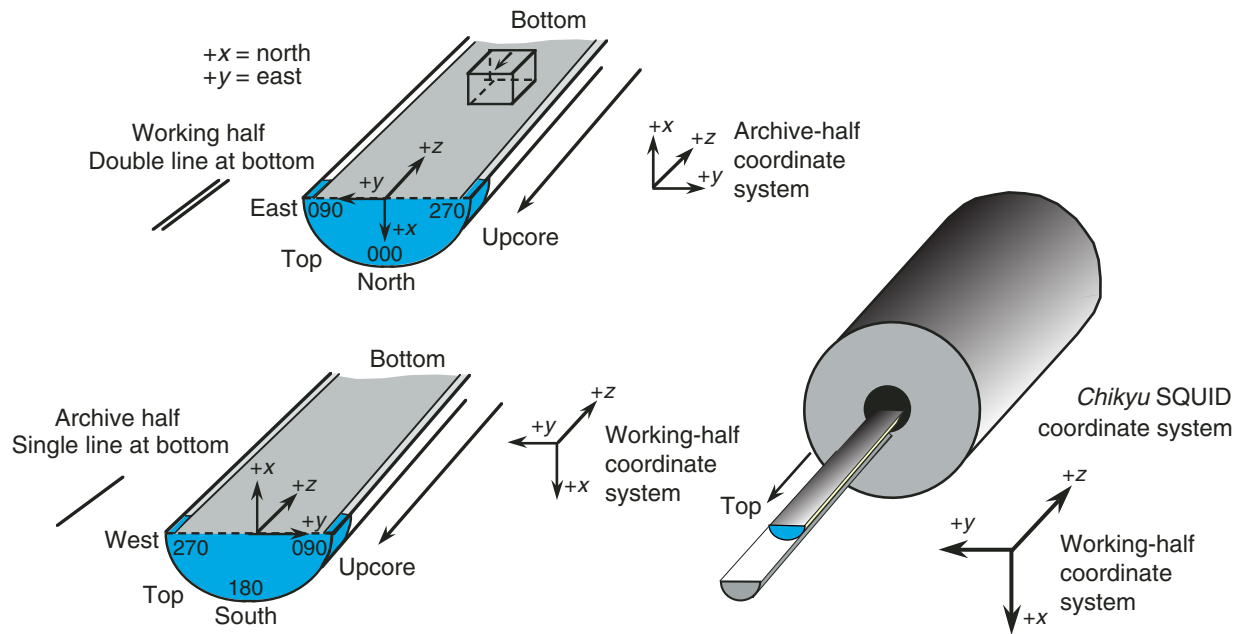


Table T1. Scan settings for X-ray CT scanner. (See table notes.)

| Parameter | Setting |
|------------------------|--------------------|
| Scan type | Helical-full-0.5 s |
| Interval (mm) | 0.625 |
| Gantry tilt | S0.0 |
| SFOV | Small |
| Tube voltage (V) | 120 |
| Tube current (mA) | 100 |
| Detector rows | 16 |
| Helical thickness (mm) | 0.625 |
| Pitch | 0.562:1 |
| Speed (mm/rot) | 5.62 |
| DFOV (cm) | 9.6 |
| R/L center (mm) | R0.0 |
| A/P center (mm) | A0.0 |
| Recon type | Detail |
| Matrix size | 512 × 512 |
| Recon option | Full |
| Direct vis | Off |

Notes: Protocol name: 090624_Exp319 9.1 071210_Aluminum Piece. SFOV = scan field of view, DFOV = dual field of view. R/L center = distance right or left of the center line, A/P center = distance anterior or posterior of the center line.

Table T2. MWD-APWD tool acronyms, descriptions, and units. (See table notes.)

| Tool | Output | Description | Unit |
|---------------------|----------------------|---|-------------------|
| MWD | | Measurement while drilling | |
| | HKLD | Hookload | kgf |
| | SWOB | Surface weight on bit | kgf |
| | DWOB | Downhole weight on bit | kgf |
| | SPPA | Surface pump pressure | kPa |
| | ROP*5 | 5 ft averaged rate of penetration | m/h |
| | GRM1 | LWD natural gamma radiation | gAPI |
| | CRPM_RT | Collar rotation per minute | rpm |
| | TRPM_RT | Fluid pulse turbine rotation per minute | rpm |
| | Stick-slip indicator | rpm | |
| APWD | | Annular pressure while drilling | |
| | PRSA | Annular pressure | kPa |
| | ATMP_CDR | Annular temperature | °C |
| | ECD_CDR | Equivalent circulating density | g/cm ³ |
| | SPPA | Surface pumpout pressure | kPa |
| | SHKRSH | Shock risk | |
| | STICKNSLIP | Slimpulse stick-slip | rpm |
| | CRPM | Slimpulse collar rotation per minute | rpm |
| | STUCK | Percent time stuck | — |
| | MTFS | PowerPulse magnetic toolface | ° |
| | MWD_GR_BHC | Borehole corrected gamma ray | gAPI |
| geoVISION real time | | geoVISION resistivity tool | |
| | GR_RAB_RT | Natural gamma radiation | gAPI |
| | RES_RING_RT | Ring resistivity | Ωm |
| | RES_BIT_RT | Bit resistivity | Ωm |
| | RES_BS_RT | Shallow-button resistivity | Ωm |
| | RES_BM_RT | Medium-button resistivity | Ωm |
| | RES_BD_RT | Deep-button resistivity | Ωm |
| | RB_RT | Relative bearing | ° |
| | HAZI_RT | Hole azimuth | ° |
| | DEVI_RT | Hole deviation | ° |
| | ECAL_RAB_RT | Caliper | inch |
| | SHK_RAB_TRANS_RT | Transverse shock | 1/s |
| | SHK_RAB_AX_RT | Axial shock | 1/s |
| geoVISION memory | | geoVISION resistivity tool | |
| | GR | Total natural gamma radiation | gAPI |
| | RES_RING | Ring resistivity | Ωm |
| | RES_BIT | Bit resistivity | Ωm |
| | RES_BS | Shallow-button resistivity | Ωm |
| | RES_BM | Medium-button resistivity | Ωm |
| | RES_BD | Deep-button resistivity | Ωm |
| | RES_BS_IMG | Shallow-button resistivity image | Ωm |
| | RES_BM_IMG | Medium-button resistivity image | Ωm |
| | RES_BD_IMG | Deep-button resistivity image | Ωm |
| | TAB_RAB_RING | Ring resistivity time after bit | s |
| | TAB_RAB_BS | Shallow-button resistivity time after bit | s |
| | TAB_RAB_BM | Medium-button resistivity time after bit | s |
| | TAB_RAB_BD | Deep-button resistivity time after bit | s |
| | ECAL_RAB | RAB caliper | inch |
| | HAZI | Hole azimuth from well survey | ° |
| | DEVI | Hole deviation from well survey | ° |
| | P1NO | Pad 1 rotation relative to north azimuth | ° |

Notes: LWD = logging while drilling. RAB = resistivity at the bit.



Table T3. Measurement performance specifications of the geoVISION tool. (See table notes.)

| Measurement | Vertical resolution (inches) | Depth of investigation (inches) | Diameter of investigation (inch) | | Horizontal resolution | | Midpoints of extremes |
|-----------------------------|---------------------------------|------------------------------------|-------------------------------------|--------------------|-----------------------------------|------------------------------------|-----------------------|
| | | | $R_t/R_{xo} = 10$ | $R_t/R_{xo} = 0.1$ | $R_t/R_{xo} = (10 \times \pi)/56$ | $R_t/R_{xo} = (0.1 \times \pi)/56$ | |
| Resistivity at the bit | 12–24* | 12 | 32 | 32 | | | |
| Ring resistivity | 2–3 | 7 | 22 | 25 | | | |
| Button resistivity | | | | | | | |
| Shallow-focused resistivity | 2–3 | 1 | 19 | 24 | 1.07 | 1.35 | 1.2 |
| Medium-focused resistivity | 2–3 | 3 | 15 | 21 | 0.84 | 1.18 | 1 |
| Deep-focused resistivity | 2–3 | 5 | 11 | 16 | 0.62 | 0.9 | 0.75 |

Notes: * = depends on bit subs. Vertical penetration rate = 30 m/h (= 1371.6 inches/h = 22.86 inches/min). At typical rotation rate (50 rpm), this penetration rate oversamples vertically. R_t = true resistivity of formation, R_{xo} = resistivity of zone invaded by drilling fluid. When R_t and R_{xo} are approximately equal ($R_t/R_{xo} \sim 1$), drilling fluid invasion may be minimal due to measurement of resistivity soon after hole cutting. R_t below frontal thrust = ~ 0.4 – $0.6 \Omega\text{m}$, R_{xo} of drilling fluid (seawater) = $0.19 \Omega\text{m}$; therefore, R_t/R_{xo} may be >1 , depending on invasion. Horizontal resolution for the geoVISION tool is intermediate between the extremes of R_t/R_{xo} shown in the table. The geoVISION tool records 56 points with each tool revolution. The accuracy of the segment location is $\pm 1^\circ$.

Table T4. Wireline logging tool acronyms, descriptions, and units. (See table note.)

| Tool | Output | Tool name/description | Unit |
|---------------|-----------------------------------|--|--------------------------------|
| TLD | PEFZ | Three-Detector Lithology Density Standard resolution formation photoelectric factor | b/e ⁻ |
| | RHOZ | Standard resolution formation density | g/cm ³ |
| HGNS | TNPH | Highly Integrated Gamma Ray Neutron Sonde Thermal neutron porosity | m ³ /m ³ |
| | NPHI | Thermal neutron porosity (ratio method) | m ³ /m ³ |
| | NPOR | Enhanced thermal neutron porosity | m ³ /m ³ |
| HRLA | RT_HRLT | High-Resolution Laterolog Array HRLT computed true resistivity | Ωm |
| | RXO_HRLT | HRLT computed invaded zone resistivity | Ωm |
| | RLA0, 1, 2, 3, 4, 5, | HRLT borehole corrected resistivity (0, 1, 2, 3, 4, 5) | Ωm |
| | RM_HRLT | HRLT mud resistivity | Ωm |
| | GR | Total natural gamma radiation | gAPI |
| EMS | HD1, 2, 3 | Environmental Measurement Sonde Hole diameter (1, 2, 3) | inch |
| | TMP | Mud temperature | °C |
| | REMS | Mud resistivity | Ωm |
| MCFL | RXOZ | Micro-Cylindrically Focused Log MCFL standard resolution invaded zone resistivity | Ωm |
| | | | |
| FMI | C1, C2 | Formation Microlmager Orthogonal hole diameter | inch |
| | P1AZ | Pad 1 azimuth | ° |
| | FC A(1-4), B(1-4), C(1-4), D(1-4) | FMI buttons, Pads A-D, rows 1-4 | ° |
| GPIT | DEVI | General Purpose Inclinometry tool Hole deviation | ° |
| | HAZI | Hole azimuth | ° |
| | Fx, Fy, Fz | Magnetometer (x-, y-, z-) axis | A/m |
| | Ax, Ay, Az | Acceleration (three orthogonal components) | m/s ² |
| Sonic Scanner | DTCO | Δt compressional | μs/ft |
| | DTSM | Δt shear | μs/ft |
| PPC | HD1, 2_PPC1 | Power Positioning Device and Caliper Tool Hole diameter 1, 2 | inch |
| | | | |
| HNGS | HSGR | Hostile Environment Natural Gamma Ray Sonde HNGS standard gamma ray | gAPI |
| | HCGR | HNGS computed gamma ray (HSGR minus uranium) | gAPI |
| | HFK | Formation potassium concentration | % |
| | HTHO | Formation thorium concentration | % |
| | HURA | Formation uranium concentration | % |

Note: HRLT = High Resolution Laterolog Array Tool.

Table T5. Measurement performance specification of the wireline logging tools. (See table notes.)

| Tool string | Tool | Measurements | Sampling interval (cm) | Vertical resolution (cm) | Depth of investigation (cm) | Logging speed (m/h) |
|------------------------|---------------|---|------------------------|----------------------------------|-----------------------------|---------------------|
| PEX-HRLA-EMS-GR | HGNS | Natural gamma ray | | 31.0 | ~61.00 | 1097 |
| | HGNS | Neutron porosity | | 31.0 | ~23.00 | |
| | HRMS | Bulk density, PEF, caliper | | 45.7 (6 inch hole) | 12.70 | |
| | MCFL | Microresistivity | | 1.8 | 7.62 | |
| | HRLA | Laterolog resistivity | 5.00 | 31.0 | 127.00 | |
| | EMS | Caliper, mud temperature-resistivity | | 15.0 | | |
| | GR | Gamma ray | | 31.0 | 24.00 | |
| FMI-Sonic Scanner-HNGS | FMI | Microresistivity | 0.25 | 0.5 | 2.50 | 305 |
| | GPIT | Acceleration | | 15.2 | | |
| | Sonic Scanner | Compressional and shear slowness, full waveforms | | <1.82 m (15.24 cm sampling rate) | ~7 borehole radii | |
| | HNGS | Spectral gamma ray (corrected gamma ray of uranium; potassium, thorium, and uranium curves) | 15.00 | 20.3–30.5 | 24.00 | |

Notes: PEX = Platform Express, HRLA = High-Resolution Laterolog Array, EMS = Environmental Measurement Sonde, GR = Gamma Ray, HGNS = Highly Integrated Gamma Ray Neutron Sonde, HRMS = High-Resolution Mechanical Sonde, MCFL = Micro-Cylindrically Focused Log. FMI = Formation MicroImager, HNGS = Hostile Environment Natural Gamma Ray Sonde, GPIT = General Purpose Inclinerometry Tool. PEF = photoelectric effect.

Table T6. Characteristic X-ray diffraction peaks for semiquantitative analysis of composite clay minerals, quartz, cristobalite, plagioclase feldspar, and calcite.

| Mineral | Reflection | d-Value (Å) | Peak position ($^{\circ}2\theta$) |
|----------------|------------|-------------|-------------------------------------|
| Composite clay | Multiple | 4.478 | 19.4–20.4 (area) |
| Quartz | 100 | 4.257 | 20.9 (max. intensity) |
| Quartz | 101 | 3.342 | 26.3–27.0 (area) |
| Plagioclase | 2 | 3.192 | 27.4–28.2 (area) |
| Calcite | 104 | 3.035 | 29.1–29.7 (area) |

Table T7. Normalization factors for calculation of relative mineral abundance using bulk powder X-ray diffraction analysis. (See table note.)

| Affected mineral in standard mixture: | Normalization factor | | | |
|---------------------------------------|----------------------|----------------|----------------|----------------|
| | Total clay | Quartz | Plagioclase | Calcite |
| Influencing mineral: | | | | |
| Total clay | 9.8956702E-03 | -1.5889532E-04 | -2.8855808E-04 | -7.3842803E-04 |
| Quartz | -4.7221169E-05 | 5.8782392E-04 | -4.7869325E-05 | -3.1098843E-05 |
| Plagioclase | 7.2794763E-04 | -4.2840613E-05 | 1.3719777E-03 | -3.6005495E-05 |
| Calcite | 4.2042411E-05 | 3.3021188E-06 | -4.1329499E-06 | 1.3071455E-03 |

Note: Singular value decomposition was used to compute factors, following Fisher and Underwood (1995).

Table T8. Analytical conditions for major element analysis of glass beads. (See table notes.)

| Element line | Filter | Crystal | Peak angle (°) | Count time (s) | BG 1 angle (°) | Count time (s) | BG 2 angle (°) | Count time (s) | Detector |
|---------------|--------|---------|----------------|----------------|----------------|----------------|----------------|----------------|----------|
| Na-K α | Out | RX25 | 47,125 | 40 | 49,000 | 10 | 45,250 | 10 | PC |
| Mg-K α | Out | RX25 | 38,804 | 40 | 40,750 | 10 | 36,900 | 10 | PC |
| Al-K α | Out | PET | 144,607 | 40 | 147,150 | 10 | 140,400 | 10 | PC |
| Si-K α | Out | PET | 108,946 | 40 | 106,100 | 10 | 111,250 | 10 | PC |
| P-K α | Out | PET | 89,280 | 40 | 91,350 | 10 | 87,200 | 10 | PC |
| K-K α | A 140 | PET | 50,632 | 40 | 49,200 | 10 | | | PC |
| Ca-K α | Out | PET | 45,154 | 40 | 43,650 | 10 | | | PC |
| Ti-K α | Out | LiF1 | 86,155 | 20 | 85,240 | 10 | 87,120 | 10 | SC |
| Mn-K α | Out | LiF1 | 62,997 | 20 | 62,200 | 10 | 63,820 | 10 | SC |
| Fe-K α | Out | LiF1 | 57,535 | 20 | 58,180 | 10 | 56,900 | 10 | SC |

Notes: Analyses performed on the Supermini (Rigaku) X-ray fluorescence spectrometer. BG = background angle, PC = flow-proportioned counter, SC = scintillation counter.

Table T9. Average measured values and 3σ for the major elements. (See table note.)

| Component | Sample JB-3 | | | | Sample JA-1 | | | |
|--------------------------------|-----------------------------------|--------------------------|----------------------------------|---------------------------------|-----------------------------------|--------------------------|----------------------------------|---------------------------------|
| | Reference value (100% normalized) | Measured value (average) | Standard deviation (3σ) | Relative standard deviation (%) | Reference value (100% normalized) | Measured value (average) | Standard deviation (3σ) | Relative standard deviation (%) |
| Na ₂ O | 2,720 | 2,713 | 0.106 | 1.3 | 3,867 | 3,821 | 0.155 | 1.4 |
| MgO | 5,170 | 5,109 | 0.085 | 0.6 | 1,581 | 1,541 | 0.097 | 2.1 |
| Al ₂ O ₃ | 17,135 | 17,173 | 0.080 | 0.2 | 15,325 | 15,300 | 0.092 | 0.2 |
| SiO ₂ | 50,767 | 50,842 | 0.141 | 0.1 | 64,413 | 64,342 | 0.227 | 0.1 |
| P ₂ O ₅ | 0.293 | 0.286 | 0.014 | 1.6 | 0.166 | 0.144 | 0.012 | 2.7 |
| K ₂ O | 0.777 | 0.764 | 0.020 | 0.9 | 0.775 | 0.783 | 0.034 | 1.5 |
| CaO | 9,753 | 9,789 | 0.049 | 0.2 | 5,739 | 5,691 | 0.031 | 0.2 |
| TiO ₂ | 1,435 | 1,432 | 0.032 | 0.7 | 0.856 | 0.855 | 0.025 | 1.0 |
| MnO | 0.176 | 0.184 | 0.005 | 0.9 | 0.158 | 0.159 | 0.006 | 1.2 |
| Fe ₂ O ₃ | 11,775 | 11,810 | 0.065 | 0.2 | 7,119 | 7,077 | 0.062 | 0.3 |

Note: Values determined on the Supermini (Rigaku) X-ray fluorescence spectrometer from a selection of standard samples.

Table T10. Astronomically calibrated age estimates of calcareous nannofossil datums used as biostratigraphic tie points, Expedition 319. (See table notes.) (Continued on next page.)

| Nannofossil event | Zone (base) | Degree of reliability | Age (Ma) |
|---|-------------|-----------------------|----------------|
| X medium <i>Gephyrocapsa</i> (>3.5 μm)– <i>Emiliana huxleyi</i> | | | 0.082–0.063 |
| FO <i>Emiliana huxleyi</i> | NN21 | B | 0.291 |
| LO <i>Pseudoemiliana lacunosa</i> | NN20 | A | 0.436 |
| LCO <i>Reticulofenestra asanoi</i> | | A | 0.905–0.901* |
| RE medium <i>Gephyrocapsa</i> ($\geq 4 \mu\text{m}$) | | A | 1.04 |
| FCO <i>Reticulofenestra asanoi</i> | | D | 1.136–1.078* |
| LO large <i>Gephyrocapsa</i> (>5.5 μm) | | A | 1.24 |
| LO <i>Helicosphaera sellii</i> | | C | 1.34 |
| FCO large <i>Gephyrocapsa</i> (>5.5 μm) | | | 1.46 |
| FO large <i>Gephyrocapsa</i> (>5.5 μm) | | B | 1.560–1.617* |
| LO <i>Calcidiscus macintyreii</i> ($\geq 11 \mu\text{m}$) | | C | 1.60 |
| FO medium <i>Gephyrocapsa</i> (>3.5 μm) | | A | 1.67 |
| LO <i>Discoaster brouweri</i> | NN19 | A | 2.06 |
| AB <i>Discoaster triradiatus</i> | | A | 2.135–2.216* |
| LO <i>Discoaster pentaradiatus</i> | NN18 | C | 2.393–2.512* |
| LO <i>Discoaster surculus</i> | NN17 | C | 2.52 |
| LO <i>Discoaster tamalis</i> | | C | 2.87 |
| LO <i>Sphenolithus</i> spp. | | C | 3.65 |
| LO <i>Reticulofenestra pseudoumbilicus</i> (>7 μm) | NN16 | A | 3.79 |
| FCO <i>Discoaster asymmetricus</i> | NN15–NN14 | B | 4.13 |
| LO <i>Amaurolithus primus</i> | | | 4.50 |
| LO <i>Ceratolithus acutus</i> | | B | 5.04 |
| FO <i>Ceratolithus rugosus</i> | NN13 | D | 5.12 |
| LO <i>Triquetrorhabdulus rugosus</i> | | | 5.279* |
| FO <i>Ceratolithus acutus</i> | | B | 5.32 |
| LO <i>Discoaster quinquerramus</i> | NN12 | A | 5.59 |
| LO <i>Nicklithus amplificus</i> | | A | 5.978–5.939* |
| FO <i>Nicklithus amplificus</i> | | C | 6.909–6.684* |
| PE <i>Reticulofenestra pseudoumbilicus</i> (>7 μm) | | D | 7.077–7.167* |
| FO <i>Amaurolithus</i> spp./ <i>Amaurolithus primus</i> | NN11b | A | 7.362–7.424* |
| FCO <i>Discoaster surculus</i> | | B | 7.88 |
| LCO <i>Minylitha convallis</i> | | D | 7.78–8.3 |
| FO <i>Discoaster berggrenii</i> | NN11a | D | 8.52 |
| PB <i>Reticulofenestra pseudoumbilicus</i> (>7 μm) | NN10b | A | 8.785–8.761* |
| FO <i>Discoaster pentaradiatus</i> | | | 9.1 |
| FO <i>Minylitha convallis</i> | | D | 9.416 |
| LO <i>Discoaster hamatus</i> | NN10a | C | 9.560 |
| LO <i>Catinaster calyculus</i> | | D | 9.674* |
| LO <i>Catinaster coalitus</i> | | D | 9.687* |
| X <i>Discoaster hamatus</i> – <i>D. neohamatus</i> | | | 9.762* |
| FO <i>Discoaster neohamatus</i> | | C | 9.867–10.521* |
| LCO <i>Discoaster exilis</i> | | | 10.427 |
| FO <i>Discoaster hamatus</i> | NN9 | C | 10.541 |
| LO <i>Coccolithus miopelagicus</i> | | C | 10.613 |
| FO <i>Discoaster calcaris</i> | | | 10.676 |
| FO <i>Discoaster bellus</i> gr. | | C | 10.72 |
| FO <i>Discoaster brouweri</i> | | A | 10.734–10.764* |
| FO <i>Catinaster calyculus</i> | | D | 10.785* |
| FO <i>Catinaster coalitus</i> | NN8 | D | 10.886–10.733* |
| LCO <i>Discoaster kugleri</i> | | A | 11.578–11.596* |
| FCO <i>Discoaster kugleri</i> | NN7 | B | 11.863–11.905* |
| LO <i>Cyclicargolithus floridanus</i> | | D | 12.037 |
| LO <i>Coronocyclus nitescens</i> | | | 12.254 |
| LCO <i>Calcidiscus premacintyreii</i> | | A | 12.447 |
| FCO <i>Triquetrorhabdulus rugosus</i> | | | 12.671 |
| LCO <i>Cyclicargolithus floridanus</i> | | A | 13.294 |
| LO <i>Sphenolithus heteromorphus</i> | NN6 | C | 13.532–13.654* |
| LO <i>Helicosphaera ampliapertura</i> | NN5 | | 14.914* |
| AE <i>Discoaster deflandrei</i> | | | 15.663* |
| FO <i>Discoaster signus</i> | | | 15.702* |
| FCO <i>Sphenolithus heteromorphus</i> | | | 17.721* |
| LCO <i>Sphenolithus belemnus</i> | NN4 | | 17.973* |
| LO <i>Triquetrorhabdulus carinatus</i> | | D | 18.315* |
| FO <i>Sphenolithus belemnus</i> | NN3 | | 18.921* |
| FO <i>Helicosphaera ampliapertura</i> | | | 20.393* |

Table T10 (continued).

| Nannofossil event | Zone (base) | Degree of reliability | Age (Ma) |
|---|-------------|-----------------------|----------|
| <i>X Helicosphaera euphratis</i> – <i>Helicosphaera carteri</i> | | | 20.894* |
| FCO <i>Helicosphaera carteri</i> | | | 21.985* |
| LCO <i>Triquetrorhabdulus carinatus</i> | | | 22.092 |
| FO <i>Sphenolithus disbelemnos</i> | | C | 22.413 |
| FO <i>Discoaster druggii</i> | NN2 | D | 22.824* |
| LO <i>Sphenolithus delphix</i> | | A | 23.089 |
| FO <i>Sphenolithus delphix</i> | | A | 23.356 |
| LO <i>Sphenolithus ciperoensis</i> | NN1 | C | 24.389 |

Notes: Datums are based on Pacific records if not otherwise stated. * = datums based on Atlantic or Mediterranean records. Age estimates adopted from Raffi et al. (2006). X = abundance crossover, FO = first occurrence, LO = last occurrence, LCO = last consistent occurrence, RE = reentrance, FCO = first consistent occurrence, AB = acme beginning, AE = acme end, PE = paracme end, PB = paracme beginning. Degree of reliability: A = distinct, well-defined, and isochronous worldwide; B = indistinct and less well defined but reasonably isochronous; C = distinct and well defined but diachronous; D = indistinct, poorly defined, and diachronous. See Raffi et al. (2006) for detailed explanation.

Table T11. Specification of Versatile Seismic Imager tool.

| Feature | Specification |
|-------------------------------|--|
| Sensor | Geophone accelerometer (GAC-D) |
| Sensitivity (V/g) | 0.5 ± 5% |
| Sensor natural frequency (Hz) | 25 flat bandwidth in acceleration: 2–200 |
| Dynamic range (dB) | >105 at 36 dB gain setting |
| Distortion (dB) | Less than –90 |
| Digitization | 24 bit analog-to-digital converter |

Table T12. Location of survey lines for walkaway vertical seismic profile.

| Line | Starting point | | Ending point | | Length (km) | Shooting interval (m) |
|------------------------|----------------|--------------|--------------|--------------|--|-----------------------------|
| | Latitude | Longitude | Latitude | Longitude | | |
| 1 (A to B) (dip line) | 33°16.188'N | 136°39.966'E | 33°41.190'N | 136°22.707'E | 53.4 (29.3 km to north, 24.1 km to south) | 60 |
| Circle (3.5 km radius) | 33°29.353'N | 136°32.275'E | 33°29.377'N | 136°32.211'E | 21.98 | Every 30 s shot (clockwise) |

Table T13. Location of ocean-bottom seismometers. (See table note.)

| OBS | Latitude | Longitude | Distance from Hole C0009A (m) |
|-----|-------------|--------------|-------------------------------|
| 1 | 33°29.107'N | 136°31.017'E | 3500 |
| 2 | 33°27.704'N | 136°31.987'E | 500 |
| 3 | 33°25.832'N | 136°33.273'E | 3500 |
| 4 | 33°27.236'N | 136°32.309'E | 500 |
| 5 | 33°28.408'N | 136°34.116'E | 3500 |
| 6 | 33°27.604'N | 136°32.430'E | 500 |
| 7 | 33°26.527'N | 136°30.190'E | 3500 |
| 8 | 33°27.336'N | 136°31.869'E | 500 |

Note: OBS = ocean-bottom seismometers.

Table T14. Location of broadband ocean-bottom seismometers.

| ID | Latitude | Longitude | Water depth (m) |
|-----|-------------|--------------|-----------------|
| 5B | 33°07.540'N | 136°50.076'E | 3835.0 |
| 8B | 33°11.977'N | 136°41.090'E | 2648.0 |
| 16B | 33°21.208'N | 136°41.188'E | 2034.0 |

Table T15. Source parameters for walkaway vertical seismic profile.

| Feature | Specification |
|---|---|
| Navigation system | SPECTRA (Concept Inc.) |
| Gun controller | Digishot Ver3.1 (ION Inc.) |
| Air gun | Annular Port Air Gun (BOLT Technology) |
| Gun configuration | 1950 in ³ × 4 strings (Fig. F21) |
| Total volume (in ³) | 7800 |
| Gun pressure (psi) | 2000 |
| Gun depth (m) | 8 |
| <i>Kairei</i> ship speed (kt) | 4 (against ground) recommended; <5 against ground or water required |
| Shooting interval for Line 1 (m) | 60 |
| Shooting interval for circle shooting (s) | 30 |

Table T16. Navigation and positioning parameters for walkaway vertical seismic profile. (See table note.)

| Feature | Specification |
|--------------------|---------------|
| Survey datum | WGS84 |
| Ellipsoid | WGS84 |
| Semimajor axis | 6 378 137 m |
| 1/flattening | 298.257223563 |
| Map projection | UTM |
| Zone number | 53 |
| False easting (m) | 500000 |
| False northing (m) | 0 |
| Scale factor | 0.9996 |

Note: UTM = Universal Transverse Mercator.

Table T17. Specifications of time synchronization and accurate true time recording system.

| Feature | Specification |
|------------------------------|---|
| Radio | GM3688 (Motorola) |
| Model | JJM50KNF9AA2A |
| Frequency band (MHz) | VHF 151.89 |
| Output (W) | 20 |
| Antenna model | WH-150-3M1 |
| Blaster controller | The Shooting System (Macha International, Inc.) |
| Blaster output voltage (V) | 400 regulated |
| Firing accuracy (ms) | 0.25 |
| Firing capacity (Ω) | 40 maximum resistance |
| True time recorder | Symmetricom Truetime XL-GPS (2 on <i>Chikyu</i> , 2 on <i>Kairei</i>), <i>Kairei</i> shooting system has another time recorder |
| Accuracy (ns) | 30 |

Table T18. Recorder parameters. (See table notes.)

| Feature | Specification |
|-----------------------------------|---|
| Data acquisition system | MAXIS (Schlumberger) |
| Sensor | VSI (Schlumberger) |
| Number of receivers (VSI shuttle) | 16 |
| Shuttle interval (m) | 15.12 |
| Sampling rate (ms) | 2 |
| Record length (s) | 40 for Line 1 and circle shooting; 10 for zero-offset VSP |

Notes: MAXIS = Multitask Acquisition Imaging System. VSI = Versatile Seismic Imager. VSP = vertical seismic profile.

Table T19. Zero-offset VSP acquisition parameters.

| Parameter | Value |
|-------------------------------|--------|
| Surface recording length (s) | 10 |
| Surface sampling rate (ms) | 1.0 |
| Downhole recording length (s) | 20 |
| Downhole sampling rate (ms) | 2.0 |
| Top of survey DRF (m) | 1998.8 |
| Bottom of survey DRF (m) | 3217.8 |

Table T20. Sensor specifications for dummy run test.

| | |
|--|--|
| Self-recording accelerometer-tiltmeter | |
| Accelerometer | Kyowa EI AS-100TA Max. $\pm 100 \text{ G}$ $0.084 \text{ m/s}^2/\text{digit}$ |
| Tiltmeter | Applied Geomechanics model 900 $\pm 25^\circ$ $0.002376^\circ/\text{digit}$ |
| Sampling | 16 bit at selectable from 100, 200, 500 Hz |
| Recording | 2 GB CF memory card 2 byte sample |
| Batteries | Four Electrochem BCX85 3B76 lithium batteries (3.6 V, 30 AH each) |
| Power | 210 mA at 8 V supply when recording, 80 mA when standby |
| Housing | SUS316 stainless steel |
| Dimensions | 600 mm length, 135 mm diameter |
| Weight | 46 kg in air, 31 kg in water |
| Borehole strainmeter | |
| Strain | Three sets of transducers to measure strain in 0° , 120° , 240° ; 2 V/mm sensitivity; one volumetric strain measurement |
| Temperature | Inside strain sensor and telemetry sections |
| Sampling | Simultaneously 32 bit 6 channels at 250 Hz; volumetric strain ~40 samples/s |
| Recording | 8 GB SD memory card ~2 byte sample with data compression |
| Power | 118 mA at 24 V supply on recording |
| Batteries | Lithium batteries $3.6 \text{ V} \times 12$ to maintain observation for 2 weeks |
| Dimensions | Cylindrical maximum outer diameter 194 mm, length 4000 mm |
| Weight | 376 kg |
| Interface | Top: flange; bottom: 3-1/2 inch EUE pin; connector (Seacon MINK-10-FCR) on top of telemetry section |
| Borehole seismometers | |
| CMG1T | |
| Recording | None |
| Housing | Titanium cylinder, Seacon MINK-10-FCR on top |
| Dimensions | 127 mm diameter, 1300 mm height |
| Weight | ~50 kg |
| CMG3T | |
| Recording | None |
| Housing | Titanium cylinder, Seacon MINK-10-FCR on top |
| Dimensions | 126 mm diameter, 1503 mm height |
| Weight | ~50 kg |
| Instrument carrier | |
| Purpose | To hold accelerometer and seismometers, suspend strainmeter and tubings, and serving fluid/cement path down |
| Dimensions | 8439.2 mm length, effective diameter 8 inches |
| Weight | 486 kg |

Table T21. Miniature temperature logger 1854 settings.

| Serial number | Sampling interval (s) | Distance from top of instrument carrier (cm) | Start | | End | |
|---------------|-----------------------|--|-------------|----------|-------------|----------|
| | | | Date (2009) | Time (h) | Date (2009) | Time (h) |
| 276 | 4 | 99 | 18 Aug | 0700 | 21 Aug | 0713 |
| 254 | 1 | 99 | 19 Aug | 0300 | 19 Aug | 2103 |
| 264 | 4 | 333 | 18 Aug | 0700 | 21 Aug | 0713 |
| 314 | 1 | 333 | 19 Aug | 0300 | 19 Aug | 2103 |
| 315 | 4 | 574 | 18 Aug | 0700 | 21 Aug | 0713 |
| 291 | 1 | 574 | 19 Aug | 0300 | 19 Aug | 2103 |
| 316 | 4 | 750 | 18 Aug | 0700 | 21 Aug | 0713 |
| 252 | 1 | 750 | 19 Aug | 0300 | 19 Aug | 2103 |
| 279 | 4 | Bottom of sensor tree | 18 Aug | 0700 | 21 Aug | 0713 |